Construction and Performance of an Inverted Pendulum Thrust Balance

by

Brett R. Tartler

B.S. Aerospace Engineering
University of Florida, 2008
B.S. Mechanical Engineering
University of Florida, 2008

Submitted to the Department of Aeronautics and Astronautics
in Partial Fulfillment of the Requirements for the Degree of

Master of Science in Aeronautics and Astronautics

at the

MASSACHUSETTS INSTITUTE OF TECHNOLOGY

June 2010

Signature of Author:..
Department of Aeronautics and Astronautics
May 21, 2010

Certified by:...
Manuel Martinez-Sanchez
Professor of Aeronautics and Astronautics
Thesis Supervisor

Accepted by:...
Eytan H. Modiano
Associate Professor of Aeronautics and Astronautics
Chair, Committee on Graduate Students

Construction and Performance of an Inverted Pendulum Thrust Balance

by

Brett R. Tartler

Abstract

The objective of the work in this thesis was to devise a means of profiling the thrust of the MIT Space Propulsion Lab's (SPL) Diverging Cusped Field (DCF) thruster and, more generally, other thrusters of similar size and thrust levels. The former SPL thrust stand, which had been used to characterize the BHT-200 engine, was not suitable for the DCF because of its torsional style design. An entirely new, inverted pendulum-type balance needed to be built. The new design employs a vertical arm with the DCF situated at the top and a counterweight placed at the bottom. The vertical arm rotates at the fulcrum through a flexible pivot attached to a base. A horizontal thrust force from the DCF causes the balance to rotate. This motion is sensed by a linear variable differential transformer (LVDT) and counteracted by a force from a voice coil. The voice coil's neutralizing force nulls the balance back to an equilibrium position and supplies the thrust value produced by the DCF.

The inverted pendulum thrust balance was built from an initial design proposed by Professor Manuel Martinez-Sanchez. Many of the electrical components found on the old thrust stand, like the LVDT and the voice coil, were incorporated into the new one. Additionally, the control software and hardware from the old stand required several changes and updates to be compatible with the new design. After the assembly of the new thrust balance, the issues of calibration and thermal drift during use were also addressed. Once a means of correcting the undesired operational forces and thermal effects had been established, the balance displayed thrust measurement within a range of 0mN to 23mN with an uncertainties as low as ±0.5mN.

Thesis Supervisor: Manuel Martinez-Sanchez
Title: Professor of Aeronautics and Astronautics

Acknowledgments

There are many people who deserve credit for helping me through the journey of completing a research project and writing a thesis about the work. First and foremost, I would like to express my gratitude to my advisor, Professor Manuel Martinez-Sanchez, and Assistant Professor Paulo Lozano, for their assistance in navigating me through this project. I would also like to give a very special thanks to MIT research associate Randy Leiter. Not only did Randy permit me to use and alter his control box and Labview PID software, but he spent many hours of his own time with me, explaining the various concepts of the thrust balance's control system. He acted almost as an unofficial thesis advisor, for which I am very grateful. Additionally, I would also like to acknowledge Ryan Daspit's great efforts in making the CAD model of the thrust balance. Ryan worked diligently in the Aero-Astro Machine Shop to create the legs and arms of the balance and its calibration system. Thanks as well to Daniel Courtney, Taylor Matlock, and Steve Gildea for their assistance while I worked in the Space Propulsion Lab.

Outside of MIT, I would also like to acknowledge my parents and Kate Herzhauser for all of their hard work proofreading chapter after chapter of my writing. I also need to thank my brother, Josh Tartler, for his moral support.

This thesis is dedicated to my parents, whose love and guidance has always been a constant throughout my academic career. Without them I surely would not be where I am today.

Contents

List of Figures

9

List of Tables

1. Introduction

The purpose of the work carried out in this thesis was to devise a way of quantifying the performance of the Diverging Cusped Field (DCF) thruster, and other similar thrusters, in terms of the useful force they can produce to move a spacecraft in a vacuum environment. The traditional way of making such a measurement is to use a device known as a thrust balance. Therefore, an inverted-pendulum thrust balance was designed, built, calibrated, and tested to determine the thrust of the DCF.

1.1 Motivation for the Creation and Use of a Thrust Balance

There are two traditional means of moving a man-made object through space, chemical propulsion and electric propulsion. Chemical propulsion relies on the acceleration of a gas through a nozzle to produce thrust. The gas is typically heated through the use of a chemical reaction, or a catalyst, and that thermal energy is converted to kinetic energy, or velocity, as it travels through the nozzle. In contrast, electric propulsion accelerates a gas through the use of electric heating or electric and magnetic forces. The DCF engine falls under the category of electric propulsion [5].

In general, electric propulsion devices provide very small amounts of thrust compared to chemical propulsion, however, the specific impulse for most forms of electric propulsion can be many tens of times greater than that of a chemical rocket [16]. Specific impulse (Isp) is a ratio of the thrust to the rate of fuel being used [11]. Such a form of propulsion, with a high Isp and low thrust, is often ideal for deep space missions, such as sending probes to the outer planets of the solar system. It is also advantageous for nanosatellites, which require a very tiny and precise amount of thrust to perform operations such as pointing and station keeping [17].

The DCF is a relatively new form of electric propulsion. An early version of this thruster was constructed and tested by graduate student Daniel Courtney at MIT in 2008. A preliminary measurement of the engine's thrust as a function of the anode current was done by the Busek Company[5]. While these data gave a good indication of the approximate thrust the DCF can produce, it did not take into account the

effects of altering the anode and cathode positions [5]. Since this time, several modified versions of the DCF have also been created. To fully understand the capabilities of this new electric propulsion system, it is necessary to determine the effects that these modifications have on thrust. It would also be quite beneficial to make these thrust measurements where the work is being conducted at the Space Propulsion Laboratory (SPL) at MIT, rather than ship the thruster to the Busek Company to test each and every small modification or change. Since the DCF produces a small amount of thrust, on the order of a millinewton, the SPL was in need of a device capable of measuring small forces. Thus, a new thrust balance was needed. The SPL expects to use this new balance not only to profile the thrust regime of the DCF, but to enable or enhance research on a variety of thrust concepts in the future, including Hall thrusters, Helicon thrusters, and other forms of electric propulsion.

1.2 Reasons for the SPL Thrust Balance Redesign

The lab already had a working thrust balance developed in 2003 by MIT graduate student Jareb Mirczak. The balance was torsional type in nature, where the engine rests on one end of a lever arm that is free to rotate about a pivot point, with a counterweight placed on the other end [14]. In an initial attempt to use this balance with the DCF, it was discovered that under the weight of the DCF the lever arm was not able to reach an equilibrium position. Rather, the balance would tilt all the way in the direction of DCF or all the way in the direction of the counterweight, unable to find a neutral balance. This was occurring because the weight of the DCF was just too much for the flexible torsional pivot at the fulcrum to handle. The types of forces being created on the frictionless flexible pivot were larger than what it was designed to withstand and the pivot was therefore unable to function as intended.

Other flaws in the design of the old thrust balance existed as well. The old balance had a rather small moment arm in relation to the physical size of the DCF. This could introduce uncertainties as to where exactly the thrust was being applied. In the old design the engine also rotated about a central pivot, meaning that the balance measured a torque. The force value therefore depended on an uncertain moment arm

caused by the ambiguous position of the resultant thrust force from the engine. Since the design proved to be flawed for heavier propulsion systems and the uncertainty was likely to be high for engines like the DCF, a redesign was deemed necessary.

2. Electric Propulsion and Thrust Measurement

Before exploring the work done to create the DCF's thrust balance, it would be beneficial to provide more background information about the history of electric propulsion, the categories of electric propulsion, and the means traditionally used to measure thrust for these types of devices.

2.1. A Brief History of Electric Propulsion

While electric propulsion wasn't widely used on spacecraft until the end of the twentieth century, its principles had been proposed as early as 1906 by an American scientist named Robert Goddard and in 1911 by a Russian rocket scientist named Konstantin Tsiolkovsky, both of whom were likely inspired by devices known as cathode rays [4]. By 1913, Goddard filed a patent for a device that magnetically trapped electrons to produce ionizing collisions with neutral particles [4]. Four years later, Goddard even had a design for the first electrostatic ion accelerator for the purposes of propulsion [4]. Professor Herman Oberth further supported the electric propulsion idea. In his well respected 1929 book about spaceflight, Oberth lauded the technology's mass-savings potential [7]. By 1933, the first electrothermal engine was developed and built by Valentin Glushko, although it only saw laboratory use [4]. Despite these early developments, chemical thruster research continued to dominate through the late 1940s. This was due to the military demands of World War II, the complexities of testing in vacuum conditions, which is a requirement for electric thrusters, and the obvious need for better chemical rockets to propel a spacecraft into orbit before electric engines could be utilized [4].

In the post war era, Ernst Stuhlinger was the first to pick up the idea of electric thrusters. He published the most extensive paper to date which examined the problem of a power supply to run the engine, gave design guidelines, and even demonstrated how the electric thruster could be optimized to various mission requirements [4]. This marked a turning point for this technology, where it went from a widely idealized and speculative idea to a serious field of research and development. In the late 1950s,

experiments began with electrostatic ion thrusters and thermal arcjets in several government laboratories and private corporations [11]. By the 1960s, the electric propulsion field was flourishing, with ground-based experiments on many different models taking place in large vacuum tanks [11]. The first successful US space test finally occurred on July 20, 1964 with an electrostatic ion engine [11]. This test was part of the Space Electric Rocket Test (SERT) 1 program, which was developed to demonstrate that the concept could work in space as well as it had in vacuum chamber tests [11]. By 1970, NASA flew SERT II and proved the long term abilities of this technology. This mission lasted until 1991, with over two hundred engine restarts conducted between 1973 and 1981, and a prolonged firing which lasted five months continuously [6].

From 1970 through 1990, the research in the field of electric propulsion focused primarily on mercury and xenon fed ion thrusters, hydrazine resistojets and arcjets, magnetoplasmadynamic (MPD) thrusters, and Teflon-propellant pulsed plasma thrusters (PPTs) [6]. After the collapse of the Soviet Union, research on Hall Effect thrusters started in the US. Previously, the Hall thruster had been more extensively studied in the USSR, but after 1991 this changed with technology flowing into the United States from the former communist country. In 1998 NASA launched Deep Space 1 (DS1), the first mission to employ an ion engine to travel beyond Earth orbit. DS1 successfully flew past the asteroid Braille and Comet Borrelly [6]. By now, dozens of commercial satellites feature electric propulsion thrusters, and most scientific missions use them as well.

2.2 The Types of Electric Propulsion

Electric propulsion thrusters generally fall into three main categories: electrothermal, electromagnetic, and electrostatic propulsion. Electrothermal engines create thrust by electrically heating the gaseous propellant [11]. This type of electric propulsion is very similar to the more traditional chemical engine since it still utilizes a nozzle to convert thermal energy to kinetic energy. The biggest difference being that the propellant is electrically heated, either in addition to or instead of, being heated by

a chemical reaction. Examples of thrusters from this category include resistojets and arcjets. The resistojet heats the propellant by simply passing it over an electrically heated surface, while the arcjet passes an electric current through the propellant to raise the temperature of the gas to a much higher degree than the chamber walls. Resistojet specific impulses generally reach as high as 350 seconds (maximum of 800 seconds with a fuel of H_2), while arcjet specific impulses can be as high as 600 seconds (1500 seconds with H_2 fuel) [11]. Both of these offer significant Isp improvements over the traditional chemical rocket, which reaches specific impulses of no greater than 500 seconds.

Electromagnetic thrusters, in contrast, use interactions of magnetic fields with electric currents to drive a group of charged particles [11]. This group of engines requires no nozzle; it accelerates its ionized propellant using electromagnetic forces. An example of this type of propulsion system is the Magnetoplsamadynamic (MPD) thruster. The principle which makes this device work is the Lorentz Force, described by the equation below.

$$\overrightarrow{F} = \sigma \left(\overrightarrow{E} + \overrightarrow{u} \times \overrightarrow{B} \right) \tag{2.1}$$

In this equation, σ is the electric charge of a particle, $\overrightarrow{E}$ is the electric field present, $\overrightarrow{u}$ is the velocity of a charged particle, and $\overrightarrow{B}$ is the magnetic field present. When an electric field is perpendicular to a magnetic field, and some ionized gas has a velocity perpendicular to both the electric and magnetic fields, it creates a force of $\overrightarrow{F} = \overrightarrow{j} \times \overrightarrow{B}$, which is the thrust of the engine [11]. While this form of electric propulsion is attractive because of its high Isp and relatively high thrust levels, which can be on the order of a Newton or more, it has significantly lower efficiency levels than other thrusters and, as a result, a rather large amount of energy (heat) to dissipate. The amount of waste energy that needs to be dissipated is often so high that MPDs must be operated in a pulse mode rather than used for continuous firing to prevent the engine from overheating.

Electrostatic thrusters generally employ electric body forces to accelerate charged particles [11]. Examples include ion engines, Hall Effect thrusters, and Diverging Cusped Field thrusters. The difference between these technologies is the method in which they trap the electrons used to ionize the propellant. Each design has its advantages and flaws. In ion engines, ionization of the neutral gaseous propellant is typically done through electron bombardment in a chamber whose only open end has a pair of electrically charged gridded plates [12]. Initially, the gas in the chamber is not ionized, and a cathode introduces electrons which collide with the neutral gas. Even still, the gas is weakly ionized, but the gridded plates at the opening favor the acceleration of positively charged ions out of the chamber [12]. This increases the number of electrons, which are repelled by the grids and kept inside the ionization chamber. To prevent the engine from becoming too negatively charged, an anode in the chamber collects some of the electrons and sends them to an external cathode, which adds them in with the positively charged exit plume.

The performance of ion engines is impacted by many factors. The gap between the two grids at the exit of the chamber should be as small as possible, but if made too small, arcs can jump between and cause failure [9]. Losses occur when the grids themselves, or the cathode, absorb some of the ions, or when the higher energy electrons reach the anode without colliding with neutrals [12].

In contrast to the ion engine, Hall Effect thrusters use a magnetic field to trap their electrons instead of an electrically charged gridded opening. The Hall thruster uses a radial magnetic field which, when combined with the axial electric field, produces a secondary motion in the ions and electrons called $\vec{E} \times \vec{B}$ drift [13]. This drift is azimuthal, meaning the particles will follow circular paths inside the engine. The effect is also much more predominant on the electrons which have a very small guiding center about which they drift. While the ions are also effected by the $\vec{E} \times \vec{B}$ drift, they tend to have much bigger guiding centers (typically larger than the Hall thruster itself), and therefore, are free to move axially in the electric field created by the anode. The Hall thruster has relatively high efficiencies, and when this is combined with its more simplistic design than the traditional ion engine, it is often more appealing due

to the variety of missions it can accommodate. For example, without the gridded exit planes often found in ion engines, Hall thrusters have fewer limitations on increasing the thrust [13].

Similar to the Hall thruster, the Diverging Cusped Field thruster uses a magnetic field to trap the electrons used in ionization. A schematic created by MIT graduate student Daniel Courtney is provided in figure 2.1. In essence, electrons are emitted from the cathode, some of which are pulled into the engine by the anode [5]. These electrons become confined by the magnets found on the walls of the DCF [5]. The reason for the confinement is the magnetic mirror created by the magnets in addition to the drift seen in traditional Hall thrusters. In a magnetic mirror, the field strength increases significantly at the ends of the magnetic field lines, and weakens in the middle. This has the effect of trapping particles traveling along the lines, which move quickly through the weak part of the field, but slow down and reverse direction as they are repelled in the stronger magnetic region. The mirror closest to the anode is also the strongest, with one end of the field lines concentrating at the anode itself [5]. The dense field lines at the anode help to prevent the electrons from flowing straight in from the cathode, evading the magnetic cusps. As electrons are caught within the opening of the engine, injecting a neutral gas (typically one with a low ionization energy) into the region creates collisions between the neutral particles and the electrons, thus forming positive ions. These ions are pushed axially out of the thruster by the electric field created by the anode. Some of the electrons from the external cathode also get pulled along with the exiting positive ions, keeping the DCF itself neutralized.

The DCF holds several advantages over the traditional Hall thruster. Since it is much more difficult for the electrons to move across magnetic field lines than it is for them to move along them, fewer are able to jump to the walls of the engine's chamber [5]. Obviously, fewer electrons escaping to the chamber walls keeps the walls from building up a negative potential and attracting ions, which would decrease efficiency. In addition, erosion of the chamber should also decrease [5]. Furthermore, the DCF's divergent shape helps to reduce the magnetization of ions as they exit the chamber,
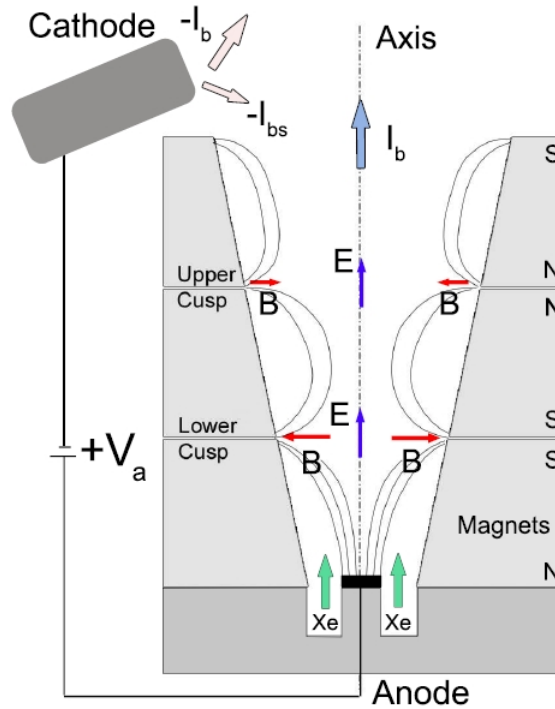
Figure 2.1: Schematic of the Diverging Cusped Field Thruster[5].

primarily because the magnetic fields they are exposed to become weaker and weaker
[5].

2.3 The Evolution of Thrust Measurement

The history of thrust measurement begins with chemical rockets, as they had been
developed many years prior to the first electric propulsion engine. Chemical rockets,
as well as jet engines and other devices which produce large amounts of thrust, are
measured with load cells [16]. Load cells can trace their origins to Lord Kelvin, who
discovered the correlation between a metal's resistance and the tension or compression
the metal was experiencing [7]. A load cell measures force through the use of sensitive
strain gages which measure the deformation of a material of known elasticity [7]. An
example of a typical load cell test setup is shown in figure 2.2.

Measurement of the force produced by electric thrusters is considerably different.
The force from an electric engine is typically not strong enough to deform any basic
solid materials, making the use of strain gages and load cells impractical. Instead,
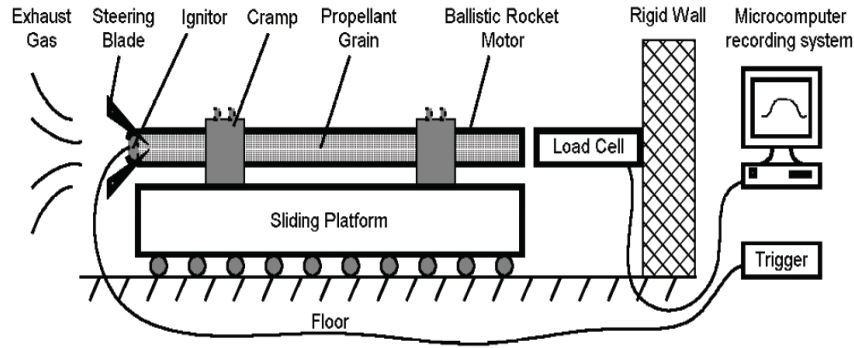
Figure 2.2: An example of the application of a load cell[7].

thrust is measured with micro-scale sensitive devices, typically called thrust balances or thrust stands. While similar in design to very accurate weight scales, they have their own set of complications to overcome. This includes the vacuum environment in which they operate, as well as, strong thermal gradients from the thruster and measurement interference from engine attachments like the gas feed line. For obvious reasons, thrust stands began to appear around the same time testing began on electric propulsion engines. Early prototypes were built at NASA, such as the Micropound Extended Range Thrust Stand (MERTS) at the Goddard Spaceflight Center and Thomas Haag's pulsed plasma thrust stand at the Lewis Research Center [14]. Since then, micro and millinewton thrust balances have been built at various universities and private companies to test a wide variety of space propulsion applications.

Many unique designs exist for the thrust stand. Most can be generally classified into one of two categories: the pendulum style and the torsional style [16]. The pendulum type thrust stands are typically either considered hanging or inverted. The hanging pendulum balance is shown in figure 2.3. The thruster sits on a platform that hangs from an arm attached to a base by a pivot point of known stiffness. This design is inherently stable because any oscillations it experiences are damped out by gravity. Using a torque balance, one can obtain the basic equation for the displacement from a known thrust with relative ease:

23
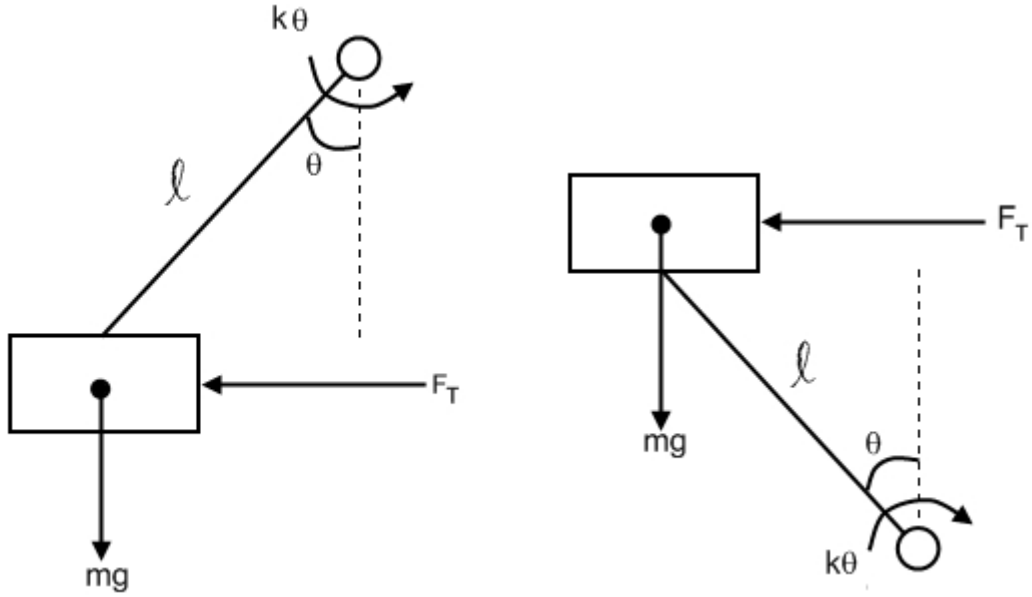
Figure 2.3: The hanging pendulum style (left) and inverted-pendulum style (right) thrust balances.

$$\Sigma\tau = 0 = F_T\ell - mg\ell\sin\theta - k\theta \tag{2.2}$$

(using small angle approximation, $\sin\theta \approx \theta$)

$$F_T\ell = mg\ell\theta + k\theta \tag{2.3}$$

(if $\theta \approx \frac{x}{\ell}$)

$$x = \frac{F_T\ell^2}{mg\ell + k} \tag{2.4}$$

The inverted pendulum is similar, only now gravity works against the torque from the pivot rather than with it. The inverted pendulum can be found in figure 2.3, and the equations involved are the same as before, but now with gravity working in the
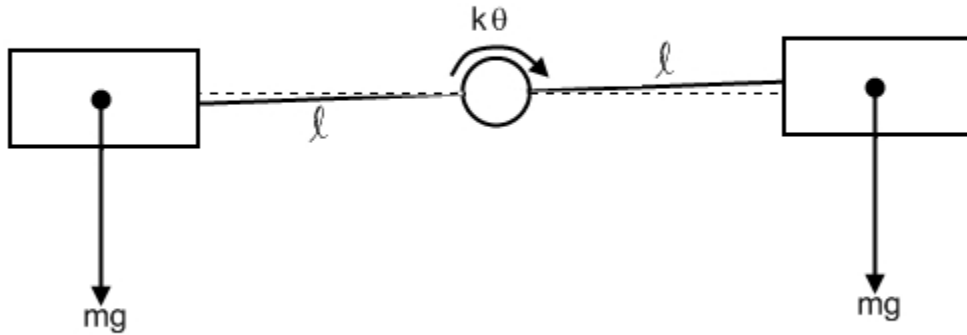
Figure 2.4: The torsional style thrust balance.

opposite direction.

$$\Sigma\tau = 0 = F_T\ell + mg\ell\sin\theta - k\theta \tag{2.5}$$

$$x = \frac{F_T\ell^2}{k - mg\ell} \tag{2.6}$$

Both designs have their advantages and disadvantages. While the sensitivity of the hanging pendulum is hindered by the length of the arm, the inverted pendulum can be made more sensitive by matching the pivot stiffness with the gravity term [16]. On the other hand, the inverted pendulum is unstable and needs some form of active control, a feature that is unnecessary in the hanging design.

The other general type of thrust balance, the torsional style, uses a counterweight rather than the weight of gravity to keep the stand in a neutral position [14]. A sketch of a typical torsional style balance is shown in figure 2.4.

$$\Sigma \tau = 0 = (F_T + mg\sin\theta)\,\ell - mg\ell\sin\theta - k\theta \qquad (2.7)$$

$$\theta = \frac{F_T\ell}{k} \qquad (2.8)$$

$$x = \frac{F_T\ell^2}{k} \qquad (2.9)$$

Looking at the torque balance confirms that the sensitivity is dependent upon the stiffness of the pivot and the arm length only.

3. Design of the SPL Thrust Balance

This section will illustrate the entire design method for the SPL thrust balance. It will start with the initial requirements of the project and then go on to show the design selection process. A brief examination of the design's system dynamics, both with and without an active control system, will be given. After that, the first steps of construction will be discussed, including the process of selecting components like the flexible pivots, LVDT, and voice coil. The CAD model and machine shop work completed by MIT graduate student Ryan Daspit will also be mentioned briefly. Finally, the control system hardware and software will be illustrated in great detail, and the calibration methods and thermal testing that were performed will also be explained.

3.1 Design Requirements

The requirements driving the design of the SPL thrust balance were based on five principles. First, the design had to be feasible for operation inside of the Space Propulsion Lab's vacuum chamber, known as ASTROVAC. This means that the balance must physically fit within the dimensions of ASTROVAC. In addition, the thruster's position as it sits on the stand should place it as close to the middle of the chamber as possible. Keeping the thruster away from the edges of the chamber prevents the walls from interfering with the exhaust plume of the engine. In order to operate within the vacuum chamber, the thrust balance also must also be created out of vacuum safe components. No material on the thrust stand should exhibit a high degree of outgassing in a vacuum environment in order for ASTROVAC to remain clean and maintain very low levels of pressure.

The second core requirement for the SPL thrust balance was high measurement sensitivity. From the initial testing done at Busek, it is known that the DCF produces thrust levels between 6 and 16mN[5]. Therefore, the balance must be able to measure forces on the order of a millinewton to produce accurate results with an error of less than 10%. That means a resolution of at least 0.1mN is desirable. It

was noted in the previous section that the sensitivity of the old thrust balance was compromised by its use of a small lever arm. The larger the lever arm, the more accurate the thrust balance becomes, as dictated by the equations from that section. To maximize sensitivity, the lever arm should be as long as possible without making use in ASTROVAC difficult. It was also mentioned that torsional balances tend to be capable of the highest amount of accuracy, followed by the inverted-pendulum and hanging pendulum styles.

In addition to operating under vacuum and measuring force with a high degree of accuracy, the design had to be insensitive to vibrations. A vibration could cause the stand to shake and register a false thrust reading. To reduce the effect of vibrations, the design must be statically balanced. If not statically balanced, a displacement could rock the base:

$$x_b = \bar{x}_b \sin\left(\omega t\right) \tag{3.1}$$

Such a base excitation as shown above would cause a misleading thrust reading:

$$F_x = -m_{thruster}\bar{x}_b\omega^2 \sin\left(\omega t\right) \tag{3.2}$$

The SPL thrust balance also needed to be insensitive to shifts in the thrust line of action. If the balance measures thrust based on the torque produced by the thruster's force on a moment arm, then any small shift in the line of action of that thrust force would create measurement uncertainty. To eliminate the effect of shifts in the thrust line of action, the design must not measure torque but rather determine the thrust force using an arrangement that produces pure linear displacement.

Finally, the balance had to be capable of supporting the weight of the DCF. It was speculated that the pivots in the old thrust balance were simply not designed to operate under torques as large as those produced by the DCF's mass. The new design must ensure that all the critical components have no difficulty supporting thruster weights of up to 40 newtons.
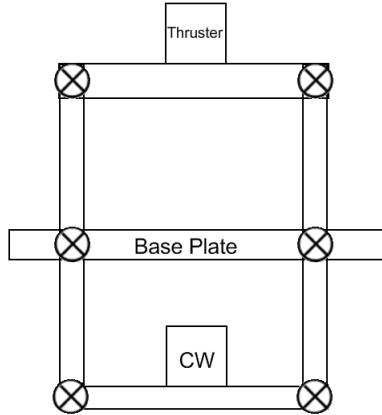
Figure 3.1: Inverted-pendulum style thrust balance for the SPL. It is supported by the base plate, with the thruster sitting on the top plate and the counterweight (CW) sitting on the bottom plate. This a side view, and it should be noted that there are a total of four legs, two of which cannot be seen from this angle.

3.2 Design Selection

The design chosen for the SPL thrust balance most closely resembles the inverted-pendulum type of stand, but includes some alterations to meet the design requirements. Shown in figure 3.1 is an initial sketch of the idea proposed by Professor Manuel Martinez-Sanchez at MIT.

The inverted pendulum style was chosen because of the balance's ability to produce a translation, or parallel displacement, as opposed to a rotation under thrust. This is done by including flexible points of known stiffness at both the top and the bottom of the stand. Now, any up or down shift in the thrust line does not affect the amount of displacement the balance experiences under the same thrust force. This also allows the engine to remain horizontal as the stand tilts, keeping the thrust in a known angular direction and reducing the uncertainty in the stand's measurements.

This inverted pendulum thrust balance includes a counterweight, a feature typically found in torsional balances. It has the effect of removing the sensitivity to base vibrations by creating a statically balanced design. The counterweight also removes the gravity term from the denominator of the equation for the displacement. This makes the stand more sensitive, meaning it makes the balance displace more under a given force. The equations below show the relationship between displacement and

thrust force for the inverted pendulum with a counterweight. A small angle approximation is assumed in the calculation.

$$\Sigma\tau = 0 = (F_T + mg\theta)\,\ell - mg\ell\theta - k\theta \tag{3.3}$$

$$\theta = \frac{F_T\ell}{k} \tag{3.4}$$

since $x = \ell\theta$

$$x = \frac{F_T\ell^2}{k} \tag{3.5}$$

This equation shows that the stand will displace more (be more sensitive) if the pivot stiffness is reduced or if the pendulum arm length is increased, so it has a sensitivity on the same order as the torsional balance (independent of gravity). Again, it makes sense to increase the arm length as much as possible to improve the balance's responsiveness to a force. However, increasing the arm length will make the thrust balance taller and it must fit within the confines of the SPL vacuum chamber. AS-TROVAC is cylindrical in shape, with an inner diameter of 1.38 meters. It also has a metal shelf inside, which provides a flat platform to rest objects inside the chamber. The distance between the metal shelf and the top of ASTROVAC is approximately 1.13 meters. Ideally, the thruster should be about level with the window ports in the chamber, which sit about 69 centimeters from the bottom. That puts the ports about 44 centimeters from the metal shelf. This was the length chosen for the pendulum's legs (from top plate to bottom plate), knowing that it would center the thruster almost directly between the top and bottom of ASTROVAC, as far from the walls as possible. It should also be noted that the SPL thrust balance was given four pen-

30
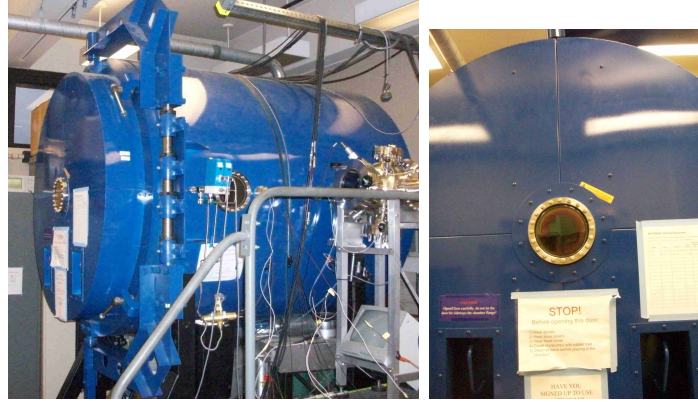
Figure 3.2: Pictures of the Space Propulsion Lab's ASTROVAC facility.

dulum arms, rather than the more traditional choice of just one arm. This helped meet the requirement of supporting the weight of the thruster. Now, each arm and its corresponding pivot point needs only to support a fourth of the thruster's total weight rather than all of it. The four arm design also improves lateral stability .

To reduce the cost and complexity of the project, the bottom pivots were replaced with a thin piece of sheet metal. Since the counterweight exerts a force that creates tension at these points, the metal could be relatively thin (low stiffness) and still hold without breaking. This would not work as an appropriate substitute for the top pivot points, since they would be in compression holding the weight of the thruster. Sheet metal pieces at the top would need to be fairly thick (high stiffness) to support the 4kg mass. A high stiffness would not allow these points to bend, preventing the thrust balance from undergoing a translational motion when the stand displaces. For an analysis of the thickness needed for thin sheet metal connections at the top plate and bottom plate, see Appendix A. A schematic with thin sheet metal replacing the bottom pivot points is shown in figure 3.4.

The bottom of the thruster's support frame is approximately 3.5 inches by 3.5 inches. The top and bottom plates of the thrust balance were designed to be just large enough to accommodate the thruster's frame at about 4.5 inches by 4.5 inches. Making the plates any larger would have just added unnecessary weight to support.
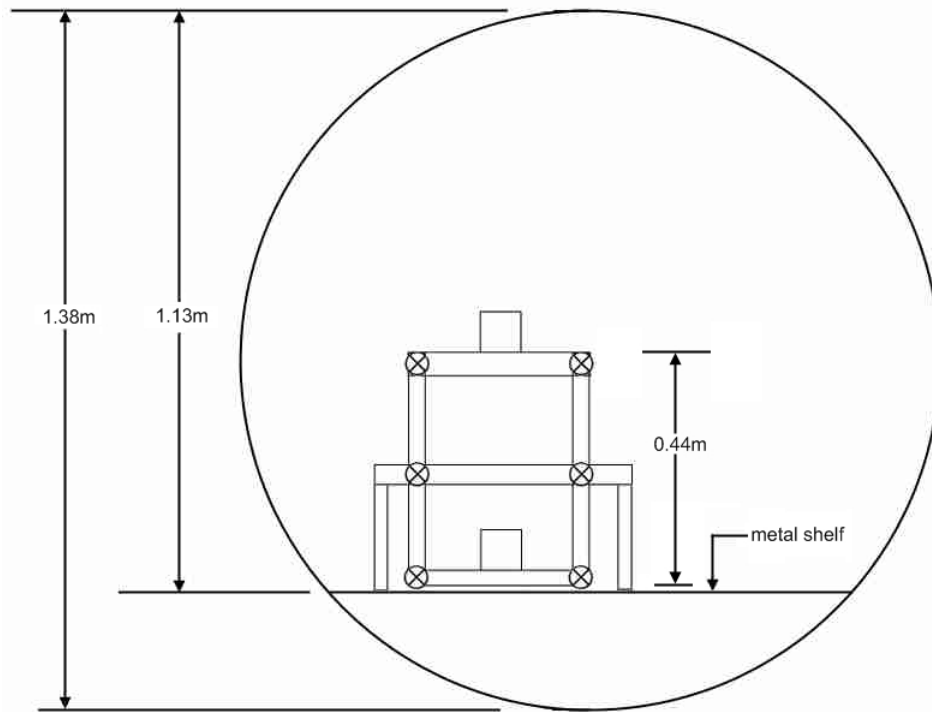
Figure 3.3: Dimensions of the chamber and thrust balance.
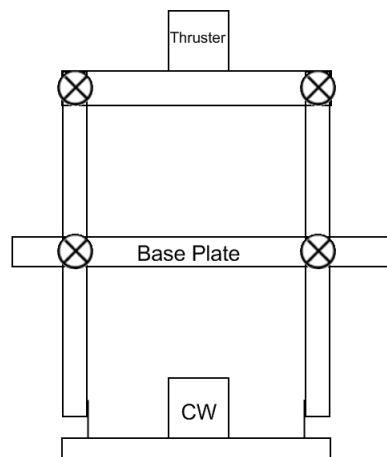
Figure 3.4: Evolution of the thrust balance design to include thin sheet metal as opposed to just flexible pivots at the bottom plate connections.
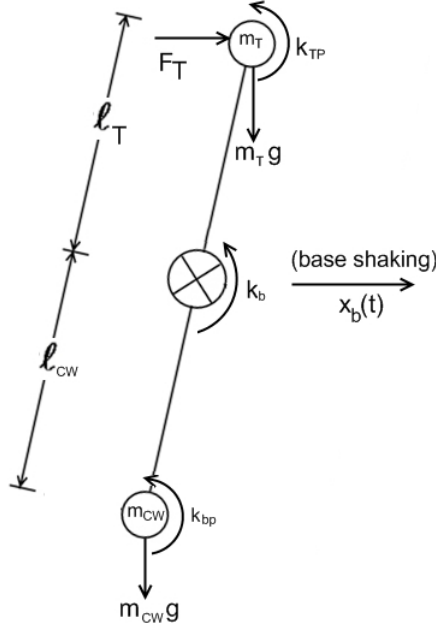
Figure 3.5: A simple, linear model of the inverted-pendulum balance including a counterweight.

3.2.1 Linear Model and System Dynamics of the SPL Thrust Balance

The linear model of the inverted-pendulum thrust stand is shown in figure 3.5, with the forces from weight, thrust, and pivot stiffness included. The dynamics of this system can be described by the following equations in the horizontal direction:

$$m_T \left(\ddot{x}_b + \ell_T \ddot{\theta} \right) = - \frac{\left(k_{TP} + \frac{k_b}{2} - m_T g \ell_T \right) \theta + I_T \ddot{\theta}}{\ell_T} + F_T \tag{3.6}$$

$$m_{CW} \left(\ddot{x}_b - \ell_{CW} \ddot{\theta} \right) = \frac{\left(k_{bp} + \frac{k_b}{2} + m_{CW} g \ell_{CW} \right) \theta + I_{CW} \ddot{\theta}}{\ell_{CW}} \tag{3.7}$$

In these formulas, I_T and I_{CW} represent the moments of inertia of the thruster and counterweight, respectively. These two equations can be simplified, then added together to create one equation for the whole system.

$$\left(I_T + m_T \ell_T^2 \right) \ddot{\theta} = - \left(k_{TP} + \frac{k_b}{2} - m_T g \ell_T \right) \theta + \ell_T F_T - m_T \ell_T \ddot{x}_b \tag{3.8}$$

33

$$\left(I_{CW} + m_{CW}\ell_{CW}^2\right)\ddot{\theta} = -\left(\frac{k_b}{2} + k_{bp} + m_{CW}g\ell_{CW}\right)\theta + m_{CW}\ell_{CW}\ddot{x}_b \qquad (3.9)$$

$$\left(I_T + I_{CW} + m_T\ell_T^2 + m_{CW}\ell_{CW}^2\right)\ddot{\theta} =$$
$$-\left(k_{TP} + k_b + k_{bp}\right)\theta + \left(m_T\ell_T - m_{CW}\ell_{CW}\right)g\theta + \left(m_{CW}\ell_{CW} - m_T\ell_T\right)\ddot{x}_b + \ell_T F_T$$
$$(3.10)$$

If the term on the left side of the equation is replaced with a single moment of inertia variable it becomes:

$$I\ddot{\theta} = -\left(k_{TP} + k_b + k_{bp}\right)\theta + \left(m_T\ell_T - m_{CW}\ell_{CW}\right)g\theta + \left(m_{CW}\ell_{CW} - m_T\ell_T\right)\ddot{x}_b + \ell_T F_T$$
$$(3.11)$$

Now the model's sensitivity to a base vibration can be removed if the static moments of the thruster and counterweight are equal. This condition also makes the forces in the vertical direction sum to zero.

$$m_{CW}\ell_{CW} = m_T\ell_T \qquad (3.12)$$

This cancels the gravity torque term as well. The equation now reduces to the following:

$$I\ddot{\theta} = -\left(k_{TP} + k_b + k_{bp}\right)\theta + \ell_T F_T \qquad (3.13)$$

If the small angle approximation is used again:

$$\sin\left(\theta\right) \approx \theta$$

and assuming now $\ell_T = \ell_{CW} = \ell$

$$\theta \approx \frac{x}{\ell}$$

This term can be substituted into equation 3.13 to create an expression in terms of displacement.

$$I\frac{\ddot{x}}{\ell} = -\left(k_{TP} + k_b + k_{bp}\right)\frac{x}{\ell} + \ell F_T \tag{3.14}$$

$$F_T = \frac{I}{\ell^2}\ddot{x} + \frac{k_{total}}{\ell^2}x \tag{3.15}$$

The removal of the base excitation parameter in the system dynamics means that this design meets the criteria of being insensitive to vibrational effects. Taking the Laplace transform produces the final result, a transfer function. The transfer function is a ratio of the output of a system to the input of the system, expressed in the Laplace Domain [15]:

$$F_T = \left(\frac{I}{\ell^2}s^2 + \frac{k_{total}}{\ell^2}\right)X \tag{3.16}$$

$$\frac{X}{F_T} = \frac{1}{\frac{I}{\ell^2}s^2 + \frac{k_{total}}{\ell^2}} \tag{3.17}$$

$$F_T \longrightarrow \boxed{\dfrac{1}{\dfrac{I}{\ell^2}s^2 + \dfrac{k_s}{\ell^2}}} \longrightarrow X$$
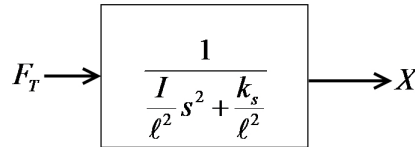
Now a transfer function exists which describes the transient relationship between the input to the system, thrust of the DCF, and the output from the stand, displace-
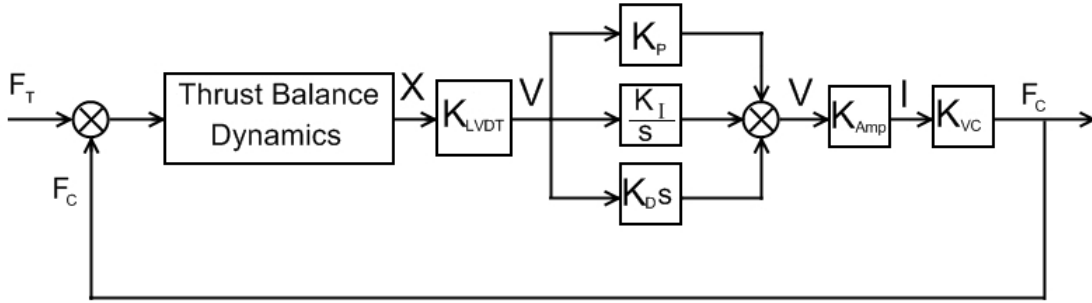
Figure 3.6: Block diagram of the active control on the SPL thrust balance.

ment. This describes the system dynamics of the inverted-pendulum design without any sort of active control. In the next section, it will be shown how this system output of displacement is transformed into a counter force to bring the stand back to a situation of equilibrium, where the displacement is zero.

3.2.2 Block Diagram

The overall goal of the work in this thesis is to measure the thrust force and not just the displacement of the stand. Since the thrust force is unknown, one technique of finding it is to produce a "neutralizing" force which, when opposing the thrust force, pushes the balance back to zero displacement. The neutralizing force is known, and when it pushes the balance back to equilibrium it should be proportional to the value of the unknown thrust force. To accomplish this neutralizing act, three items are required: a sensor that can measure the displacement, software that can determine the appropriate amount of force to supply, and an actuator that can supply the neutralizing force. Although it will be discussed in greater detail later in this chapter, right now it is sufficient to say that a device called a linear variable differential transformer (LVDT) can be used to measure the balance's displacement and produce a corresponding voltage signal. The voltage signal can be manipulated by interactive control software created in Labview, and an appropriate electrical signal can be sent from the software to a simple actuator that creates a force, like a voice coil. This process is outlined in the block diagram shown in figure 3.23.

In figure 3.23, K_{LVDT} represents the sensor, the three blocks in parallel represent

36

the control software, and K_{VC} represents the actuator. The proportional gain between the voice coil and PID control software represents an amplifier circuit, a piece of hardware which would ensure the signal being sent to the voice coil is adequate enough (has enough current) to create a force. Using this block diagram, a relationship between the thrust force and the neutralizing force can be developed. This equation describes the dynamics of the system under active control, and can be used to measure characteristics like response time to an input thrust. Such information can be useful if the thrust is not considered to be constant throughout the test. Mathematically, a transfer function relating the thrust force to the neutralizing force can be developed with relative ease from the diagram in figure 3.23:

$$F_C = K_{VC} K_{Amp} \left[\left(K_P + \frac{K_I}{s} + K_D s \right) K_{LVDT} \left(\frac{1}{\frac{I}{\ell^2} s^2 + \frac{k_{total}}{\ell^2}} \right) \right] (F_T - F_C) \quad (3.18)$$

$$F_C + K_{VC} K_{Amp} K_{LVDT} \left[\frac{K_P + \frac{K_I}{s} + K_D s}{\frac{I}{\ell^2} s^2 + \frac{k_{total}}{\ell^2}} \right] F_C = K_{VC} K_{Amp} K_{LVDT} \left[\frac{K_P + \frac{K_I}{s} + K_D s}{\frac{I}{\ell^2} s^2 + \frac{k_{total}}{\ell^2}} \right] F_T$$
$$(3.19)$$

$$\frac{F_C}{F_T} = \frac{K_{VC} K_{Amp} K_{LVDT} \left[\frac{K_P + \frac{K_I}{s} + K_D s}{\frac{I}{\ell^2} s^2 + \frac{k_{total}}{\ell^2}} \right]}{1 + K_{VC} K_{Amp} K_{LVDT} \left[\frac{K_P + \frac{K_I}{s} + K_D s}{\frac{I}{\ell^2} s^2 + \frac{k_{total}}{\ell^2}} \right]}$$
$$= \frac{K_{VC} K_{Amp} K_{LVDT} \left[K_P + \frac{K_I}{s} + K_D s \right]}{\frac{I}{\ell^2} s^2 + \frac{k_{total}}{\ell^2} + K_{VC} K_{Amp} K_{LVDT} \left[K_P + \frac{K_I}{s} + K_D s \right]} \quad (3.20)$$

$$\frac{F_C}{F_T} = \frac{K_{VC} K_{Amp} K_{LVDT} \left[K_D s^2 + K_P s + K_I \right]}{\frac{I}{\ell^2} s^3 + K_{VC} K_{Amp} K_{LVDT} K_D s^2 + \left(\frac{k_{total}}{\ell^2} + K_{VC} K_{Amp} K_{LVDT} K_P \right) s + K_{VC} K_{Amp} K_{LVDT} K_I}$$
$$(3.21)$$

Now that a general expression for the dynamics of the thrust balance has been

established, the next step is to define some of the constants in the equation. The variable k_{total} will depend on the selection of the pivots, while K_{LVDT} and K_{VC} will depend on the LVDT and voice coil selected for use on the balance. Their selection will be discussed in the next section. The constants K_{Amp} as well as K_P, K_I, and K_D will depend entirely on the control hardware and software chosen. Their selection is discussed in greater detail later in the chapter.

3.3 Construction of the SPL thrust balance

With the design of the thrust balance established, the next phase of the project developed this basic model into a physical, working prototype. This process involved selecting and ordering the flexible joints with the correct stiffness, finding an LVDT and voice coil that would suit the needs of the control system, and producing a CAD model and cutting the metal that makes up the frame of the balance.

3.3.1 Flex Pivot Selection

The important concept to keep in mind while selecting the flexible components that make up the joints on the balance is that they have to be both as frictionless as possible and vacuum safe. This means that no outgassing should occur when the pivots are placed in a low pressure environment. This restricts the number of options available since any pivot or hinge that utilized grease or oil to reduce the friction between parts was automatically eliminated. These types of lubricants outgas significantly in a vacuum environment. The most feasible option is free-flex pivots, which allow rotation in one direction and prevent any sort of lateral or translational motion [14]. These pivots have a very predictable amount of stiffness within a certain angular range, are friction free, and use no lubricants that would create complications in a vacuum environment. These pivots come in two different styles, double ended and cantilevered, shown in figure 3.7.

The cantilevered style pivot allows the two ends to rotate in opposite directions, with a specified stiffness between them as they move. The double ended model

Figure 3.7: The two types of Riverhawk flexural pivots, the cantilever (left) and doubled ended (right)[1].

allows the central shell to rotate in one direction and the two end shells to rotate together in the opposite direction. It was decided that the cantilevered pivots would be suitable for the connections between the four legs and the base of the stand, while the double ended pivots could be used as the attachments between the top plate and the pendulum arms. This would force the front set of legs, as well as the back set of legs to rotate together where they fasten to the top plate. A sketch of this concept is shown in figure 3.8.

This required a total of 6 pivots, two of the double ended type at the top and four of the cantilevered type at the base. The next task was to determine what amount of stiffness these pivots should have to provide the system the sensitivity it needs. The process of determining the appropriate stiffness for the balance started with the system dynamics equation developed in the previous section.

$$F_T = \frac{I}{\ell^2}\ddot{x} + \frac{k_{total}}{\ell^2}$$

In this case, only a constant force was considered, so the acceleration term was removed. Also, the individual stiffness for the double ended pivots, cantilevered pivots, and thin sheet metal attachments should be substituted into the equation.
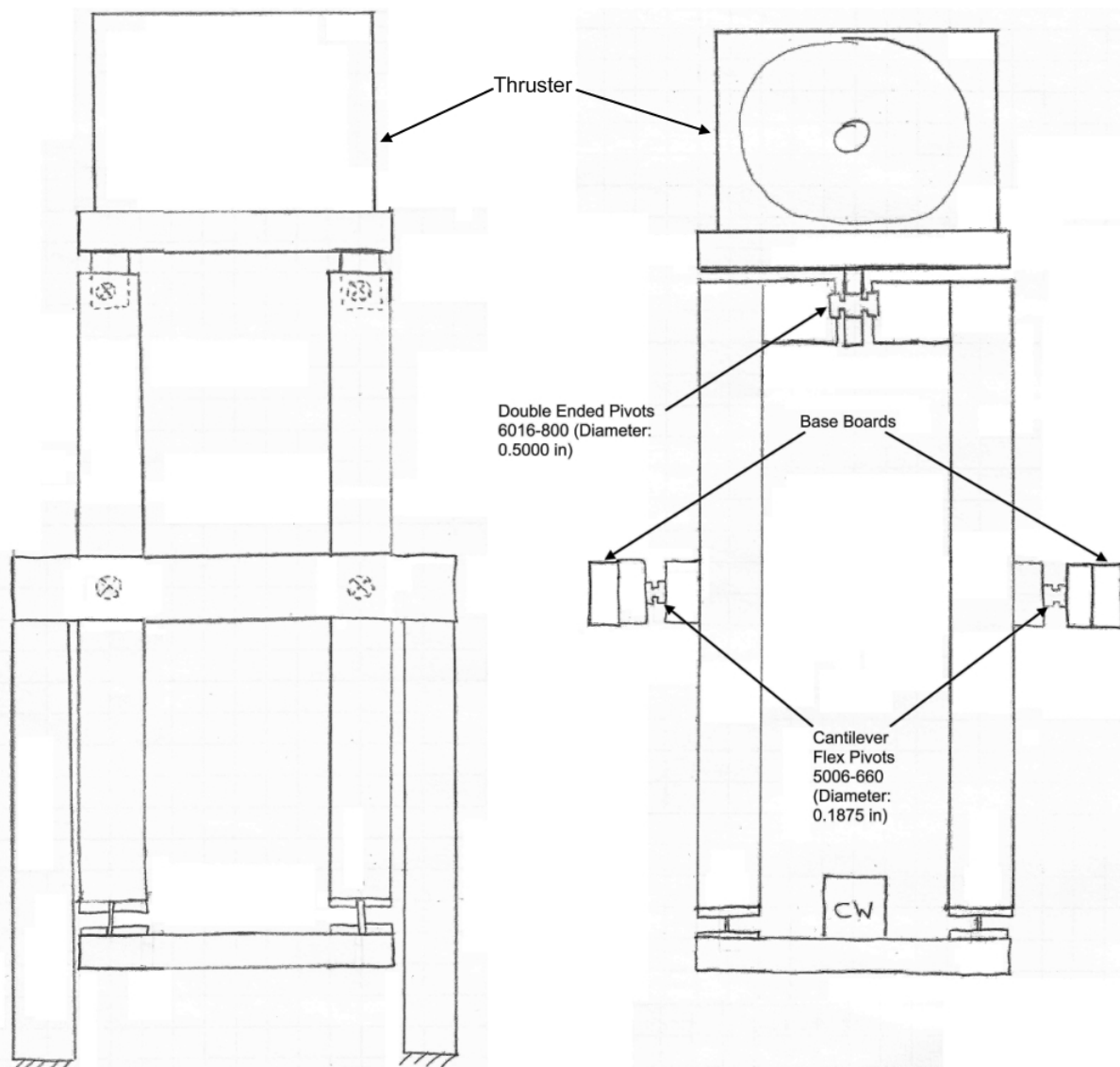
Figure 3.8: Initial sketch of the thrust balance showing the locations of the pivots.

$$F_T = \left(\frac{2k_{double-ended}}{\ell^2} + \frac{4k_{cantilevered}}{\ell^2} + \frac{4k_{sheetmetal}}{\ell^2} \right) x \qquad (3.22)$$

It was previously determined that the length of each arm would be 44 cm, or that $\ell = 22$cm. It is also known that the maximum thrust of the DCF is probably no greater than 20mN [5]. It was decided that under such a force, the deflection should be on the order of about one degree, to keep the small angle approximation relevant in the analysis and to prevent operating range issues in other devices on the balance, such as the LVDT. Keeping the small angle approximation, a one degree deflection translates to a horizontal displacement of just over 3mm.

$$x = \ell\theta = (0.22m) \left(1^o \frac{\pi}{180^o} \right) = 0.00384m = 3.84mm$$

Using the maximum value of thrust and the desired displacement this force produces allows for a calculation of the total stiffness. The overall stiffness of the system now becomes:

$$
\begin{aligned}
k_{total} &= 2k_{double-ended} + 4k_{cantilevered} + 4k_{sheetmetal} = \frac{F_T\ell^2}{x} \\
&= \frac{(0.020N)(0.22m)^2}{0.00384m} = 0.2521\frac{N-m}{rad}
\end{aligned}
$$

Next, the assumption was made that the stiffness from the sheet metal would be much less than the stiffness in the pivots. This was based on the fact that the sheet metal could be made very thin and still hold the weight of the bottom plate. A closer examination of this is given in Appendix A. With that simplification, the sheet metal could be removed from the equation and the total stiffness of the two double ended pivots and the four cantilevered pivots now becomes $0.2521 \frac{N-m}{rad}$. The data sheets in Appendix C show the list of available pivots from Riverhawk Company, one of the primary manufacturers of these flexures[1]. The closest matches were found to be model 6016-800 for the double ended pivots and 5006-660 for the cantilevered pivots.

Although the manufacturer lists their stiffness values in English units, these can be easily converted to metric:

$$6016 - 800 \Rightarrow k = 0.0142\frac{in-lb}{deg} \times \frac{0.0254m}{1in} \times \frac{4.448N}{1lb} \times \frac{180deg}{\pi} = 0.0919\frac{N-m}{rad}$$

$$5006 - 660 \Rightarrow k = 0.0037\frac{in-lb}{deg} \times \frac{0.0254m}{1in} \times \frac{4.448N}{1lb} \times \frac{180deg}{\pi} = 0.0240\frac{N-m}{rad}$$

Just as a check, these values can be put back into the equation to see how much displacement they will allow under a force of 20 mN:

$$
\begin{aligned}
x &= \frac{F_T}{\left(\frac{2k_{double-ended}}{\ell^2} + \frac{4k_{cantilevered}}{\ell^2}\right)} \\
&= \frac{0.020N}{\frac{1}{(0.22m)^2}\left(2 \times 0.0919\frac{N-m}{rad} + 4 \times 0.0240\frac{N-m}{rad}\right)} = 0.00346m = 3.46mm
\end{aligned}
$$

These pivots turn out to be a very good choice, putting the actual displacement at 3.46mm. The final requirement of the pivots is that they be able to bear the weight of the DCF, or similar thrusters, and still perform as expected with relatively constant stiffness. The 5006-660 cantilevered pivots are rated to operate successfully under a maximum of 12.2 pounds of force each, or 54.3 Newtons each. The DCF has a mass of about 4kg, so its total weight is about 39.2 Newtons. With the weight of the DCF split four ways among the cantilever pivots, they can support the weight of the DCF with a safety factor of up to 5.5. The 6016-800 double ended pivots are rated to operate under a force of 35.4 pounds of force each, or 157.5 Newtons each. Again, these pivots easily support the weight of the DCF, with a safety factor of around 8. The weight of the DCF does not come close to the operating limits of these pivot models. The pictures in figure 3.9 show the models that were selected. It should be noted that the double ended pivot is significantly larger than the cantilevered
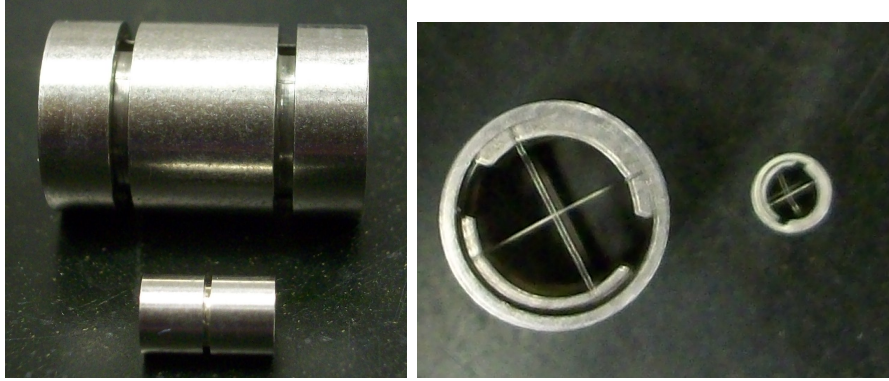
Figure 3.9: The actual flexible pivots chosen for the SPL thrust balance. Picture includes one of the cantilevered (5006-660, smaller pivot) and one of the double ended (6016-800, larger pivot) flexures.

one. The double ended pivots are approximately half an inch in diameter while the cantilevered pivots are about 3/16 of an inch.

3.3.2 CAD Modeling and Assembly

The majority of the CAD modeling and machining was done by MIT graduate student Ryan Daspit. From the sketches shown in figure 3.8, Daspit produced a working CAD model with technical drawings. Figures 3.10 and 3.11show pictures of the CAD model he produced.

The pieces of the balance, such as the base, pendulum legs, and the top and bottom plates were machined directly by Ryan Daspit. Many of the more intricate parts, such as the clamps, which held the ends of the flexible pivots, had to be machined by the MIT Central Machine Shop because of the high precision tools required to shape them. A picture of one of the clamps which holds the cantilevered pivots is shown in figure 3.12. Its edges measure about 3/4 in by 3/4 in, with a hole in the middle set to the diameter of the cantilevered pivot, 3/16 in. The slot is there so that the clamp can be tightened around the pivot through a screw driven into the hole on the top. The clamps for the double ended pivots were similar in design, with slightly larger dimensions.

The assembly of the balance had to be done with a great deal of care. The clamps had to be tight enough to grip the pivots, but at the same time not so tight that they
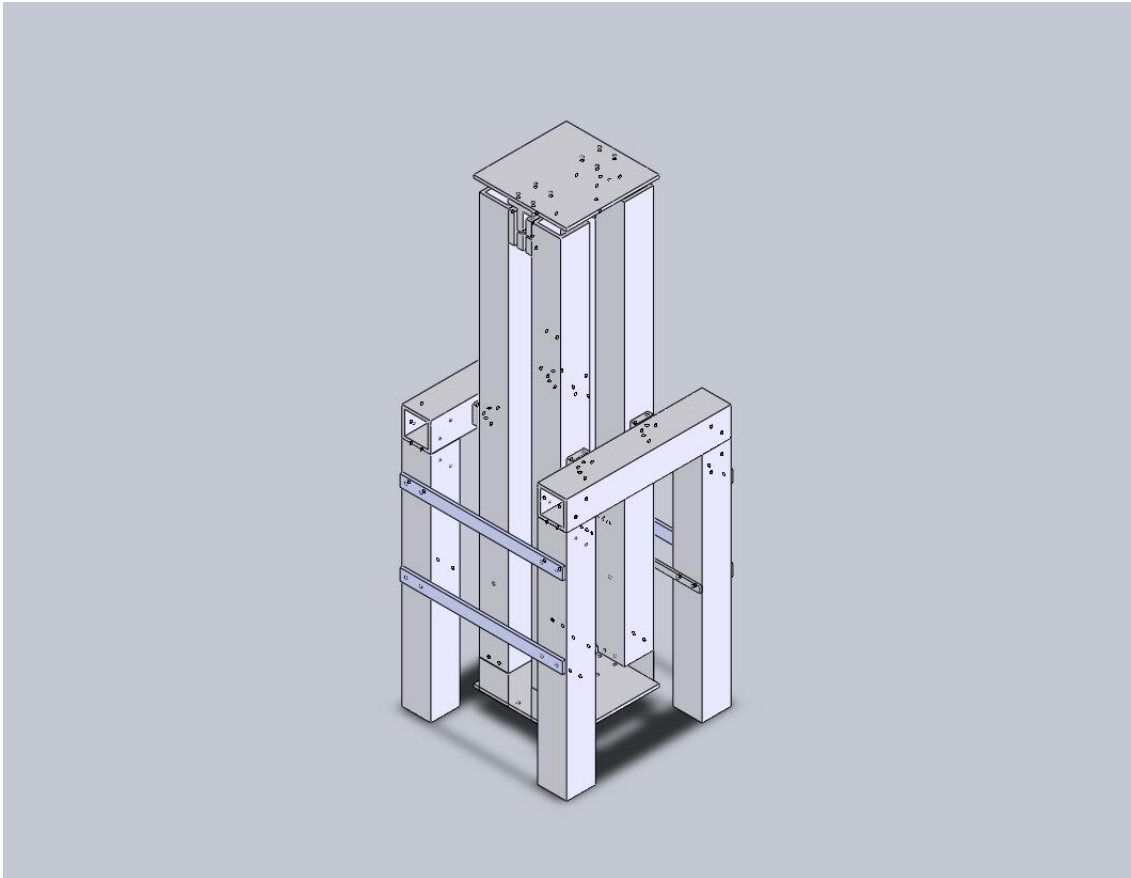
Figure 3.10: Isometric view of Ryan Daspit's CAD model of the SPL thrust balance.
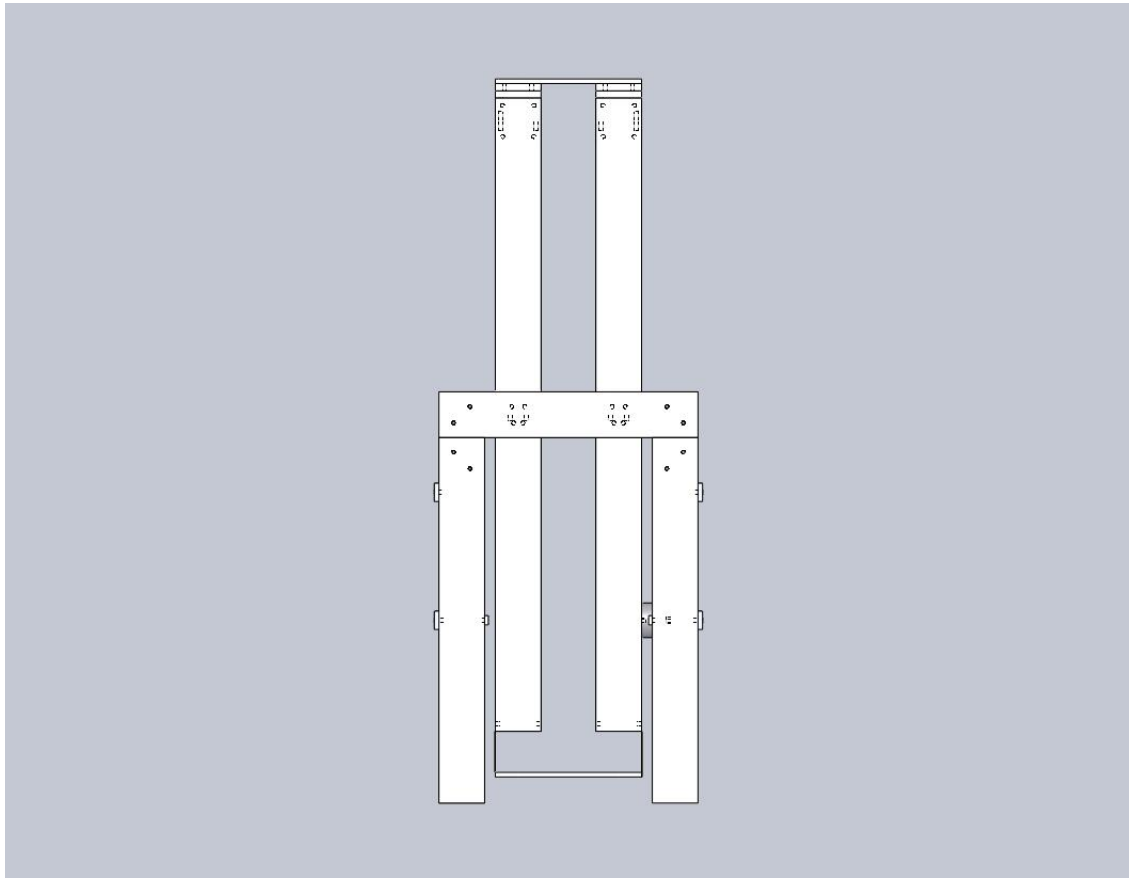
Figure 3.11: Side view of Ryan Daspit's CAD model of the SPL thrust balance.
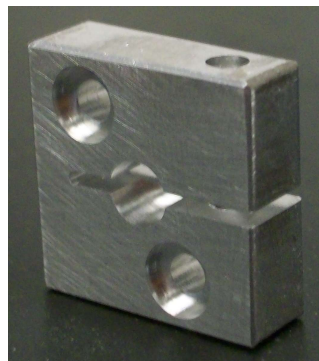
Figure 3.12: Clamping device used to hold the flexible pivots in place.
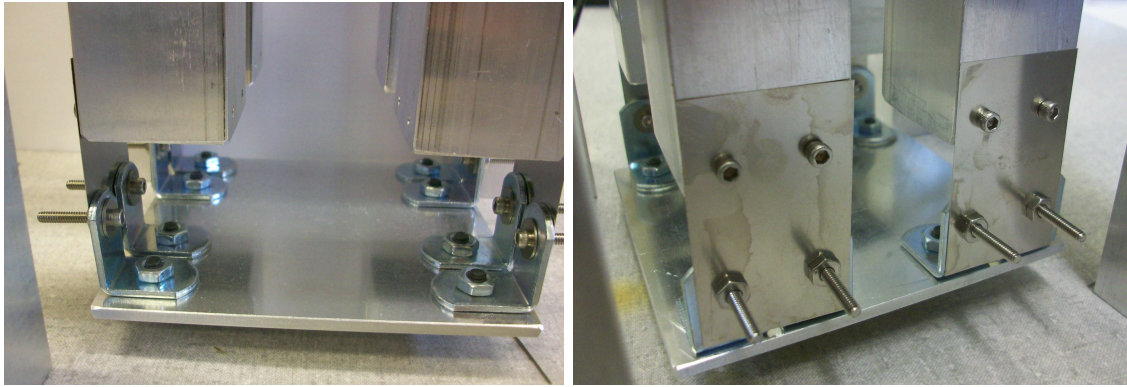
Figure 3.13: Attaching the sheet metal to the lower legs and bottom plate by screws and brackets.

would put excessive force on the flexures and damage them. The pivots also needed to be assembled such that they were not clamped into place at varying rotational angles. Doing so would have added a preloaded stiffness to one or more of the pivots, even when the stand was not experiencing a thrust force.

The final challenge in the assembly of the thrust stand was attaching the bottom plate. There was no easy way to clamp the top and bottom part of the sheet metal, so the top of each piece was just attached by a set of screws to the side of the pendulum legs and the bottom of each piece was attached to the lower plate through a set of brackets. This is shown in the pictures of figure 3.13. This method of attachment was unexpected, but, fortunately, did not seem to have a significant impact on the thrust balance's overall stiffness, and thus, no effect on the sensitivity.

Figure 3.14 shows some pictures of the balance in its final, assembled state. The pictures also show the LVDT and two voice coils attached to the balance. These components will be explained further in the next subsection.

3.3.3 Instruments, the Linear Variable Differential Transformer and Voice Coil

Clearly visible in the pictures of the assembled thrust balance from the previous section are the linear variable differential transformer (LVDT) and two voice coils. These are the key components to the active control system which is responsible for

46
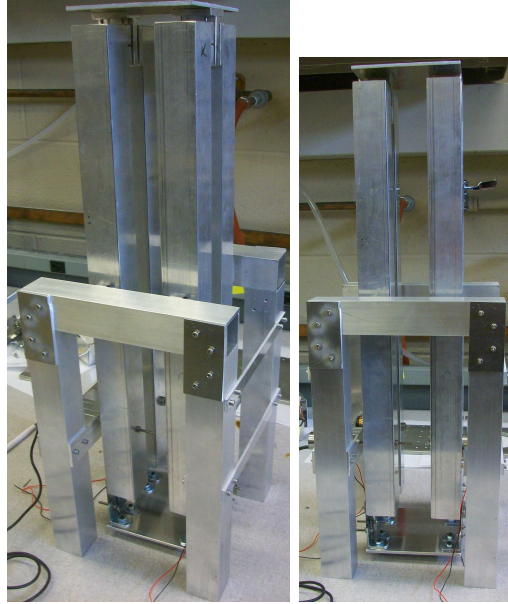
Figure 3.14: Thrust Balance in final, assembled configuration.

measuring the thrust from the DCF. This section will describe how they work and why they are a necessary part of the SPL thrust balance.

The LVDT is a sensor which measures linear displacement. It is placed on the counterweight side (lower side) of the balance to keep it far from the plume of the DCF. The plume from the thruster is an ionized gas which can create significant signal error in the LVDT if not shielded. The plume can also erode the instrument over time, however, such erosion is mitigated by keeping the LVDT near the counterweight side of the thrust balance. To measure displacement, the LVDT uses a ferromagnetic core that is free to move vertically through the hole in the middle of the cylinder. When the core moves, it induces a voltage in the solenoid coils that lie around the central tube. When read, this voltage can give a value of the displacement through a proportionality constant.

$$V_{out} = K_{LVDT} X_{in} \tag{3.23}$$

The LVDT selected was the same as the one used on the old SPL thrust balance. This LVDT was chosen because it was deemed reliable in previous testing where it measured small displacements under vacuum conditions. The model selected was the

47
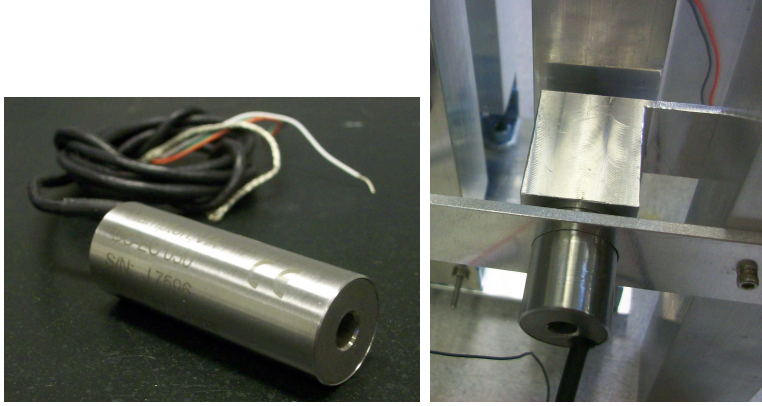
Figure 3.15: Schaevitz Sensors LVDT (model 050 DC-EC).

050 DC-EC, developed by Schaevitz Sensors, pictured in figure 3.15. Its proportion-ality constant is on the order of 8 volts per millimeter. A copy of the full datasheet can be found in Appendix C.

In addition to the LVDT, there are two voice coils. A voice coil is made up of two pieces: a coil of wire and a magnetic housing. When a current passes through the coil, it either attracts or repels the magnet. The primary, or control voice coil, works with the LVDT and control software to provide that "neutralizing" force to the thrust balance that brings it back to an equilibrium position. The secondary, or calibrating voice coil, is part of the drift correction system in vacuum, and its role will be explained more in depth in the calibration section of this paper. The force each voice coil produces is the square root of the power (voltage times current) put into the voice coil multiplied by a proportionality factor.

$$F_{out} = K_{VC}\sqrt{P_{in}} \qquad (3.24)$$

The voice coil selected was again the same as the one chosen on the old thrust balance because it was known to be reliable for this type of application. The coil chosen was made by BEI Kimco Magnetics and the specific model was LA10-08-000A. It had a proportional constant of $1.15\frac{N}{\sqrt{Watt}}$. It is pictured in figure 3.16 and a copy of the datasheet is also located in Appendix C.
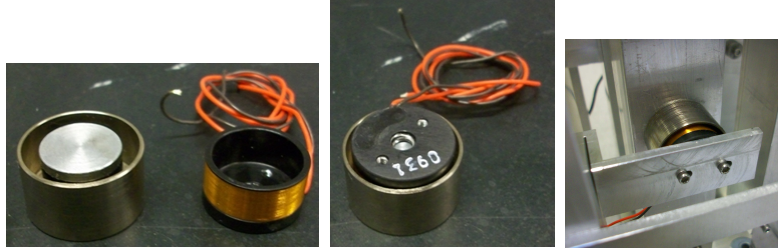
Figure 3.16: BEI Kimco Magnetics voice coil (model LA10-08-000A).

Figure 3.17: Metal housing of the thrust balance control box.

3.4 Control System

Now that the sensor and actuator have been described, the inner workings of the control system is next. Its purpose is to interpret the LVDT voltage and transform it into an appropriate signal for the voice coil. This is accomplished through electronic hardware located in what has been designated the "control box" and a Labview computer algorithm known as the "control software." Both were originally designed by MIT research associate Randy Leiter, but changes had to be made to the hardware and software in order for it to function properly with the new thrust balance. In the next two subsections, the control box and Labview algorithm will be explained to establish a better understanding of how they function.

3.4.1 Control Box Hardware

Figure 3.17 shows the control box as it appears on the outside. It has a 9 pin connector, a USB port, an on/off switch, a fuse, and a power cord plug. The 9 pin connector on the box interfaces with the 9 pin terminal on the thrust balance through a cable. This is how electrical signals travel between the box and the components on the balance (the LVDT and two voice coils). The USB port connects to the lab's desktop computer through a USB cord. This is how signals are sent between the software algorithm in Labview and the control box. Removing the top of the control box (see figure 3.18), reveals that there are only three distinct items inside. Tracing the wire from the USB port leads to the first key element, a Labview data acquisition card (or DAQ). Also visible are a pair of identical circuit boards, and just beneath these is a set of power supplies. These power supplies are controlled by the on/off switch found on the top of the box. The two circuit boards are amplifiers, and they work to increase the voltage and current of electrical signals coming from the DAQ card.

The DAQ card is the most crucial component found in the control box. As illustrated in figure 3.19, it is a model NI 6009, manufactured by National Instruments and designed to interact with a Labview program through the port on its upper surface. The DAQ card receives its power through this computer connection, not through the power supplies in the box. Therefore, the switch on the box can be "off", but if the DAQ card is plugged into the computer via the USB connection, it should be turned "on." The DAQ can send and receive analog or digital commands through the screw terminals on its sides (analog ports on the right side, digital on the left). The LVDT produces an analog voltage and the voice coils operate under analog signals, therefore only the analog terminals were utilized for this project.

The NI 6009 has a total of four analog inputs and two analog outputs. The outputs can send a signal between 0 and 5 volts, with very low levels of current, about 5 milliamps. This low level of current is not enough to drive the voice coils on the thrust balance, which is why two amplifying circuits are included in the box. A
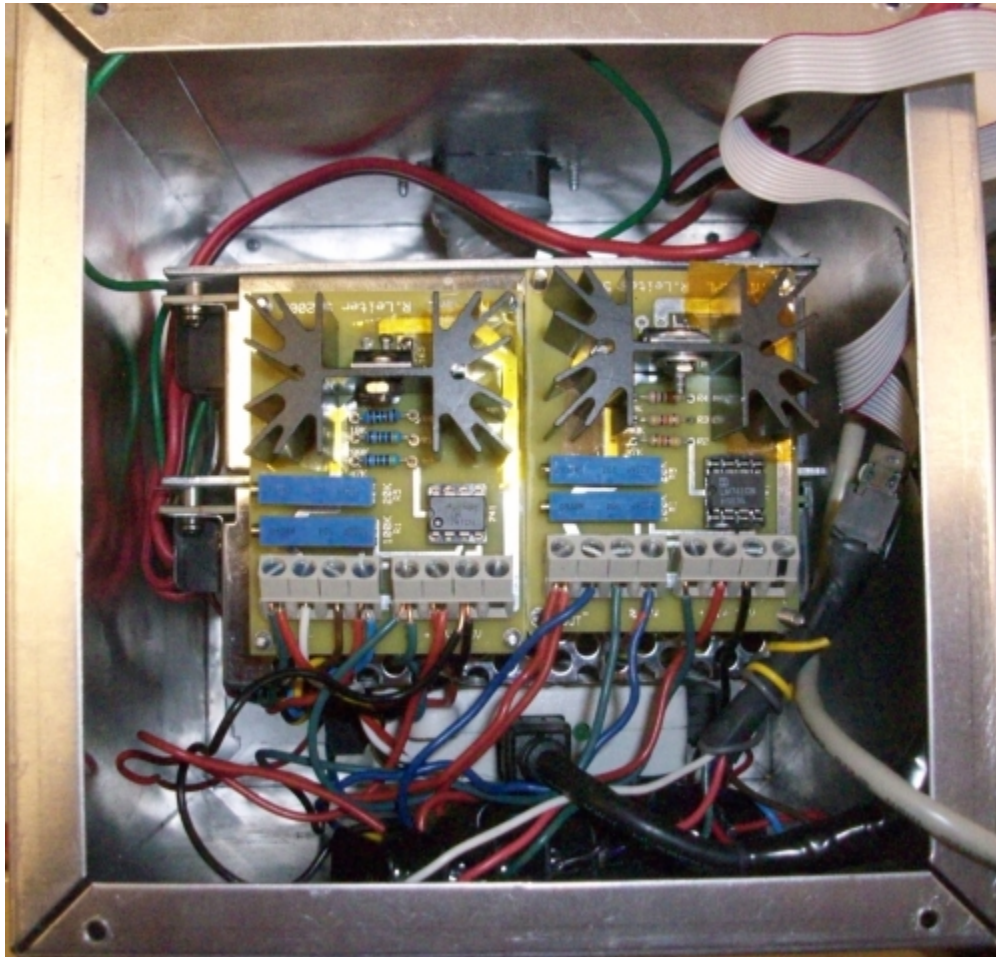
Figure 3.18: Looking inside the thrust balance control box. The two circuit boards in the middle are the amplifiers. The DAQ card is at the bottom of the picture, partially covered by wires. The power supplies sit underneath the circuit boards and are not clearly visible from this angle.

Figure 3.19: National Instruments DAQ card, model NI 6009.

full data sheet for this DAQ card is included in Appendix C.

The two power supplies are identical models. They receive an AC input through an ordinary computer power cord which connects to a wall outlet. The power supplies included in the box are providing energy to run the two amplifying circuits, as well as the LVDT, which all require a DC voltage of ±15 volts. The power supplies are also connected in series to provide a "common ground", as shown in the diagram of figure 3.20.

The original control box built by Randy Leiter contained just one amplifier circuit, but, due to the inclusion of a second voice coil on the SPL thrust balance, a second circuit was built and added into the box. Each of these amplifying circuits connects to one of the analog outputs from the DAQ card, working to alter the current and adjust the voltage to appropriate levels capable of driving the voice coils. Each circuit board has two op-amps on it. The first is an LM741, the op-amp without a large heat sink in figure 3.21. This op-amp takes the 0 to 5 volt signal from the DAQ card and shifts it to a scale of -2.5 to +2.5 volts. When the analog output from the DAQ commands 5 volts, it becomes a 2.5 volt signal after going through the LM741. Likewise, 2.5 volts from the analog output of the DAQ becomes 0 volts, and 0 volts from the DAQ card becomes -2.5 volts. The reason for this shift is that it allows
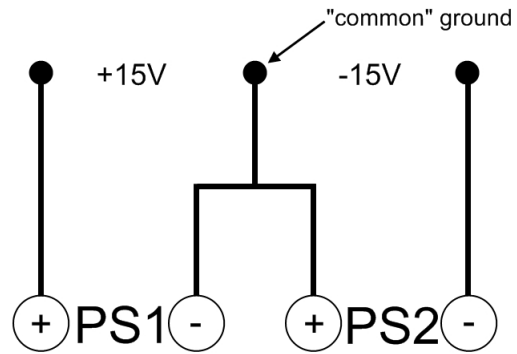
Figure 3.20: Diagram showing the series connection between the power supplies in the control box which creates a floating ground.
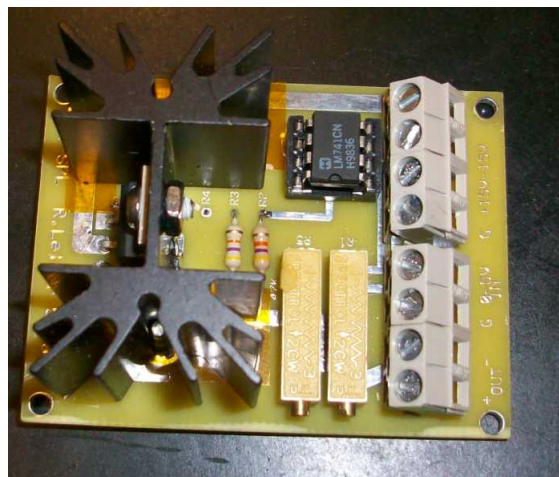
Figure 3.21: One of the two amplifying circuits found in the control box. The large black colored metal object is the heat sink, which is attached to the L165 Op-Amp.
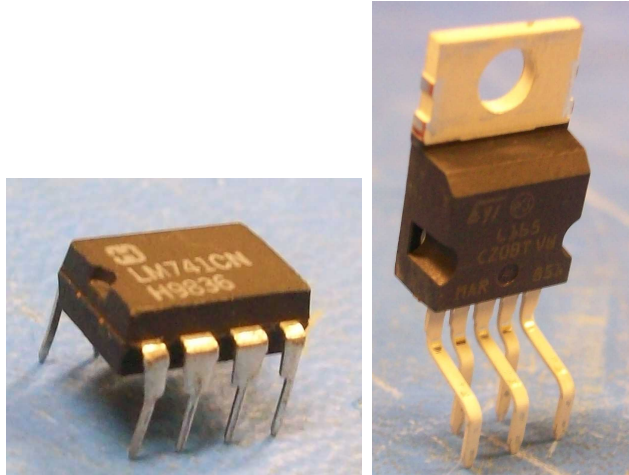
Figure 3.22: Pictures of the two op-amps used in the amplifying circuit, the LM741 (Left) and the L165 (Right).

the voice coils to receive currents going in either direction, giving them the ability to generate either a push or a pull on the thrust stand, depending on what is required to reach the equilibrium position.

After going through the LM741, the signal from the analog output on the DAQ then reaches the L165 op-amp. This is the op-amp attached to the large heat sink in the picture of the circuit board. The L165, also shown in figure 3.22, is much more powerful than the LM741, and can increase the voltage as high as ± 16 volts with a current as high as 2 amps. For this application, the voltage is actually reduced to about ± 0.8 volts by the L165. This is accomplished by tuning the potentiometers (adjustable resistors) that connect to the various pins of the op-amp. A full circuit diagram of the two op-amps and the resistors which govern how they manipulate the DAQ card signal are included in Appendix D. The data sheets for the op-amps themselves are also found in Appendix D. A wire diagram showing all of the connections inside of the control box is given in Appendix E.

3.4.2 Control Software

The extensive Labview block diagram seen in figure 3.23 is the algorithm that drives the thrust balance; it reads voltage signals from the LVDT and calculates the appropriate voltages to send to the control voice coil. This subsection will take a step by
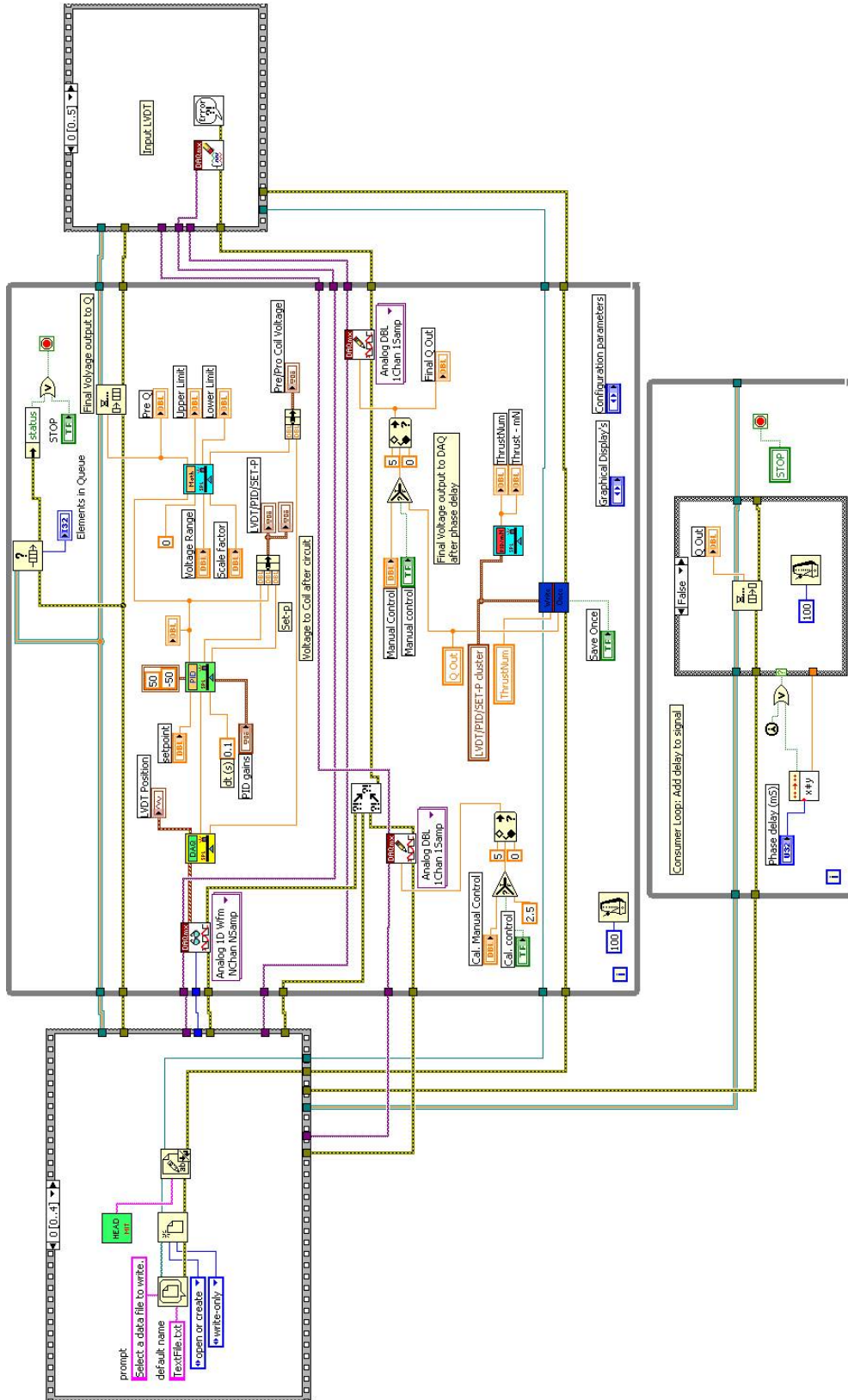
Figure 3.23: Block diagram of the Labview control software.
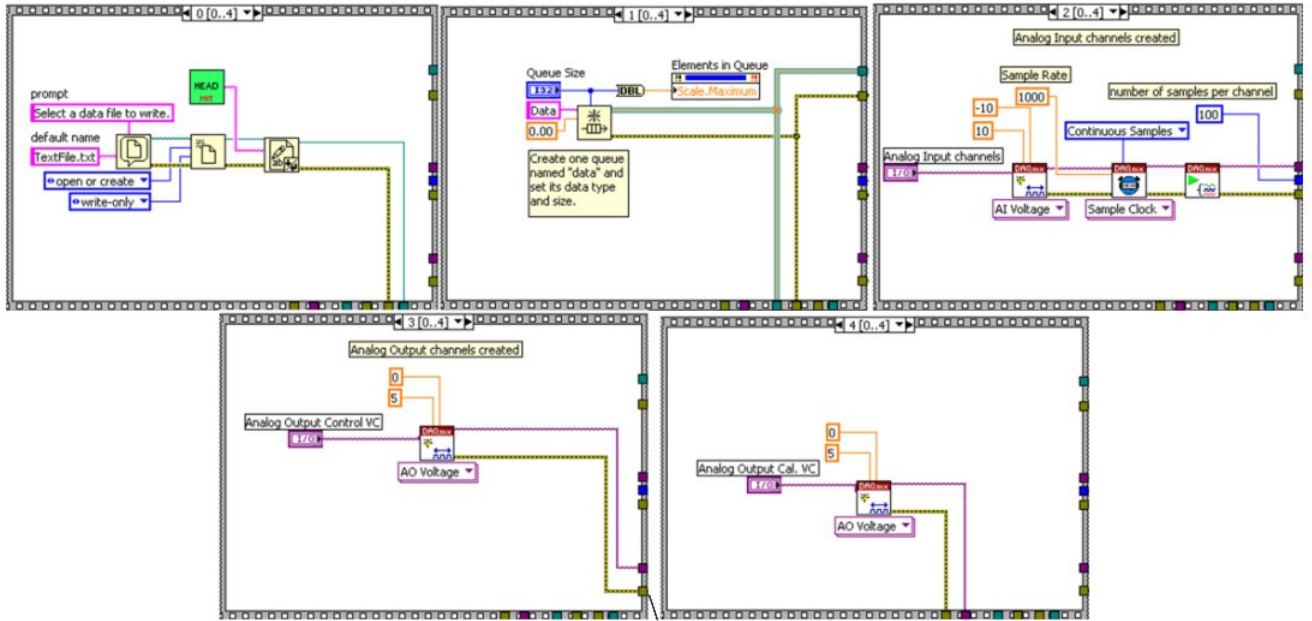
Figure 3.24: Each frame of the first stacked sequence.

step look through the program and explain the details behind how it functions.

The software begins with commands that come out of the stacked sequence structure on the left in figure 3.23. Stacked sequence structures contain a set of frames, each with separate bits of code, that execute in numerical order. The frames are laid out, in order, in figure 3.24. The first frame in the opening sequence (frame zero) sets up an Excel data file to record information, including the control voice coil voltage and LVDT position. This data file will be important later during the creation of a calibration curve and thrust calculation. Frame one sets up a queue system architecture to store commands. This queue system is a key component of the phase delay in the program, which will be explained later. Frame two initializes the analog input channels of the DAQ card, and frames three and four load the DAQ card's analog outputs for the control voice coil and the drift correcting voice coil, respectively.

After the stacked sequence is complete, the two big while loops (the gray boxes in the middle of figure 3.23) run simultaneously. For consistency, first the top loop will be discussed at length, followed by the bottom loop. The top while loop reads in the analog inputs from the stacked sequence and turns them into a single data stream, or a single waveform, using the "DAQmx Read" block. This single waveform

56

is sent on to the "DAQ Input From Balance" block, which parses the data stream and converts it to double variable format. In this block, the LVDT signal is also scaled up to a range between 0 and 100. From there, the scaled LVDT signal is plotted for the user to view (under the "LVDT position" tab in the user interface) and the double formatted data stream is sent along to the "PID Conditioning" block. Other inputs to the PID Conditioning block include a set point for the LVDT (which should be zero), a time scale, and PID gain values. Optimal performance was obtained for values of 0.020, 0.005, and 0.000 for proportional, integral, and derivative gain, respectively. The PID Conditioning block contains an algorithm called PID.vi, which is part of Labview's control toolkit. The PID Conditioning block outputs three things: the set point, the PID adjusted voice coil signal, and the LVDT signal, all fixed to a -50 to 50 scale. These outputs are first bundled, then turned into a local variable (making them accessible everywhere in the program), and finally plotted to the user interface under the "System Response & PID Feedback" tab. These outputs are also sent along to the "SPL Voltage Math" block. The Voltage Math block takes the PID signal and converts it into a voltage value in preparation for sending it back to the DAQ card as an analog output. Along with this converted PID signal, it outputs limits to prevent the voltage from going outside of the DAQ card's range. This voltage signal is now put into the queue that was initialized back in frame one of the opening stacked sequence structure. The reason for this queue is that the electrical signals traveling from the LVDT to the control box and on to the voice coil do not reach their destinations instantly, but rather, they take a certain finite amount of time. The software can run much faster than these signals can be sent and received, so the algorithm must be slowed to the same speed as the rest of the system. A delay is purposefully added by saving voltage commands in the queue. The process of de-queuing the voltage commands is handled in the lower while loop, and will be discussed shortly.

A few other operations are also occurring in the upper loop. The local variable created after the PID Conditioning block is sent to the "PID Force Convert" block. The output of the Force Convert block provides the voice coil voltage reading, which is displayed in the user interface. The local variable is also fed to the "Write Once"
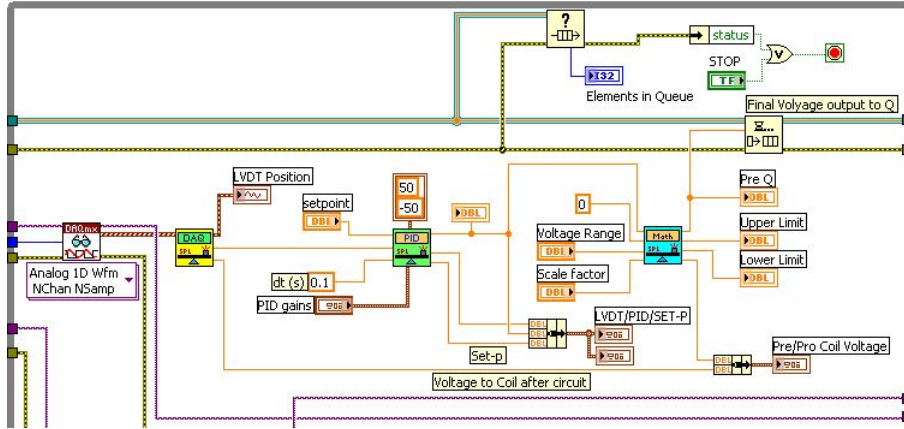
Figure 3.25: Top half of the upper, or "producer" loop.
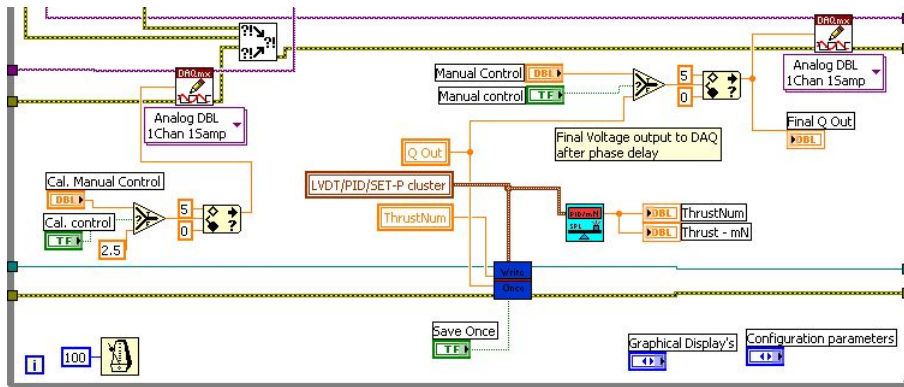
Figure 3.26: Lower half of the upper, or "producer" loop.

block which saves the voice coil voltage to the Excel data file whenever the user clicks the "Save Once" button. Just above and to the left of the "Write Once" block are the controls for the two voice coils. A "Select" block allows toggling between manual and PID control on the control voice coil and power on and off on the drift correcting voice coil.

The upper loop is also nicknamed the "producer" loop, because its primary function is to produce an appropriate voltage for the control voice coil. The lower loop is known as the "consumer" loop, as it takes this resulting voltage and adds a phase delay to it. The lower loop consists of a pair of nested loops. In the outer loop, the user sets the phase delay in milliseconds. The optimal time delay was found to be about 500 milliseconds. The outer loop makes the inner loop wait the specified amount of delay time before executing. The inner loop's only function is to de-queue
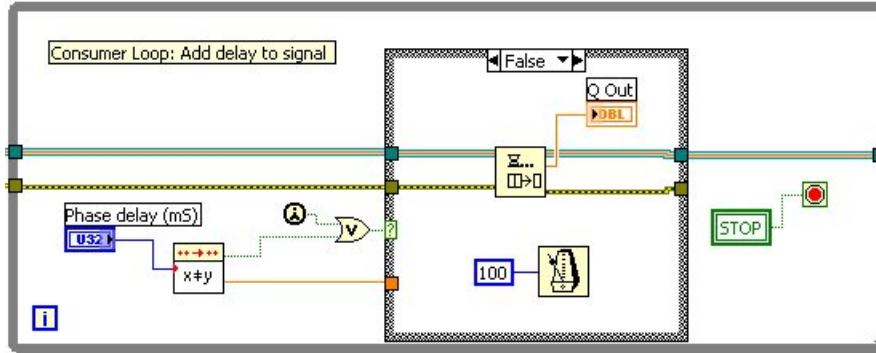
Figure 3.27: The consumer loop, which adds a phase delay to the voltage sent to the control voice coil.

voltage commands one at a time, sending them on to the DAQ as they are removed.

The final step in the software occurs when the user clicks the "System Stop" button on the display interface. This forces both loops to quit and the stacked sequence on the right begins to execute. The first frame (frame zero) in this sequence shuts down the analog inputs to the DAQ card properly, meaning it releases the memory and reconditions the DAQ inputs for the next use. Frames one and two set the control voice coil and drift correcting voice coil voltages to 2.5V each (which becomes 0 after the signal is sent through the control box) and shut the analog outputs down properly. Frame three releases the queue of voice coil voltages, restoring this memory to the computer. Frame four closes the Excel file where the data was collected to keep it from becoming corrupted. Finally, frame five resets the system stop button to false. All six frames can be seen in figure 3.28.

3.5 Calibration System

In order to determine the amount of force that the control system is delivering to neutralize the thrust balance, some means of calibration is necessary to establish a relationship between the control voice coil's voltage and force. Traditionally, this requires the use of carefully measured weights to see how much weight force moves the balance. The previous thrust balance was designed to measure vertical thrust forces, thus the process of adding weights was straightforward. The SPL thrust stand measures a horizontal thrust force, therefore calibration through the use of a

59
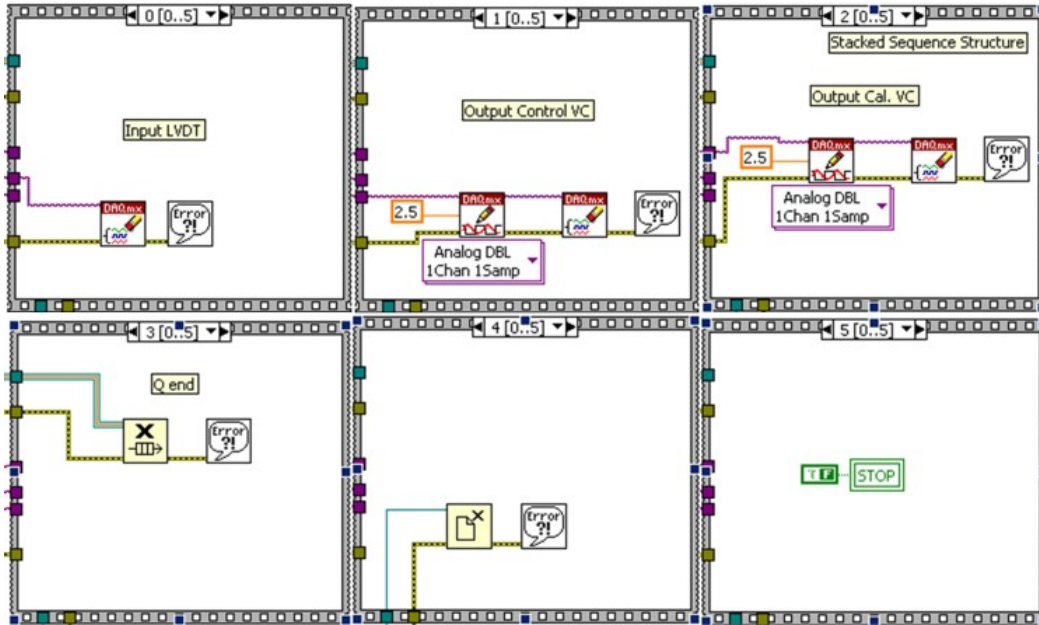
Figure 3.28: Final stacked sequence which terminates the program.

vertical weight force is a bit more complicated. The next subsection will explain the development of a weight dependent calibration system. The subsection following that will briefly mention the method of drift correction used inside the vacuum chamber.

3.5.1 External Calibration System

As mentioned in the previous paragraph, the most reliable force to calibrate is that of a known weight. This source is dependable because it can be considered a constant over time; the force of gravity will remain the same and the mass of a lead weight won't decrease or increase. This is unlike an electrically generated force from an electromagnet, which could change over brief intervals of time due to the small fluctuations in the current or voltage. Of course, the difficulty in utilizing a weight force is that it acts only in the vertical direction and the SPL thrust balance measures horizontal forces. To solve this problem, a pulley like system was created to turn the direction of the weight force. The picture in figure 3.29 shows the basic concept of how this was done.

In this sketch, the weights are attached to a very thin, light-weight wire or string. On the left side, the string wraps around a spool which is free to rotate. On the right
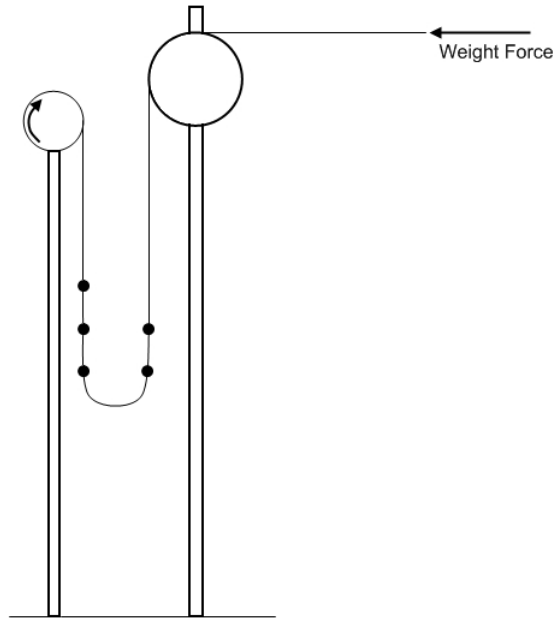
Figure 3.29: Sketch of the Calibration System for the SPL thrust balance.

hand side, the string bends around a cylindrical bar to turn the vertical weight force into a horizontal tension force. The weights hanging on the right side of the 180° wire loop contribute to this tension force, but the ones on the left side do not. This setup effectively changes the direction of the weight force so that it is useful to the thrust balance, but there are problems with this approach.

The most obvious problem is the friction force acting between the string and the roller on the right side of the setup. This force could be a significant source of error in the calibration. While it would be impossible to remove the friction entirely, the hope is that this force can be reduced as much as possible and characterized so that it is predictable. In order to diminish it as much as possible, Teflon was selected as the cylinder's material. It tends to have a very low static friction coefficient. This Teflon cylinder was fixed to the calibration stand arm, meaning it could not rotate.

Also of concern was the selection and method of attaching the weights themselves. The weights had to be on the order of milliNewtons and also had to be fixable to the string, unable to slide. The solution to this problem was a simple set of lead shot fishing weights. This type of fishing weight has a slot cut into it, and can be clamped onto a line using a set of pliers. Fishing weights also come in sizes small enough to
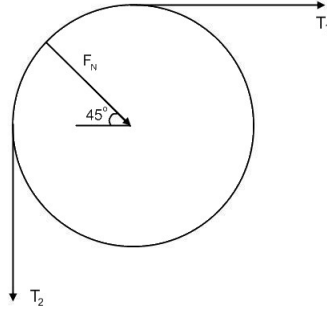
Figure 3.30: Normal force contributing to the friction.

produce the forces necessary for this calibration.

Finally, the right type of string had to be selected to connect all of these weights together. The ideal line should be as lightweight as possible and produce small amounts of friction when in contact with the Teflon cylinder. It is also important that the string be reasonably flexible, so that it can hang and produce the 180° loop separating the weights contributing force from the others. Trilene, XL 2 pound test fishing line was the ideal choice for this application. Since its tensile force limit was about two pounds, it had a very small diameter, just 0.13mm. This makes it lightweight and very flexible.

Because Teflon has such a small coefficient of friction, it shouldn't generate a large friction force when in contact with the fishing line. The best estimates of the coefficient of static friction between nylon (the material of most monofilament fishing lines) and Teflon indicate that it is about 0.1[19]. The force of friction between these two surfaces would be roughly linear to the normal force, as the basic frictional force equation shows.

$$F_f = \mu N \tag{3.25}$$

In this equation, F_f is the force of the static friction, μ is the coefficient of static friction, and N is the normal force. The normal force should be related to the tension in the fishing line. This tension is a combination of the weight of the fishing line and the fishing weights. The fishing line's weight was found to be negligible compared to

the fishing weights, and does not need to be considered. For problems like this one involving a string wrapped around a cylinder, the "capstan equation" can be used to find the static friction force[2].

$$T_2 = T_1 e^{\mu\theta} \tag{3.26}$$

As the picture in figure 3.30 shows, T_2 is the tension created by the hanging weights while T_1 is the tension force seen by the thrust balance. The terms in the exponential are the static friction coefficient (μ) and the angle in contact with the cylinder (θ). Knowing the coefficient of friction and the contact angle allows for the calculation of the actual force seen by the balance, T_1, for each hanging weight force, T_2. The difference between the two tensions provides the actual value of static friction.

$$F_f = T_2 - T_1 \tag{3.27}$$

Using a coefficient of friction of 0.1 and a contact angle of 90°, or $\frac{\pi}{2}$, the static friction turns out to be just less than 15% of the total hanging weight, much higher than desired. This could be the result of an inaccurate estimation of the coefficient of friction. To find a more accurate value of μ, a small experiment was setup in the lab as shown in figure 3.31. First, a laboratory scale was used to measure the weight of a fishing line with some weights attached. Then, a second measurement was taken with a mass of known weight (in this case, 26.37 grams) being pulled up off the scale under tension from the fishing line. The fishing line wraps around the Teflon cylinder by 180°, allowing the weight force to change direction. Subtracting the known weight from the second measurement should provide a value of the difference between the weight force on the line and the static friction force from the contact between the fishing line and Teflon. The difference between this number and the first measurement (which was the value of the weights on the fishing line) gives the static friction force, F_f. Since the tension force T_2 is known, T_1 is then found using equation 3.27. Knowing T_2 and T_1 along with the contact angle θ (which doubled to 180°, or π) allows the calculation of the coefficient of friction using equation 3.26.
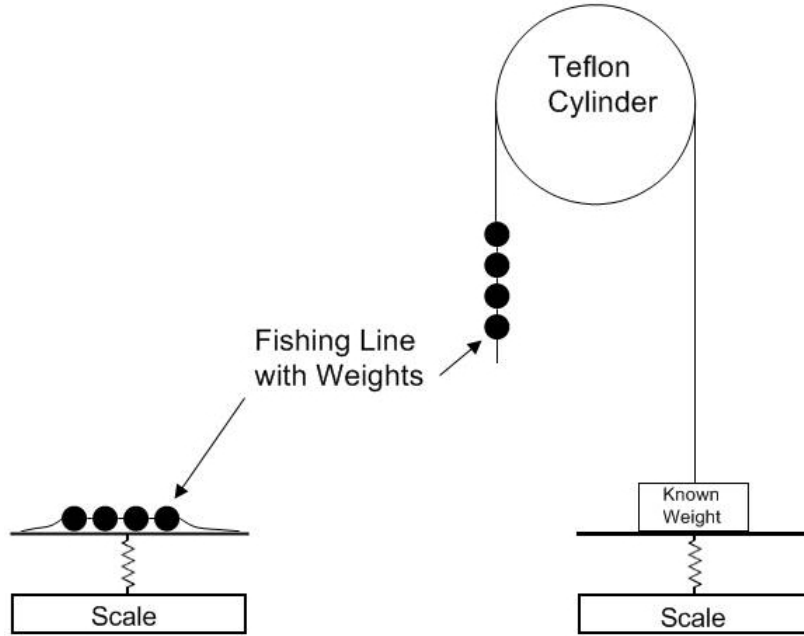
Figure 3.31: Experimental setup to determine the friction coefficient between Teflon and nylon fishing line.

Four different trials were done, and table 3.1 summarizes the results. The average coefficient of friction from the four trials turned out to be about 0.055, which means the friction force is actually closer to 8.3% of the total hanging weight, half of the theoretical prediction. So, when finding the calibration curve relating force to voice coil voltage, this 8.3% static friction should be subtracted from the total hanging weight to provide the true force seen by the thrust balance. For instance, when 10mN of weight is hanging on the calibration system, it is estimated that the response of the voice coil is to a force of around 8.3% less, or about 9.17mN.

Table 3.1: Results of the experiment to determine the friction coefficient between the Teflon cylinder and nylon monofilament fishing line.

String number	Amount of weight on string (g)	Known weight minus string tension (g)	$T_1(g)$	μ
1	1.217	25.255	1.116	0.0275
2	1.662	25.090	1.281	0.0828
3	2.000	24.730	2.781	0.0632
4	3.232	23.590	1.640	0.0478

64

Table 3.2: Values of the weights used in calibration.

Weight Num- ber	Weight Value (mN)	Total Hanging Weight (mN)	Resulting Static Friction (mN)	Actual Calibra- tion Force (mN)	Accuracy of the Cal- ibration Force (mN)
1	2.005	2.005	0.166	1.839	±0.077
2	0.956	2.961	0.245	2.716	±0.114
3	0.968	3.929	0.325	3.604	±0.151
4	1.011	4.940	0.409	4.531	±0.190
5	0.961	5.901	0.488	5.413	±0.227
6	0.990	6.891	0.570	6.321	±0.265
7	1.054	7.945	0.658	7.287	±0.306
8	0.980	8.925	0.739	8.186	±0.344
9	1.014	9.939	0.823	9.116	±0.383
10	0.999	10.938	0.905	10.033	±0.421
11	2.018	12.956	1.072	11.884	±0.499
12	1.917	14.873	1.231	13.642	±0.573
13	1.966	16.839	1.394	15.445	±0.648
14	1.976	18.815	1.557	17.258	±0.724
15	2.958	21.773	1.802	19.971	±0.838
16	3.019	24.792	2.052	22.740	±0.954
17	3.033	27.825	2.303	25.522	±1.071
18	3.024	30.849	2.553	28.296	±1.188

The construction and assembly of the calibration stand support arm was completed by MIT graduate student Ryan Daspit. The calibration system has one large aluminum arm to which the Teflon cylinder is fixed with a series of screws. A second small aluminum arm branches off of this main arm and supports a threaded rod. This rod holds a spool around which the fishing line, loaded with pre-determined weights, is wrapped. A total of 18 points of known weight are included on the line ranging between 2 and 32mN of force, and their values are given in sequential order in table 3.2. The weights were measured using an AdamLab AAA 250L scale with a resolution of 0.1 mg, or 0.00098mN. When the end of the fishing line is attached to the thrust balance, rotating the spool clockwise adds more calibration force while rotating counterclockwise reduces the calibration force.

There was one last issue with the integration of this calibration system and the
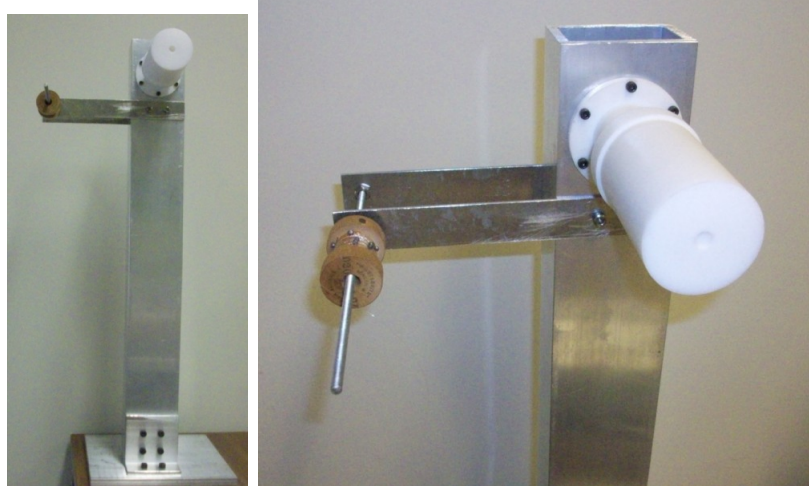
Figure 3.32: Pictures of the external calibration stand.

thrust balance. It is imperative that the fishing line be completely horizontal where it attaches to the balance. The initial thought was that the end of the fishing line could just be held in place underneath the weight of the thruster. Unfortunately, two problems arose when this technique was attempted. The thermal insulation layer that the thruster sits upon does not necessarily line up with the tangent to the top of the Teflon cylinder. Also, the fishing line is so thin that it can easily slip, even underneath the weight of the thruster. As a simple solution, the string is simply fixed to the back of the thruster (in a place which makes the line horizontal) with a piece of kapton tape. Pictures of the assembled calibration system can be found in figure 3.32.

3.5.2 Correction for Drifts During Use in the Chamber

As mentioned in previous subsections, the SPL thrust balance includes a secondary voice coil, placed adjacent to the LVDT. It is expected that the LVDT position reading will drift slightly between the time the external calibration is completed and the actual thrust measurement occurs. After the external calibration is finished, the chamber has to be sealed and pumped down to vacuum. The process of pumping the chamber down to vacuum and preparing the DCF can take almost a day, and over such a long period of time, it is likely that the equilibrium position of the balance will drift from
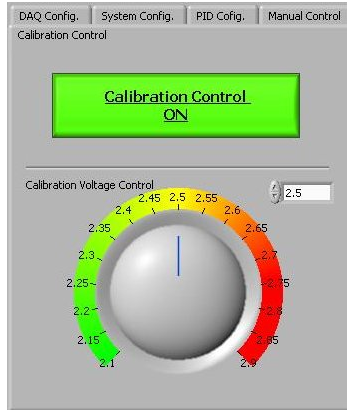
Figure 3.33: Calibration control tab in the Labview software which controls the second voice coil.

its calibrated location. The secondary voice coil, which is manually adjusted in the user interface of the control software, provides a way to force the balance's position back to the point where it was when calibration data was collected. It is believed that, so long as the drift is small, pushing the balance back to its starting location during calibration will ensure that the calibration curve is still valid. Figure 3.33 shows a screen shot of the drift correcting voice coil's user interface in the software.

As illustrated, the knob allows the user to change the force level being provided by the second voice coil. By watching the PID voltage value below this tab, the balance's position can be driven very close to its starting point during calibration. This process should be performed before thruster firings with the PID control on to ensure the stand is always at the same initial point prior to taking data. The full test procedure and the appropriate schedule for using the secondary voice coil for drift correction is outlined later in the paper.

3.6 Thermal Testing

The DCF can produce a significant amount of waste heat during operation. Since it is functioning in a vacuum environment, heat not radiated away or carried by the plume of the thruster will sink into the thrust balance through conduction. This could disastrously impact some of the precision pieces of the thrust stand and reduce accuracy because stiffness values change with temperature. For example, the waste

heat from the DCF could cause different parts of the flexible pivots to expand, altering their expected stiffness and possibly even damaging them. It was proposed that a layer of Teflon be placed between the top plate and the thruster to reduce the deleterious effects of the heat. In order to determine exactly how much Teflon should be used, theoretical calculations and experimental results were employed. First, this section will discuss the theoretical calculations, and then, the actual results from using a silicone heater with thermocouples.

3.6.1 Theoretical Modeling of the DCF's Heat Flow into the Thrust Balance

Before calculations can be performed, it is vital to know exactly how much heat needs to be dissipated from the thruster. According to the statistics from MIT graduate student Dan Courtney's thesis, the DCF had a peak efficiency of around 45% at an anode power of 242 watts [5]. With that power input and efficiency, about 130 watts will be given off by the DCF as waste heat. However, it may become necessary to measure thrust at higher power levels as well. In fact, it could be tested at power levels as high as 375 watts, where the expected efficiency would be about 35%[5]. At that efficiency and power, about 244 watts will need to be dissipated as waste heat, but only a fraction of this heat loss goes to the walls of the thruster. A considerable amount goes into the plume thermal energy and plasma radiation. The fraction of heat lost to the plume is not easily determined, therefore this analysis will assume the worst case scenario, in which all waste heat is delivered to the thruster's metal structure.

In the vacuum environment, there will be no convection to help remove some of this thermal energy. The only two means of heat transfer will be radiation and conduction. The radiation can be modeled using the Stefan-Boltzmann relation for radiation heat transfer[10].

$$q_{rad} = \epsilon A_s \sigma T^4 \tag{3.28}$$

In this equation, q_{rad} is the power in watts, ϵ is the emissivity of the skin of the material in question (unitless), A_s is the surface area in meters squared, σ is the Stefan-Boltzmann constant (in watts per meter squared per Kelvin to the fourth), and T is the surface temperature of the material in Kelvin. Assuming that the outer layer of the DCF is made of aluminum, the emissivity should be around 0.09 [10]. During a test firing of the DCF, a thermocouple was placed on the outer layer of the magnets (just inside the thruster's outer shell) and the temperature recorded was about $200°C$. To figure out how much heat is removed through radiation, the outer surface temperature of the DCF must first be calculated. Faraday's Law of Conduction can be used to find this outer surface temperature[10].

$$q_{cond} = \frac{kA}{L} \triangle T \qquad (3.29)$$

In this equation, q_{cond} is the power in watts, k is the thermal conductivity in watts per meter per Kelvin, A is the cross-sectional area of the material in meters squared, L is the thickness of the material in meters, and $\triangle T$ is the difference in temperature (in Kelvin) across the material. Because all of the outer shell pieces of the DCF are made from aluminum, the thermal conductivity is taken to be about $177\frac{W}{mK}$ [10]. It is assumed that the heat rate is very close to the waste heat value given earlier of 244 watts. To find the area and length of the material, the dimensions of the DCF casing, base core, and back plate must be known. These values can be estimated as shown in figure 3.34. For the purposes of modeling the heat flow, the assembled DCF casing, base core, and back plate can be redrawn as a composite wall in order to set up a thermal circuit and find the outer wall temperature. The composite wall representation and thermal circuit associated with it are shown in figure 3.35.

Each element has been transformed into a resistance. An additional thermal resistor was included for the point between the base core and back plate. This resistance is the result of the uneven surfaces of the base core and back plate on a microscopic level at the point of contact. A table of contact resistance is available in Incropera/DeWitt/Bergman/Lavine, and from this reference the contact resistance be-
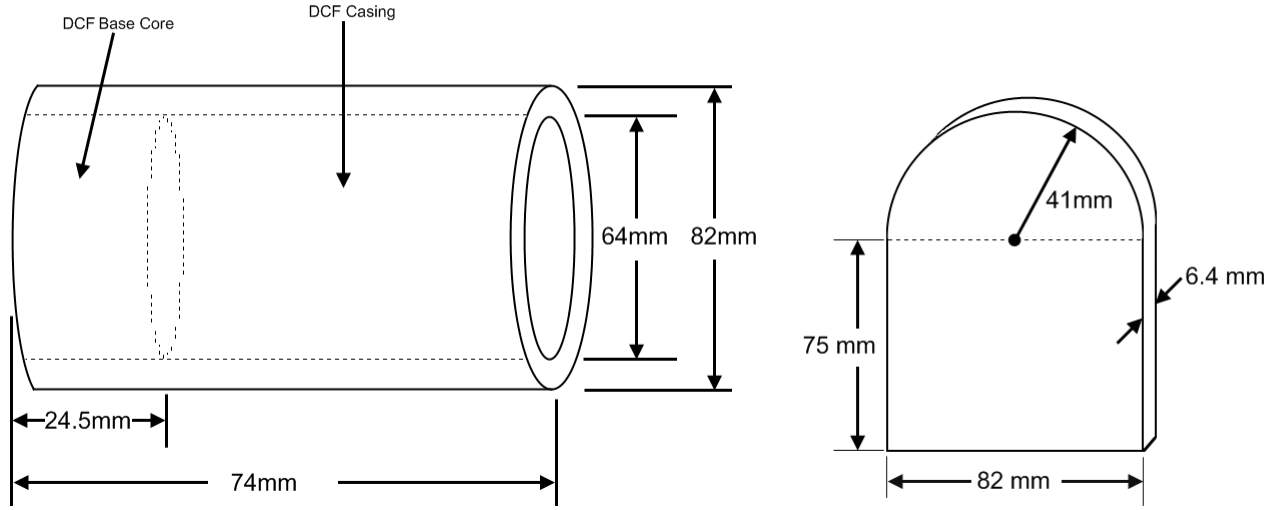
Figure 3.34: Rough dimensions of the DCF casing, base core, and back plate.

tween two surfaces of aluminum in a vacuum is known to be about $1.5 \times 10^{-4} \frac{m^2 W}{K}$ [10]. The resistance of the other elements is described by following equation:

$$R = \frac{L}{kA} \qquad (3.30)$$

In the equation above, L is the depth of the layer in meters, A is the surface area in meters squared, and k is the thermal conductivity. Once the total resistance is found, it is used to find the temperature change with the following formula:

$$q = \frac{\triangle T}{R} \qquad (3.31)$$

Here, R is the total resistance, q is the heat transfer rate through the DCF outer shell, and $\triangle T$ is the temperature drop. From the rough dimensions given above, each resistor in the circuit can be calculated as shown below.

$$R_{Casing} = \frac{L_{casing}}{k_{Al} A_{casing}} = \frac{0.018m}{177 \frac{W}{mK} \left(\pi \cdot 0.064m \cdot 0.0495m \right)} = 0.0102 \frac{K}{W}$$
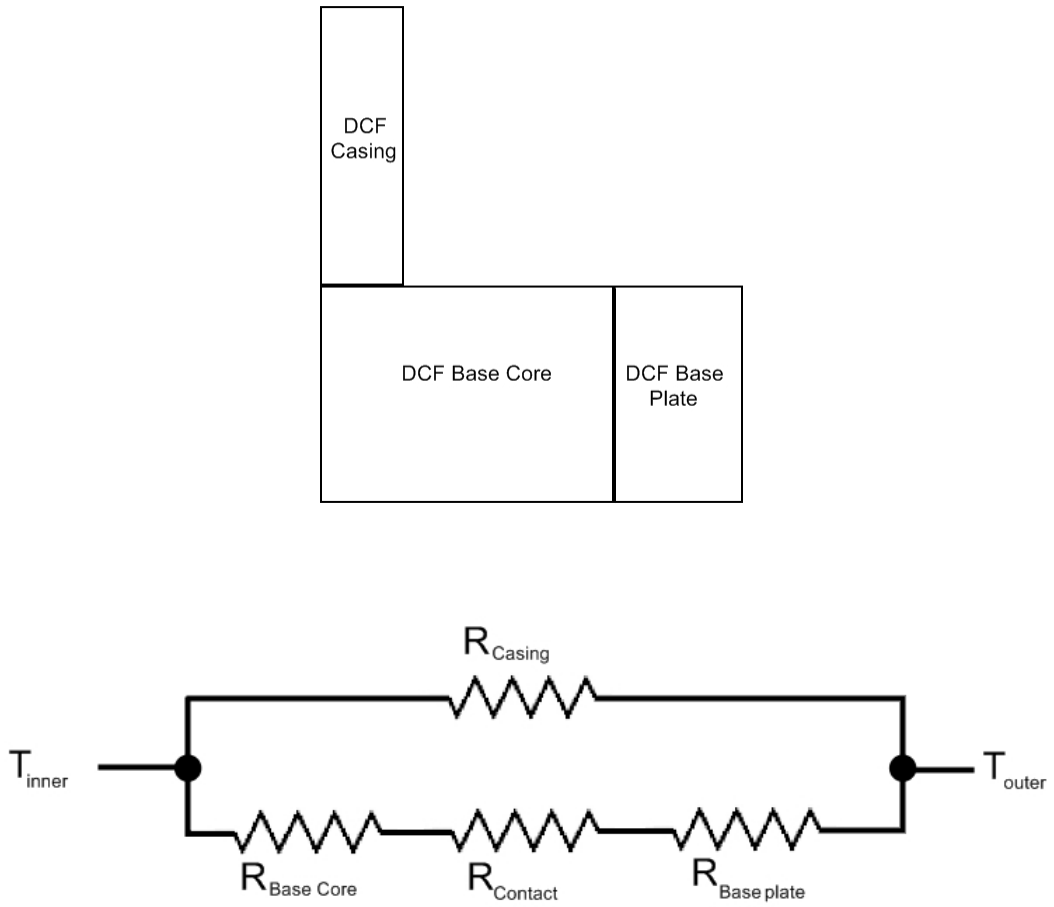
Figure 3.35: One dimensional composite wall and corresponding thermal circuit representing the path of the heat flow through the DCF.

$$R_{Core} = \frac{L_{Core}}{k_{Al}A_{Core}} = \frac{0.0245m}{177\frac{W}{mK}\left(\frac{\pi}{4}(0.064m)^2\right)} = 0.0430\frac{K}{W}$$

$$R_{Plate} = \frac{L_{Plate}}{k_{Al}A_{Plate}} = \frac{0.0064m}{177\frac{W}{mK}\left(0.075m \cdot 0.082m + \frac{1}{2}\pi(0.041m)^2\right)} = 0.00411\frac{K}{W}$$

$$R_{contact} = \frac{R"_{contact}}{A} = \frac{1.5 \times 10^{-4}\frac{m^2K}{W}}{\frac{\pi}{4}(0.064m)^2} = 0.0466\frac{K}{W}$$

With these resistance values known, they can now be combined just as they would be in an electrical circuit. The plate, core, and contact resistors can be combined in series by adding their values together. Then, this equivalent resistance can be combined in parallel with the resistance from the DCF casing using the equation for parallel resistors.

$$\frac{1}{R_{eq}} = \Sigma\frac{1}{R_i} \tag{3.32}$$

Combining the resistors produces a total resistance of about $0.009214\frac{K}{W}$. Plugging this value along with the total heat rate (244 watts) into equation 3.31 from above shows that the temperature will only drop about $3°C$. This puts the surface temperature of the DCF at about $197°C$. Of course, this assumes that the aluminum surface is at a uniform temperature, and also that little (if any) heat dissipation occurs within the aluminum, and that all 244 watts of heat make it through the casing. Without thermocouple data on the surfaces of the DCF, more accurate values would be hard to obtain. Knowing the Stefan-Boltzmann constant to be $5.67 \times 10^{-8}\frac{W}{m^2K^4}$ means that all of the necessary values are now in place to find the radiation heat losses.

Using equation 3.28 from the beginning of this section, with the emissivity of aluminum ($\epsilon = 0.09$) and surface area of the DCF casing and the back plate (minus the surface where the casing touches the plate, this area is about $0.0296m^2$), the total
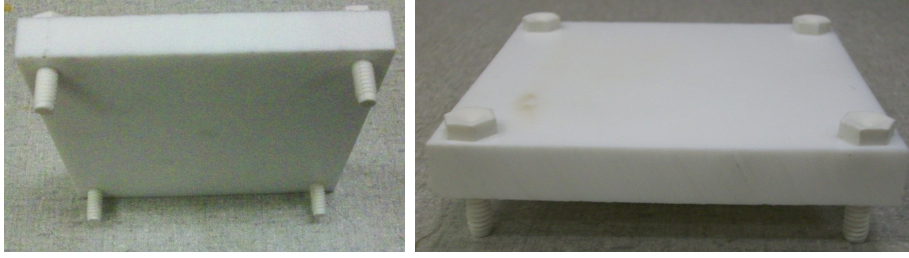
Figure 3.36: The Teflon insulation used to separate the DCF from the thrust stand.

loss from radiation becomes:

$$q_{rad} = \epsilon A_s \sigma T^4 = (0.09)\left(0.0296 m^2\right)\left(5.67 \times 10^{-8} \frac{W}{m^2 K^4}\right)(197^o C + 273K)^4 = 7.37W$$

Therefore, very little of the heat is dissipated through radiation. That still leaves about 236.6 watts going into the the thrust balance through conduction. To prevent the thrust measurements from drifting while the thruster is in operation, as much of this heat should be blocked from the thrust balance as possible. Knowing the thermal conductivity of Teflon to be $0.23\frac{W}{mK}$, it was chosen as the appropriate material for the thermal barrier.

Rather than using a block of Teflon, an alternative design was considered. This involved using a slab of Teflon mounted on four Teflon pegs, reducing the contact surface area and increasing the thermal resistance significantly. A piece of half inch Teflon was used as the base, and the pegs were made from Teflon screws. Figure 3.36 shows this new design configuration.

To determine the heat rate that can penetrate this insulating layer, the idea of thermal resistance should be revisited. Treating the Teflon plate and pegs as two different thermal resistors in series allows for the calculation of a total heat resistance. The length of the pegs is about 12 millimeters and each has a diameter of about 6 millimeters. Now, the total resistance becomes:

$$\Sigma R = \frac{L_{plate}}{k_{plate} A_{plate}} + \frac{L_{pegs}}{k_{pegs} A_{pegs}} = \frac{0.0127m}{\left(0.23\frac{W}{mK}\right)(0.01032m^2)} + \frac{0.012m}{\left(0.23\frac{W}{mK}\right)4\left(\frac{\pi}{4}(0.006m)^2\right)} = 466.7\frac{K}{W}$$

With this thermal resistance and a temperature drop of about $150^\circ C$ (found

73
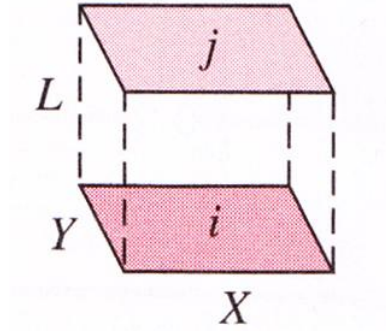
Figure 3.37: View factor geometry for the radiation heat transfer problem.

through testing as shown in table 3.6), the rate of heat transfer making it through the Teflon by conduction becomes just 0.321 watts, well below the limit.

Left to consider is the radiation heat transfer between the bottom of the Teflon base and the top of the thrust balance plate. Teflon has a much higher emissivity than aluminum, about 0.38[10]. Since most of the thermal resistance occurs in the pegs (due to their small cross-sectional area), the bottom of the Teflon base can become very hot. In fact, it should be pretty close to the temperature of the DCF base plate:

$$T_f = T_i - \frac{Lq}{kA} = 197^oC - \frac{0.0127m \cdot 0.315Watts}{\left(0.23\frac{W}{mK}\right)(0.01032m^2)} \approx 196.3^oC$$

Heat transfer by radiation should occur between the lower surface of the Teflon base plate, the thrust balance top plate, and the surroundings. To determine how much heat transfer occurs between each surface, the view factor must be calculated [10]. For two rectangular parallel plates of length X and width Y, separated by a distance L, the equation for calculating the view factor is as follows:

$$\bar{X} = \frac{X}{L} \tag{3.33}$$

$$\bar{Y} = \frac{Y}{L} \tag{3.34}$$

74
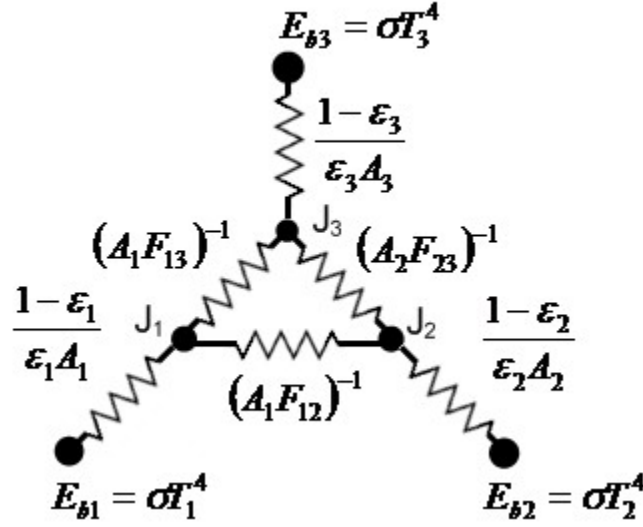
Figure 3.38: Thermal circuit to calculate the radiation heat transfer between the Teflon base, thrust balance top plate, and the surroundings.

$$
\begin{aligned}
F_{ij} &= \frac{2}{\pi \bar{X}\bar{Y}} \ln \left\{ \left[\frac{\left(1 + \bar{X}^2\right)\left(1 + \bar{Y}^2\right)}{1 + \bar{X}^2 + \bar{Y}^2} \right] + \bar{X}\left(1 + \bar{Y}^2\right)^{1/2} \tan^{-1}\left(\frac{\bar{X}}{\left(1 + \bar{Y}^2\right)^{1/2}} \right) \right\} \\
&\quad + \frac{2}{\pi \bar{X}\bar{Y}} \ln \left\{ \bar{Y}\left(1 + \bar{X}^2\right)^{1/2} \tan^{-1}\left(\frac{\bar{Y}}{\left(1 + \bar{X}^2\right)^{1/2}} \right) - \bar{X}\tan^{-1}\left(\bar{X}\right) - \bar{Y}\tan^{-1}\left(\bar{Y}\right) \right\}
\end{aligned}
$$

(3.35)

With a length and width of 4 inches for both the Teflon and thrust balance top plate, and a separation distance of 12 mm, the view factors F_{12} and F_{21} are both 0.8. The view factors between the surfaces and the surroundings, F_{13} and F_{31} are therefore 0.2 each. A thermal circuit can be setup to help solve the problem in a similar manner as before (see figure 3.38). In the diagram of figure 3.38, the nodes J_1, J_2, and J_3 represent the radiosity of each surface. The radiosity is the combination of the radiation emitted and reflected [10]. The inner resistors are the result of the view factor ratios, while the outer resistors are the result of radiosity. Assuming that the surroundings will act almost like a black body, the values for the variables in the resistor circuit can be found in table 3.3. Looking at nodes one and two produces a series of two equations and two unknowns, J_1 and J_2.

Table 3.3: Properties for the three surfaces in the radiosity circuit.

Property	Surface 1	Surface 2	Surface 3
T (K)	469.3	323	288
ϵ	0.38	0.09	1
A (m^2)	0.01032	0.01032	-
$E_b\left(\frac{W}{m^2}\right)$	2755	617.2	390

$$\frac{\sigma T_1^4 - J_1}{(1 - \epsilon_1)/\epsilon_1 A_1} = \frac{J_1 - J_2}{1/A_1 F_{12}} + \frac{J_1 - \sigma T_3^4}{1/A_1 F_{13}} \tag{3.36}$$

$$\frac{\sigma T_2^4 - J_2}{(1 - \epsilon_2)/\epsilon_2 A_2} = \frac{J_2 - J_1}{1/A_1 F_{12}} + \frac{J_2 - \sigma T_3^4}{1/A_2 F_{23}} \tag{3.37}$$

Solving the two equations for the unknown J_2 shows it has a value of 1344. Plugging this into the equation below allows for the solution of the radiation heat transfer to the aluminum plate.

$$q = \frac{\sigma T_2^4 - J_2}{(1 - \epsilon_2)/\epsilon_2 A_2} \tag{3.38}$$

The equation shows that the radiation heat transfer will be approximately 0.75 watts, more than 2 times the amount that is transferred by conduction. The radiation heat transfer between the Teflon insulation and the thrust balance is small, but not insignificant. To diminish this undesired heat transfer, it was proposed that a couple pieces of aluminum foil be placed in the space between the Teflon base and thrust balance top plate, as shown in figure 3.39. With an emissivity as low as 0.03, it should be able to help reflect most of this radiation[10].

3.6.2 Thermal Testing of Insulation Materials

An experiment was performed to check the validity of these theoretical results. The test was done using a replica of the DCF base plate and back plate. The dimensions of the mock DCF plates were similar to those of the real ones. Two heaters were attached to the back plate for the experiment. These were silicone heaters, each about 3 inches in diameter. Table 3.4 provides the power capabilities of the heater
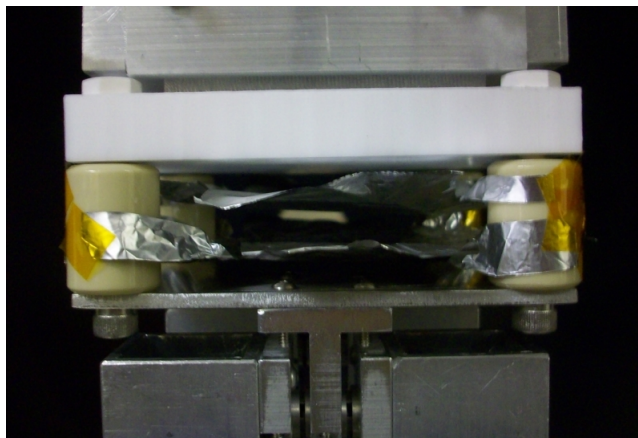
Figure 3.39: Aluminum foil layer added between the Teflon insulation and thrust balance top plate.

Table 3.4: Information about the heaters used in the thermal testing.

Heater Type	Flexible Silicone-Rubber Heater Plain Backing
Sheet Dimensions	Round, 3" in diameter
Thickness	0.035"-0.07"
Watts/sq in	10
Total Watts	71
Maximum Voltage	115 VAC
Amps	0.62A
Temperature Exposure Range	-70ºC to 450ºC

model chosen along with some other characteristics.

The heaters required an alternating current input, and only one AC power supply was available in the lab, thus the two heaters were connected in parallel to produce the highest power levels possible. When connected in parallel, the equivalent resistance became 92.5Ω, drawing a maximum current of 1.23A at the highest recommended voltage of 115V. This meant the total power flowing to the heaters was around 142 Watts, about 100 watts shy of what the DCF produces. Rather than attempt to pump the full 237 watts of heat through the insulation, several lower power levels were tested in an attempt to make a linear relationship between input power and heat dissipation by the thermal boundary. It should be noted that the experiment was performed without the radiation blocking layer of aluminum foil, therefore the heat rate reaching the thrust balance was a combination of conduction and radiation
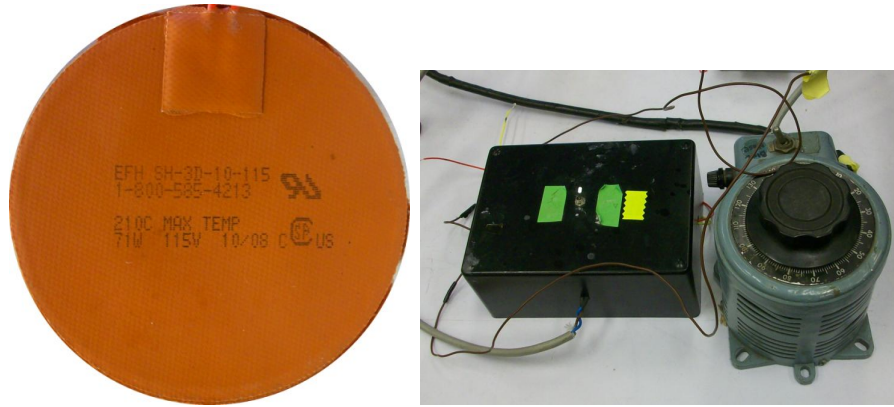
Figure 3.40: One of the two circular silicone heaters used in the thermal testing (left) and the power supply system used to power the heaters (right).

Table 3.5: Data on the thermocouples used during the thermal testing.

Thermocouple Model	CO Series
Style	CO1-K
Type	K
Measurement	Surface Temperature
Response Time	milliseconds
Length	1m (40")
Maximum Continuous Temp.	260^oC (500^oF)

heat transfer. A picture of the heaters and the power supply system used in the thermal test can be found in figure 3.40.

The heaters were attached to the replica back plate using Dow Corning 736 heat sealant. This is a special adhesive which can handle exposures to temperatures on the order of $260°C$ continuously without weakening or sagging. Type K thermocouples were used to measure the temperature on the mock plates and on the layer of Teflon insulation. Some characteristics of these thermocouples are found in table 3.5. Before the experiment was performed, the cold junction temperature of each thermocouple was found using the ice bath technique. This cold junction temperature is the amount of error observed in the measurement of a known reference temperature. In the case of the ice bath, the reference temperature is meant to be $0°C$. To provide a reference point as close to zero as possible, the ice bath consisted primarily of crushed ice with a very small amount of water added [8].

In order to read the voltage from the thermocouples, translate it into a tempera-
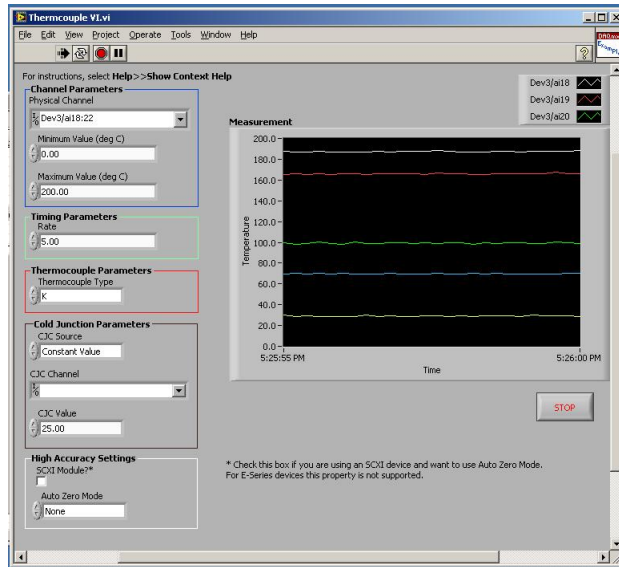
Figure 3.41: Labview VI used to read and record the temperature data from the thermal test.

ture, and save the data, a thermocouple measuring Labview program was employed. The user interface of the program is shown in figure 3.41. It enabled the user to input the channels on the DAQ card where the thermocouples were attached, as well as, an estimate of each cold junction temperature and thermocouple type. While running, the program outputs the temperature results to a graph for the user to see. In addition, this temperature data was compiled in a text file.

A total of five thermocouples were available, and these were placed on the replica back plate next to the heater, under the replica base plate, on the bottom of the Teflon base plate (one centered and another near one of the four pegs), and on the top of the thrust balance's top plate. The pictures in figure 3.42 illustrate this thermocouple placement.

The thermal data were collected in a series of five stages, each corresponding to a different input power. The voltage started at zero and was increased to 40 volts during the first stage, corresponding to a power input of about 17.3 Watts. The system was allowed to sit while all of the layers reached a steady state temperature. After this was achieved, the voltage was increased. Table 3.6 shows the five different trials and the corresponding power levels, along with the steady state temperature of
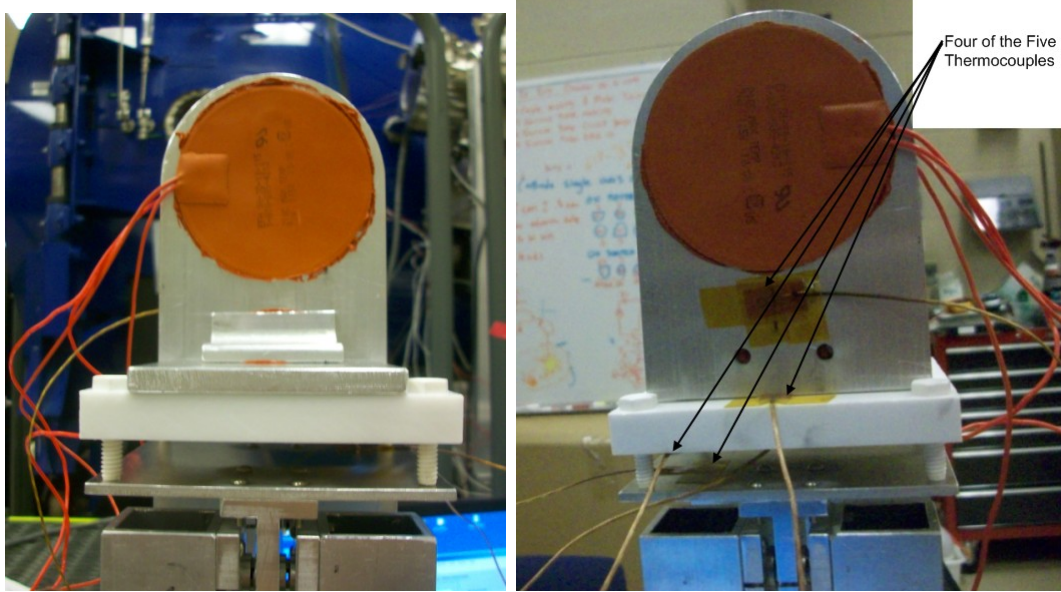
Figure 3.42: Picture of the thermocouples and heaters as they were attached to the mock DCF back plate, base plate, and Teflon.

each thermocouple. To see the full set of temperature measurements collected during the transient part of the experiment, see Appendix B.

At the highest power level, the Teflon insulation produced a significant temperature drop. Knowing the thermal resistance of the insulation allows for the calculation of the heat transfer penetrating this layer and reaching the thrust balance top plate. This is shown below.

$$q_{Teflonlayer} = \frac{\triangle T}{R} = \frac{(208°C - 30°C)}{466.7\frac{K}{W}} = 0.381W$$

Because this test was performed in a pressurized environment, convection heat transfer losses must be accounted for as well. To find the heat rate lost through convection, the Nusselt Number must be found in order to estimate the heat transfer coefficient[10]. To find the Nusselt Number, the Rayleigh Number is needed, and this value can be found through the following equation [10]:

$$Ra_L = \frac{g\beta(T_s - T_\infty)L^3}{\nu\alpha} \tag{3.39}$$

In this equation, g is the acceleration due to gravity (in $\frac{m}{s^2}$), β is the volumetric

Table 3.6: Results of the thermal testing.

	Stage 1	Stage 2	Stage 3	Stage 4	Stage 5
Voltage	40V	60V	80V	100V	110V
Current	0.432A	0.649A	0.865A	1.08A	1.19A
Power	17.3W	38.9W	69.2W	108W	130W
Back Plate (below heaters) S.S. Temp.	61^oC	98^oC	146^oC	191^oC	208^oC
Back Plate (surface touching Teflon) S.S. Temp.	56^oC	89^oC	135^oC	173^oC	188^oC
Under Teflon Plate (next to peg) S.S. Temp.	31^oC	42^oC	61^oC	74^oC	77^oC
Under Teflon Plate (middle) S.S. Temp.	41^oC	60^oC	86^oC	106^oC	109^oC
Top Plate of Thrust Balance S.S. Temp.	24^oC	25^oC	28^oC	30^oC	30^oC

thermal expansion coefficient (in K^{-1}), $T_s$is the surface temperature of the object, $T_\infty$is the ambient temperature, L is the characteristic length (in meters), ν is the dynamic viscosity (in $\frac{m^2}{s}$), and $\alpha$is the diffusivity (in $\frac{m^2}{s}$). Once the Rayleigh Number is found, it can be used to calculate the Nusselt Number with the following equation[10]:

$$\overline{Nu}_L = 0.68 + \frac{0.670Ra_L^{1/4}}{\left[1 + (0.492/Pr)^{9/16}\right]^{4/9}} \tag{3.40}$$

The variable Pr in the denominator is the Prandtl Number. Finally, from the Nusselt Number, the convection heat transfer coefficient can be calculated with the equation below[10]:

$$h = \frac{k}{L}\overline{Nu}_L \tag{3.41}$$

The k in this formula is just the thermal conductivity for air and L is the characteristic length again. For air at temperatures around 25 degrees Celsius, these values tend to be: $\nu = 16.2 \times 10^{-6}\frac{m^2}{s}$, $\alpha = 22.9 \times 10^{-6}\frac{m^2}{s}$, $\beta = 0.0033K^{-1}$, $k = 0.0265\frac{W}{mK}$, and $Pr = 0.71$[10]. Convection should be occurring from each exposed surface of the back plate and base plate. First, the back plate will be analyzed, and then, the base

plate. The back plate is approximately 200 degrees Celsius on average during the 130 watt test, and the characteristic length of both the front and back faces, as well as, the sides, is about 5 inches, or 0.127 meters. The area of the front face, back face, and sides combined is approximately 0.0228 meters squared. With this characteristic length and average surface temperature, the Rayleigh Number is approximately 32,677,720 leading to a Nusselt Number of about 39.56 and a heat transfer coefficient of $8.25 \frac{W}{m^2 K}$. The exposed sides of the base plate have a characteristic length equal to their height, about a quarter inch, or 0.00635 meters. Their temperature probably turns out to be a little less than the back plate, so it can be approximated as 150 degrees Celsius. The total area of the sides turns out to be 0.00210 meters squared. With this characteristic length, average surface temperature, and surface area, the Rayleigh Number is approximately 2790 with a Nusselt Number of about 4.41 and a heat transfer coefficient of $18.404 \frac{W}{m^2 K}$. The top surface of the base plate can also be assumed to be about 150 degrees Celsius, with a characteristic length of 0.0205 meters (found by dividing the surface area by the perimeter), and a surface area of 0.00677 meters squared. These values provide a Rayleigh Number of about 94089 which leads to a Nusselt Number of 9.687 and a heat transfer coefficient of $12.504 \frac{W}{m^2 K}$.

Convection will also be experienced on the Teflon insulation plate. With an overall temperature averaging 90 degrees centigrade and a characteristic length of 0.0127m for the sides and 0.0254m for the bottom face, the Rayleigh Number for the sides and bottom should be 11,607 and 92,855, respectively. These lead to Nusselt Numbers of 6.47 and 10.41, with heat transfer coefficients of $13.5 \frac{W}{m^2 K}$ and $10.86 \frac{W}{m^2 K}$. Now, the convection heat transfer equation can be utilized to find the total number of watts lost to convection. The convection heat transfer equation, also known as Newton's Law of Cooling, is given below[10]:

$$q = hA\left(T_s - T_\infty\right) \tag{3.42}$$

Calculating the convection from each surface gives the total:

Table 3.7: Calculation of the various forms of heat transfer involved in the thermal testing.

	Trial 1	Trial 2	Trial 3	Trial 4	Trial 5
Power Input (W)	17.3	38.9	69.2	108	130
Convection Loss (W)	7.6	18.6	35.1	50.5	59.4
Net Power (minus Convection) (W)	9.7	20.7	34.1	57.5	70.6
Conduction and Radiation heat transfer penetrating the Teflon Insulation (W)	0.0686	0.137	0.229	0.306	0.339

$$q_{conv} = h_1 A_1 \triangle T_1 + h_2 A_2 \triangle T_2 + h_3 A_3 \triangle T_3 + h_4 A_4 \triangle T_4 + h_5 A_5 \triangle T_5 = 60W$$

Taking the convection losses and subtracting them from the 130 watts of power input during the fifth trial means that the Teflon boundary needed to dissipate a total of 70 watts. The insulation was successful in blocking all but 0.381 watts of this heat. The goal is to take the results from each trial and try to produce a linear relationship between the input power and the heat rate that penetrates the thermal boundary. The results should show if the design will hold up against the anticipated 237 watts expected in the actual testing. Table 3.7 shows the input power, the convection losses, the net power (input minus convection), and heat transfer penetrating the thermal insulation. A plot of the conduction and radiation heat transfer that penetrates the insulation versus the power input (minus convection losses) was created. This plot is shown in figure 3.43. A linear fit line was applied to the plot for the purposes of estimating the losses at higher power levels.

The heat rate through the Teflon appears linear, with approximately 0.0044 watts reaching the thrust balance top plate per watt of input power. Using the linear fit, under a 237 watt load the number of watts reaching the thrust balance should be approximately 1.09. This comes very close to the prediction of the theoretical calculations, which estimated that a heat rate of 0.315 watts would make it through
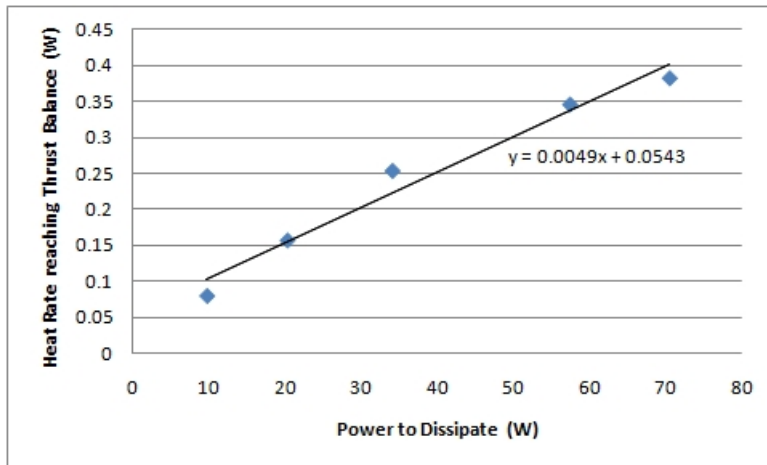
Figure 3.43: Heat Rate through the Teflon insulation versus the input power.

by conduction and 0.75 watts would reach the balance through radiation, for a total of 1.07 watts. This reinforces the value found through the theoretical thermal resistance model. With as much as 237 watts of waste heat, the temperature of the thrust balance should not increase by more than 10 degrees Celsius, even without any aluminum foil radiation heat transfer barrier.

4 Thrust Balance Operational Procedure and Results

Now that the design and construction of the thrust balance have been discussed at length, it is an appropriate time to look at the operational procedure and the preliminary results attained when using the balance with the DCF. First, an in-depth set of instructions to prepare the thrust balance and its various components for use will be explained. Then, a calibration and testing procedure will be outlined, along with the uncertainty associated with these measurments. Finally, this section will display the initial results achieved when using the thrust balance to take measurements with the DCF.

4.1 Setup, Calibration, and Test Procedure for Operating the DCF's Thrust Balance

The following subsection explains the process of using the balance to take thrust measurements. First, a list of all the required parts is given, along with the procedure to set up each of these components for testing. Afterwards, an in-depth diagnostic is provided to ensure the sensors, actuators, and control hardware are working properly. This is followed by a step-by-step procedure to setup the Labview software and to calibrate the stand. Finally, this section provides an explanation of the proper way to take measurements while the DCF is in operation.

4.1.1 Required Components

Before the thrust balance can undergo testing, all of the essential parts must be gathered. The following components are required to successfully take thrust measurements:

1. Inverted-pendulum thrust balance

2. Vacuum safe, shielded, 9 pin cable

3. Vacuum chamber 9 pin through port

4. Triple shielded, beige, 9 pin cable

5. DCF control box

6. USB cable

7. SPL Lab desktop computer with Labview and thrust balance software installed (or laptop computer with executable version of the software installed)

8. External calibration stand

9. External calibration spool with string of pre-measured weights

4.1.2 Setting up the connections between the balance, control box, and computer

Once these essential parts have been gathered, they should be assembled as shown in figure 4.1.
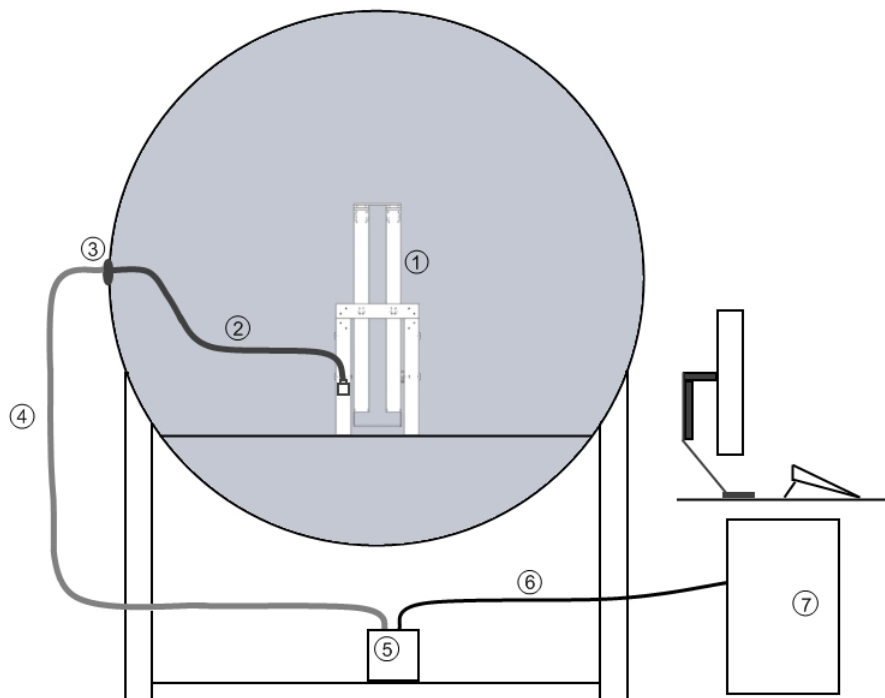
Figure 4.1: Experimental setup of the DCF thrust balance. The components are labeled according to the list in the previous section. The balance itself is sitting in the vacuum chamber in this figure.

1. The thrust balance sits within the chamber. Before the balance goes into the vacuum chamber, it must be thoroughly cleaned to prevent significant outgassing when the chamber is put under low pressure. The thruster should sit on the Teflon thermal boundary, which is permanently attached to the top plate of the thrust balance. Use a screw to fix the thruster to the hole in the Teflon base. The thrust balance should be placed in the chamber on a flat, level surface. Before securing the thruster to the balance, be sure to measure the weight of the thruster and cathode so that the appropriate amount of counterweight can be added to the bottom plate. Due to the limited amount of space, lead weights are the best material to use as a counterweight. The amount of counterweight needed will be:

   Counterweight Moment Arm × Weight of Counterweight =

   Thruster Moment Arm × (Weight of Thruster + Weight of Cathode

   +Weight of Thermal Layer)

   The thermal insulation weighs about 0.282 kilograms, while the weight of the thruster and cathode can vary. The counterweight should be positioned on the bottom plate and adjusted to ensure that the stand appears as neutrally balanced as possible. The stand will be neutrally balanced when the pendulum is hanging freely and not leaning to one side. Place the external calibration arm on the edge of the grate at the entrance of the chamber. The calibration stand should be at a spot which allows its calibration string to hang out of the chamber and as low as the lab floor. Attach the string on the spool to the thruster such that none of the weights contribute a force. For the time being, the chamber should be left open.

2. The vacuum ready shielded cable runs from the 9 pin connector on the thrust balance to a 9 pin through port on the vacuum chamber. It may be necessary

to attach this cable to the 9 pin through port and feed it into the chamber before the through port is connected, due to the narrow space available in some of ASTROVAC's ports. To save troubleshooting time later, it would be best to test each of the pins and verify that they are working after installation. Note that the pins "flip" at the through port, i.e. pin 1 on the through port should be pin 5 at the end of the shielded vacuum cable, and pin 9 on the through port will be pin 6 at the end of the shielded vacuum cable. See Appendix E for a more thorough explanation of the flip seen on either end of the through port.

3. The beige 9 pin computer cable should be connected to the external part of the 9 pin through port. It runs underneath the vacuum chamber and connects to the 9 pin port on the control box. During the initial setup, this cable should be left unplugged from the control box. The next subsection will explain when this should be attached.

4. The control box is placed on the platform underneath the vacuum chamber to ensure the cables running to and from it are able to reach. The switch on the control box should be in the off position. An ordinary desktop computer power cord should run between the control box and a basic AC power outlet.

5. An ordinary USB cable should run between the desktop computer in the lab and the control box. For the time being, this cable should also be left unplugged. The diagnostic section will explain when this USB line should be attached.

6. The desktop computer in the lab should have the base version of Labview from 2009 or later in order to run the control software. The computer should also have the control software program itself. To confirm the software is on the computer, click the start button, then search, and files and folders. Search for the VI file called "MIT-SPL Thrust Balance-5-1".

4.1.3 Diagnostic testing of the control box, LVDT, and voice coils

Once the necessary components have been connected, the next step is to run a diagnostic check to verify that the control box, LVDT, and voice coils are all working properly. The following steps should be taken to ensure that these parts are operating correctly:

1. Connect the control box's DAQ card by plugging the USB cable into the control box and computer. Do NOT turn on the control box or connect the 9 pin cable yet.

2. Open the "Measurements & Automation Explorer" by double clicking its icon on the desktop of the computer.

3. Under the toolbar on the left, expand the plus sign next to "Devices and Interfaces" and perform the following actions:

   - Expand the plus sign "NI-DAQmx Devices".

   - Select USB 6009 Dev 3 (if the computer sees the DAQ card, it will be in green) and click on the button that says "test panel". The window shown in figure 4.2 should appear.

4. While keeping the control box switch in the off direction and with no connection to the thrust balance (9 pin connector unplugged):

   - Select the Analog Output Tab, set the channel to "ao0", and set the voltage to 2.5V. Click the update button.

   - Go back to the Analog Input tab and set the following:

     - Channel Name: ai2
     - Mode: continuous
     - Rate: 1,000 Hz
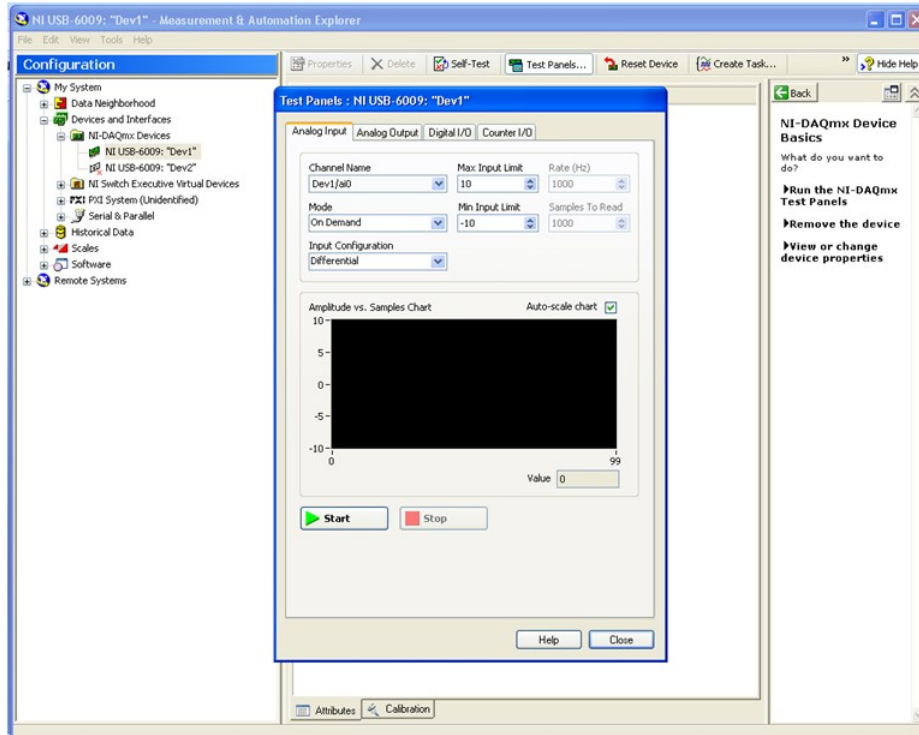
Figure 4.2: Test Panel for the USB 6009 DAQ card.

- Click the button that says "start" and verify that the DAQ card is sending a 2.5V signal as shown in figure 4.3 (a small 60Hz oscillation may be present, but it will have a small voltage). Repeat by setting the voltage to 0V and 5V. This confirms that the DAQ card is working properly.

5. Now that the DAQ card is functioning as expected, the amplifying circuits will be tested. First, go to the analog output tab.

- Go to channel "ao0", adjust the voltage to 2.5V and click update. Go to channel "ao1", adjust the voltage to 2.5V, and click update.

6. Next, connect the 9 pin cable to the box and turn on the power to the control box by flipping the switch to the on position. Perform the following actions:

- On the analog input tab, hit the stop button and change the channel name to "ai1". This channel monitors the voltage coming out of the first amplifying circuit. Proceed by clicking start.

90
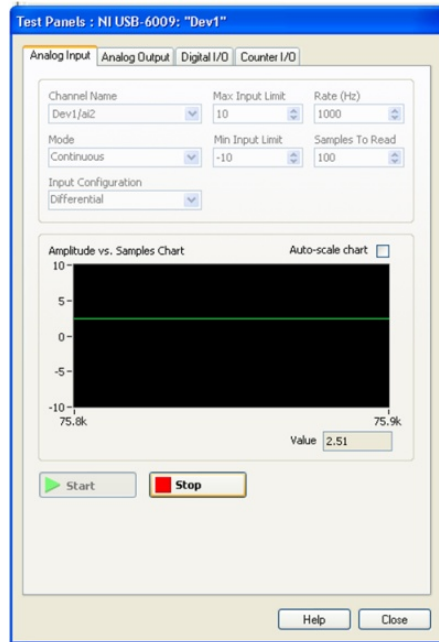
Figure 4.3: Analog input tab displaying the output of the DAQ card.

- Go to the analog output tab. Make sure to select channel "ao0". Set the voltage to 5.0V and click update.

- Go back to the analog input tab and verify that the voltage is no longer 0V. It should be about 0.7V or 0.8V.

- Return to the analog output tab and set the voltage to 0 and click update.

- Select the analog input tab and verify that the voltage is now around -0.7V to -0.8V.

- Go back to the analog output tab and set the voltage back to 2.5V.

- If the readings from the analog input tab are correct, there is confirmation that the first amplifying circuit and voice coil are functioning appropriately. Repeat these steps for the output channel "ao1" and input channel "ai3" to verify that the second amplifying circuit and voice coil are also working properly.

7. To verify the LVDT is running properly, the following actions should be taken:

- On the analog input tab, set the channel name to "ai0" and click start.
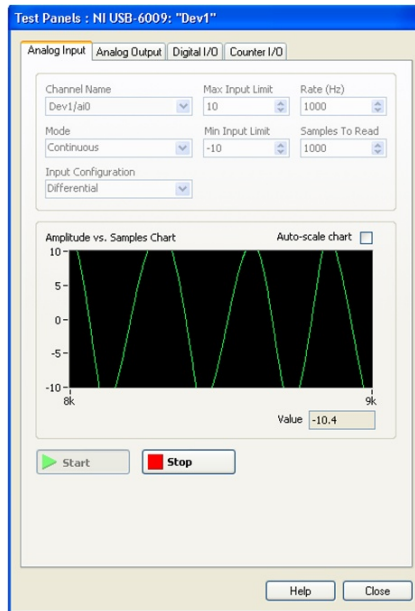
Figure 4.4: Analog input tab displaying the signal coming from the LVDT.

This channel monitors the voltage signal coming from the LVDT.

- Tap the balance very lightly so that it oscillates. The LVDT signal should fluctuate on the plot as shown in figure 4.4.

- When the balance is settled, the LVDT should be reading as close to 0V as possible (the neutral balance reading). If the LVDT's signal is not close to 0V when the balance is still, loosen the screw that holds the LVDT in place and adjust it manually.

8. The diagnostic steps are now complete and the control box, LVDT, and both voice coils should be operating correctly. Close the Measurement & Automation Explorer.

4.1.4 Setting up the Labview Software

Now that the LVDT, control box, and voice coils have been tested, the next step is to set up the Labview program for calibration. The following steps should be taken after the diagnostic procedure, but before the external calibration:

1. Opening the SPL Thrust Balance Program:
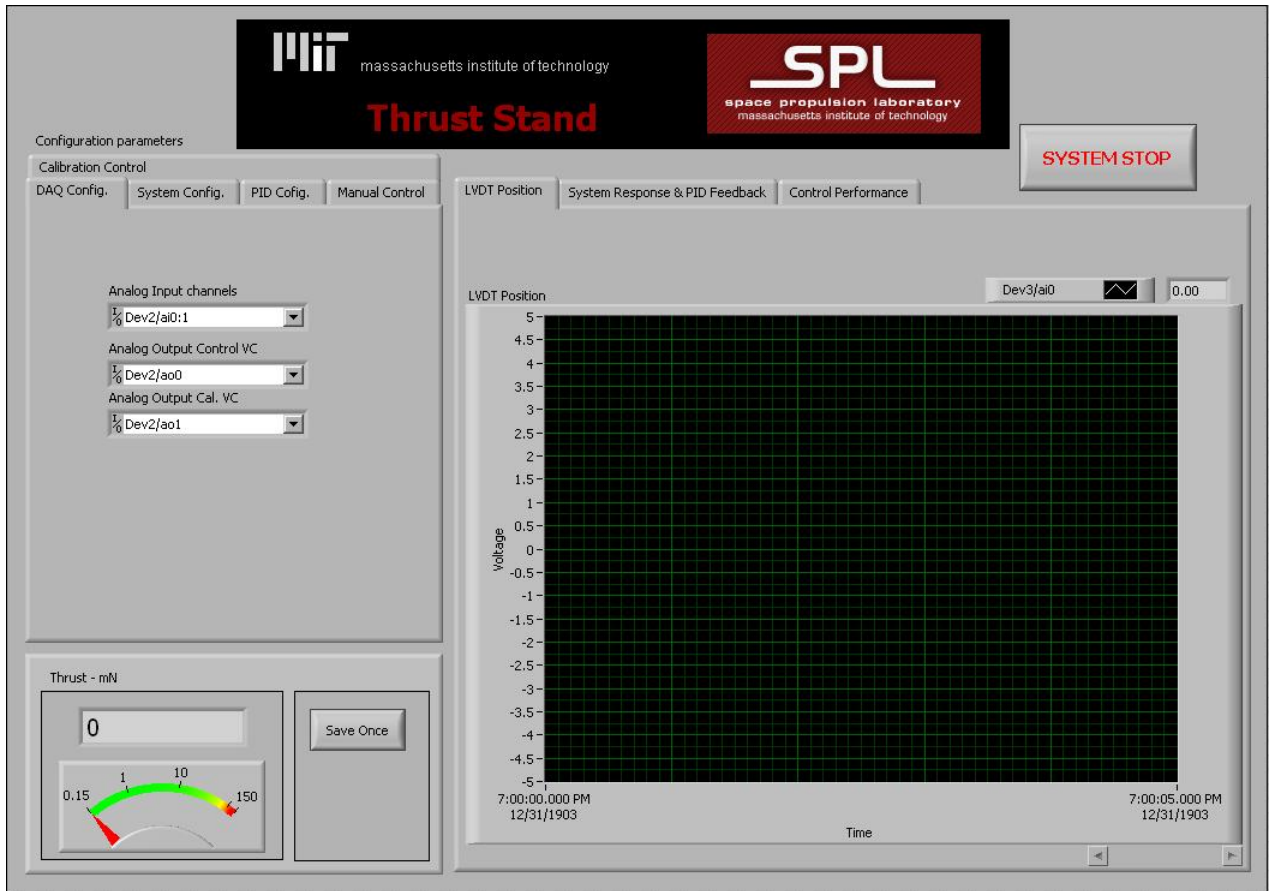
Figure 4.5: The Labview Software User Interface.

- At the SPL desktop computer, select the "start" menu, then "search", then "files and folders".

- Locate the Labview Project File called "MIT SPL Thrust Balance" and open this program.

- The project file will have a list of Labview VI's. Open the program "MIT-SPL Thrust Balance-5-1". The screen in figure 4.5 should appear.

2. Configuring the DAQ card:

- Under the configuration parameters on the left, select the "DAQ Config." tab.

- For the Analog Input Channels, select "ai0:1" for the correct device number.

93
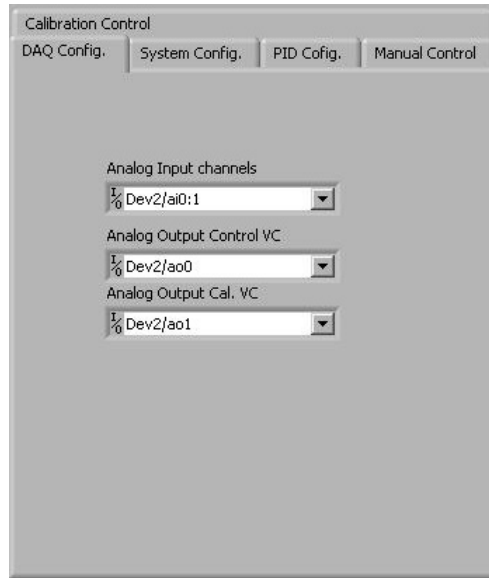
Figure 4.6: DAQ Configuration tab.

- For the Analog Output Control Voice Coil, select "ao0" for the correct device number.

- For the Analog Output Calibration Voice Coil, select "ao1" for the correct device number.

3. Configuring the primary, PID voice coil:

- Under the configuration parameters on the left, select the "Manual Control" tab.

- This tab will feature a large knob to manually control the voltage to the primary voice coil and a button to toggle the PID control software.

- Toggle the PID Control until the button turns red and says "PID Control Loop NOT Active: Manual Control Mode" as shown in figure 4.7.

4. Configuring the secondary, drift correcting voice coil:

- Under the configuration parameters on the left, select the "Calibration Control" tab.
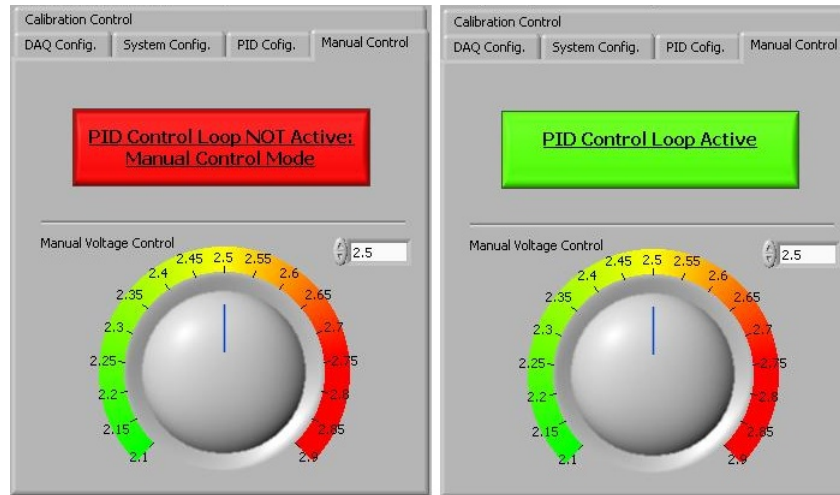
Figure 4.7: The PID control loop can be toggled on or off by simply clicking the button.

- This tab will feature another large knob to manually control the voltage to the drift correcting voice coil, and a button to turn this voice coil on or off.

- Toggle the button until it is red and says "Calibration Control OFF" as seen in figure 4.8.

5. Starting the program:

- Now the program is ready to run. Make sure the manual voltage control for both voice coils is set to 2.5V and select the "run" button (the arrow button just below the view menu).

- Choose a location to save the calibration data which will be collected later and name the file appropriately.

- IMPORTANT: If the program experiences any sort of problem or error during the experiment, use the "SYSTEM STOP" button to halt operation. The smaller stop button found next to the run button (with a small red octagon on it) should never be used. Pressing this button will not close down the program properly and may lead to significant problems during the next restart.
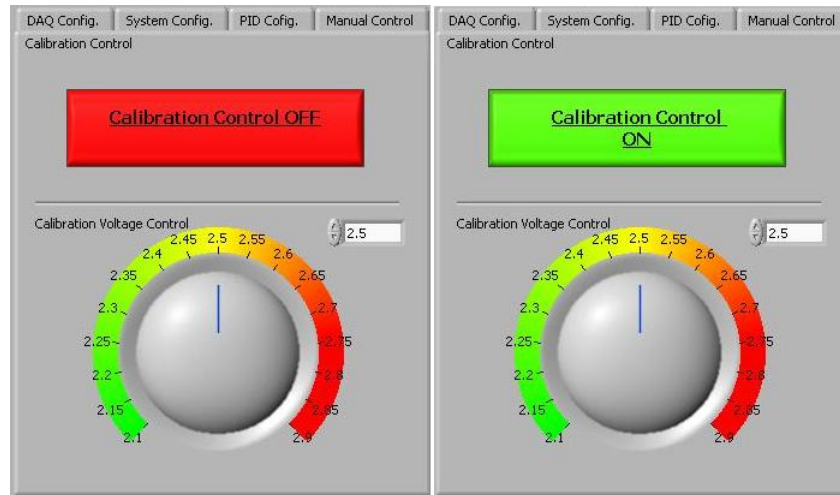
Figure 4.8: The calibration voice coil can be toggled on or off by simply clicking the button.

- On the right hand side of the program is a series of graphs. Select the "LVDT Position" tab. This will give the current position of the LVDT.

- Go back to the "Calibration Control" tab on the left. Turn the calibration control on by clicking on the red button. It should turn green with the text "Calibration Control ON".

- Now go to the System Response & PID Feedback tab. There will be a series of lines on this graph representing the following:

  - The white line is the LVDT position.

  - The green line is the set point.

  - The red line is the power the PID software is commanding to the primary voice coil.

- When the LVDT (white line) displaces, the computer will work to bring it back to the set point (green line) by using the voice coil's force (red line).

- Return to the manual control tab and turn the PID control on (button should now be green). Allow the system to reach steady state. It is now ready for calibration.

4.1.4 External calibration procedure and producing a calibration curve

Before calibration can begin, the PID loop must reach a relatively constant state. This will occur when the voice coil's voltage sits at a steady value (to approximately two decimal places). The voltage can be seen in the box in the bottom left corner of the software user interface. Once this number remains relatively constant, calibration can begin.

1. First, calibration points should be collected with no force on the balance. Click the "Save Once" button 5 to 8 times to include some zero force data points in the file.

2. Turn the spool on the calibration stand so that only the first weight contributes a force. Allow the voltage reading to settle again and click the "Save Once" button another 5 to 8 times to collect data at this force point.

3. Repeat this process for each of the 18 weights on the spool. Once the voltage has been recorded for each point, begin collecting data for each point that is removed. This will be used for hysteresis examination later.

4. Once the calibration is complete, shut down the software and turn off the control box. All of the pre-testing setup and calibration is complete. The next step is to prepare the chamber and the DCF for use.

5. With the calibration finished, carefully disconnect the fishing line from the DCF and remove the external calibration stand from the chamber. Close the chamber and begin roughing it down to a lower pressure.

To establish a relationship between voice coil voltage and thrust force, the voltage readings gathered during the calibration process should be plotted against the force that was pulling on the balance. The force values of this graph can be found in the calibration section of this thesis (table 3.2). The voltages should be adjusted so that they start at zero, which is accomplished by subtracting the value of the voltage with zero weight force from all of the voltage values. The resulting points of force
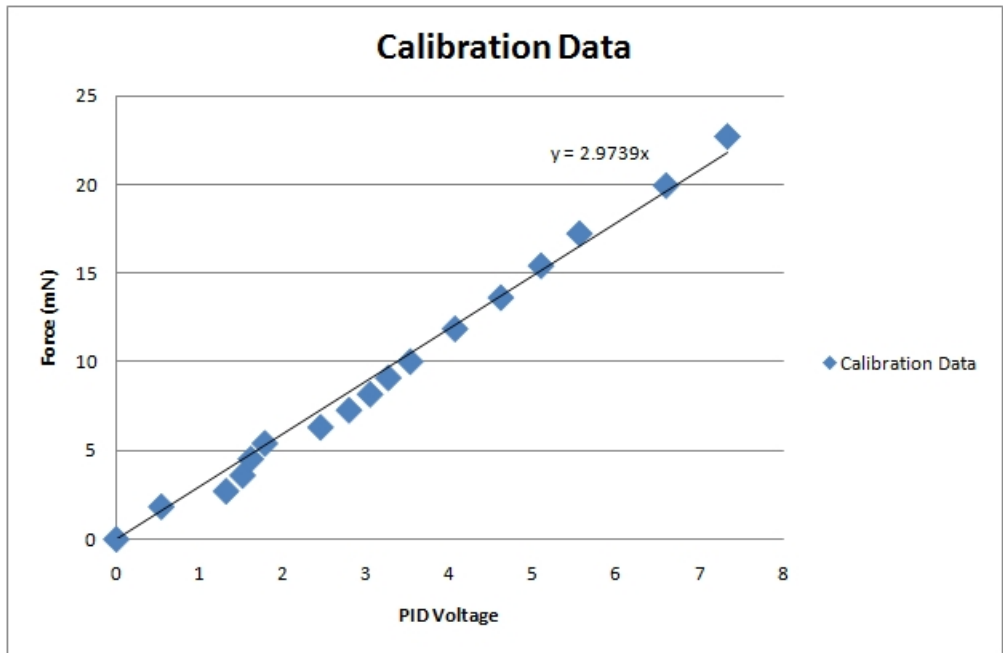
Figure 4.9: Example calibration curve relating voice coil voltage to thrust force.

and voltage should produce a plot similar to the one seen in figure 4.9. The curve appeared linear for the force range that was tested, therefore a linear fit line was added to the plot. The equation for this linear line provides the relationship between voice coil voltage and force.

4.1.5 DCF Thrust Balance Test Procedure

With the calibration curve complete, the vacuum chamber can now be sealed and depressurized. The amount of time it takes for the chamber to be pumped down to vacuum and for the DCF to be prepared for use is in the range of 12 to 24 hours. Once the process is complete and the DCF is ready, the first action should be to check the system for any drift. Once the PID control has been activated, the goal should be to get the voice coil voltage to the same value at the start of calibration. The voice coil voltage with zero force is adjusted using the drift correcting voice coil. Once the voice coil voltage is where it was at the beginning of calibration, the gas flow to the thruster should begin. After measuring the thrust created just by the gas flow, the thruster can be started. It is recommended that measurements be taken
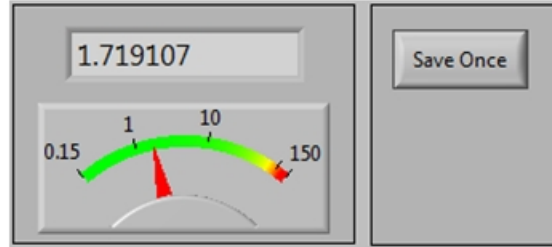
Figure 4.10: Voice coil's voltage reading as seen in the Labview software.

in incremental steps of anode power to reduce the uncertainty in the measurement, or more specifically, the effects of hysteresis. The hysteresis and other sources of uncertainty with the DCF's thrust balance will be discussed in the next subsection.

4.2 Uncertainty Analysis of the Thrust Measurements

The calibration plot shown in the previous section is the curve being used to calculate the thrust measurements, and therefore, the accuracy of this graph will determine the accuracy of the thrust values obtained during the experiment. There are four sources of uncertainty associated with the calibration curve: resolution, hysteresis, drift, and linearity.

The most obvious source of error comes from the resolution of the two variables in the calibration graph, the voice coil voltage and the weight force. The voice coil's voltage is read from the Labview software, as shown in figure 4.10. While the voltage may appear to have a high resolution, in reality, the voltage is only reliable to a certain number of decimal places. The voltage value is given in terms of a percentage of the total voltage the system can supply. Figure 4.10 shows a value with five trailing decimal places, but only the first two decimal places truly settle to a steady state value, while the others will constantly fluctuate. This is a result of the sensitivity of the voice coil; it is unable to provide a reliable force below that percentage of the system's output voltage. For that reason, the uncertainty in the voice coil voltage reading was taken as ± 0.05.

There is also an uncertainty from the resolution of the force acting on the balance during calibration. This resolution comes from the accuracy of the scale used to
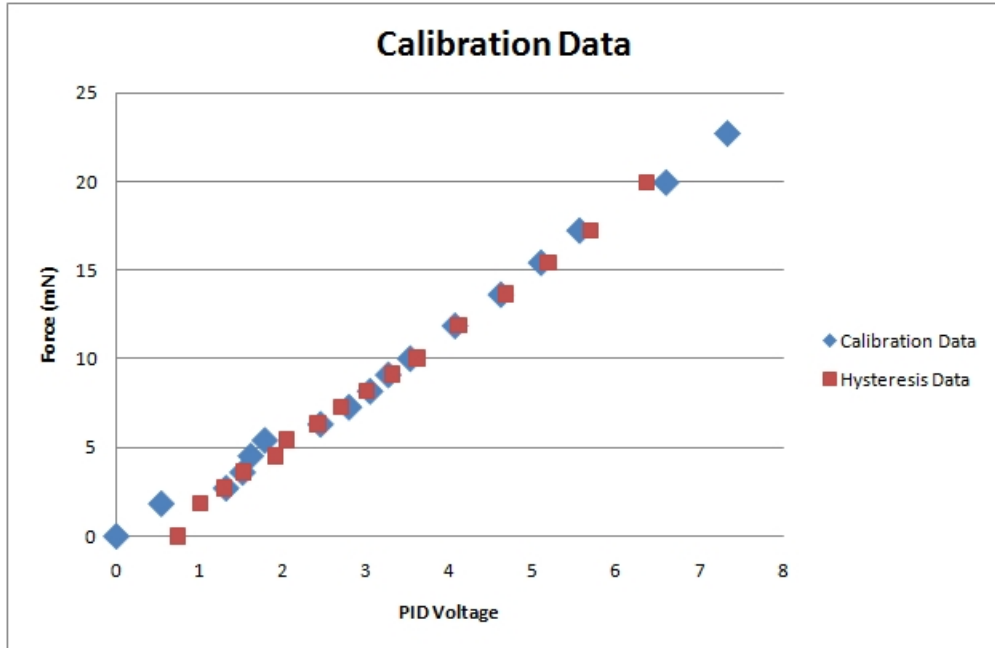
Figure 4.11: Hysteresis exhibited during calibration.

measure the weights themselves and the accuracy of the friction coefficient used to find the friction force acting between the Teflon cylinder and fishing line. The value of the weight hanging on the line should be very accurate since the sensitivity of the scale used to measure the weights was ± 0.00098mN. The average coefficient of friction between the Teflon cylinder and the nylon fishing line was found to be 0.055, but over the four trials, this value varied by about ± 0.0275. This translates to an accuracy of $\pm 0.0385T_2$ for the tension force pulling on the balance, where T_2 is the hanging weight force. The accuracy of each amount of hanging weight force is outlined in table 3.2 of the calibration section of this thesis.

Another source of error is the hysteresis. Hysteresis error refers to the difference between an upscale sequential test and a downscale sequential test[8]. In the case of the thrust balance, calibration points were taken for each added weight, and then again, as each weight was taken away. The measurements above 3mN seemed to be very consistent, with the second set of measurements falling almost directly on top of the originals. Below 4mN, the second measurements started to deviate more dramatically. The graph shown in figure 4.11 shows the data obtained from adding

100

weight sequentially to obtain a calibration curve along with the data obtained from sequentially removing the weights. Above 3mN, this results in an uncertainty of ±0.1 in the voice coil voltage. Below 3mN, the uncertainty rises to about ±0.5. This hysteresis seen during calibration is possibly the effect of retentivity occurring in the voice coil's magnetic core [18]. The effect of retentivity means that magnetic dipoles in the magnetic core line up in one fashion as the magnetic field increases, and then line up in a slightly different fashion when the field decreases [18].

Beyond the inaccuracies that arise from the resolution of the instruments and hysteresis, a couple of less quantifiable sources of error exist as well. It is assumed that there will be some drift during the time between calibration and measurement, and that this drift will not change the calibration curve if corrected by the secondary voice coil. Initial investigations seemed to confirm that this assumption is correct. A calibration curve was created before the first thrust measurement taken with the DCF and again after testing was complete. During the second calibration, the drift correcting voice coil was used to fix the zero force voltage point to the same value used in the first calibration. When this was done, the second curve validated the first. Another possible source of error comes from the linear fit that was applied to the calibration data. The relationship between voice coil voltage and thrust force was presumed to be linear. Multiple calibrations of the thrust balance confirmed that this assumption was also true. In all attempted calibrations, the relationship between force and voltage remained linear.

With the known sources of error in resolution and hysteresis, error bars can be added to the calibration curve. It is worth noting that the error is rather high between 0 and 3 mN, and rather low between 4mN and 16mN.

4.3 Initial Results from the DCF's Thrust Characterization with the Thrust Balance

Using the procedure from the previous section, the thrust balance measured thrust while anode power and flow rate were simultaneously recorded. Since ASTROVAC
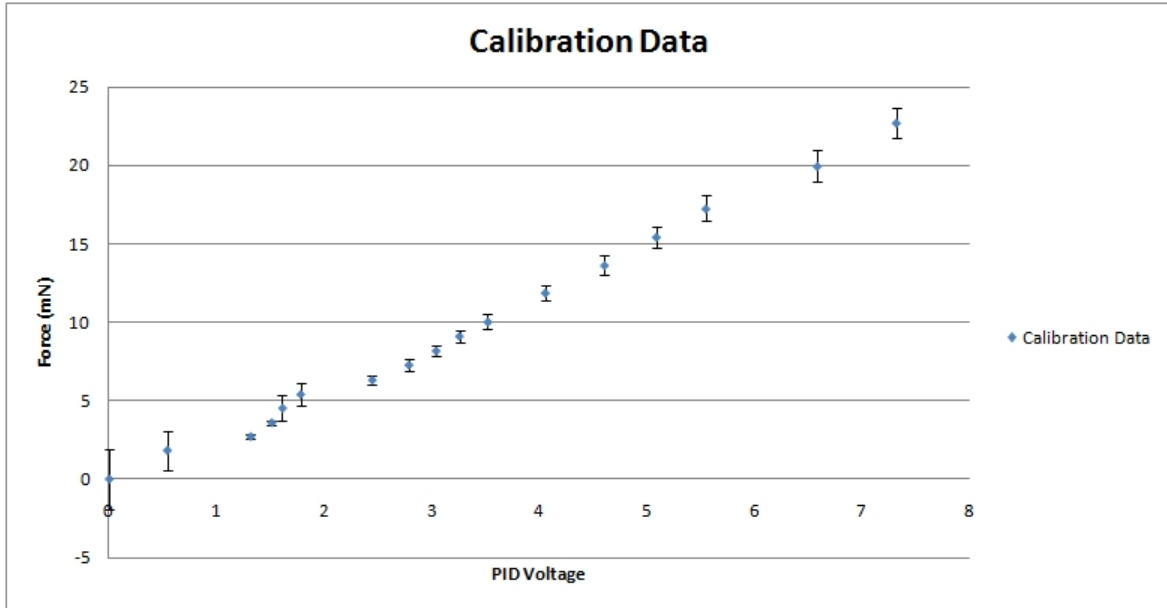
Figure 4.12: Error bars providing the uncertainty in the calibration data.

had only one working cryopump at the time of the initial testing phase, anode flow rates could not exceed 6 standard cubic centimeters per minute (sccms). Typical operating flow rates would be between 4 sccms and 10 sccms. Figure 4.13 shows the thrust results obtained for anode flow rates of 4 sccms and 6 sccms with power levels between 0 and 125 watts.

When higher anode power levels were tested, an unexpected event occurred. The DCF operates in two current modes, and above 125 watts it begins to run in its higher current mode (shown in figure 4.14). When this occurred, the additional plasma emitted from the DCF began to interact with the wiring of the LVDT and primary voice coil, causing the PID software to fluctuate wildly and eventually terminate. Although shielding already existed over the 9 pin cable and LVDT wiring, it was not enough to protect the system from this increased amount of plasma in the chamber during high current operation. Due to the difficulties of having just one cryopump and not enough shielding, initial characterization of the DCF was restricted to the 0 to 125 watt range, with a maximum anode flow rate of 6 sccms.

Figure 4.13: Thrust versus Anode Power for the DCF under anode flow rates of 4 sccms and 6 sccms. The cathode flow rate was between 1 and 2 sccms.

Figure 4.14: Diverging Cusped Field thruster in operation on the thrust balance. The DCF has two modes: low current (left) and high current (right).

5 Conclusions

The results from initial testing of the thrust balance with the Diverging Cusped Field thruster showed that the balance was a success. It was able to produce thrust measurements at various anode power levels, and additional trials indicated that the results obtained were repeatable.
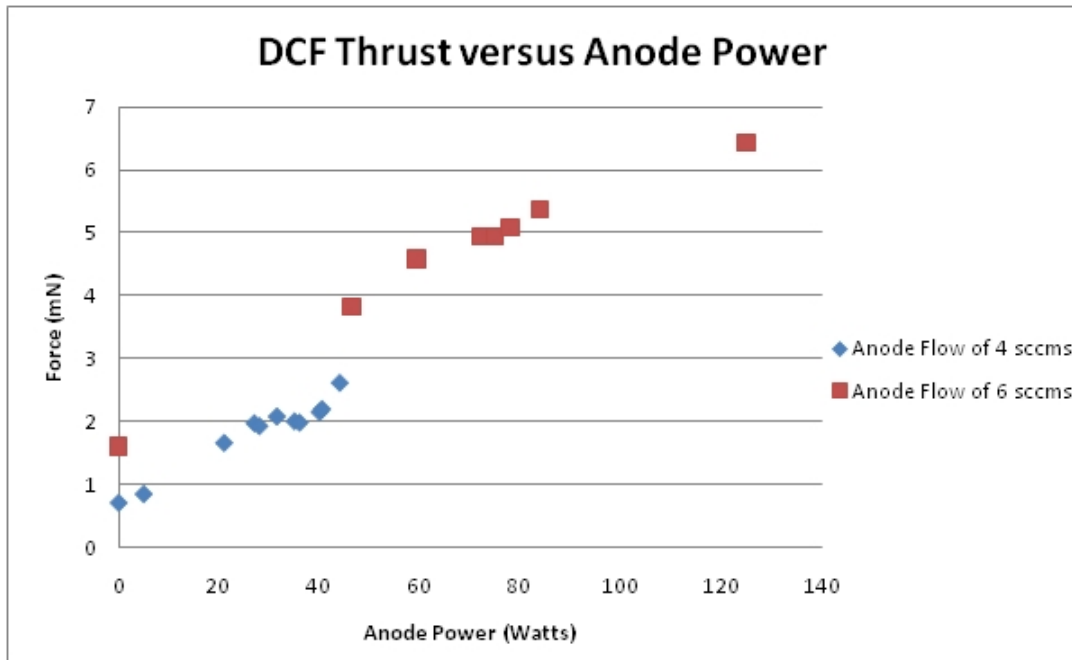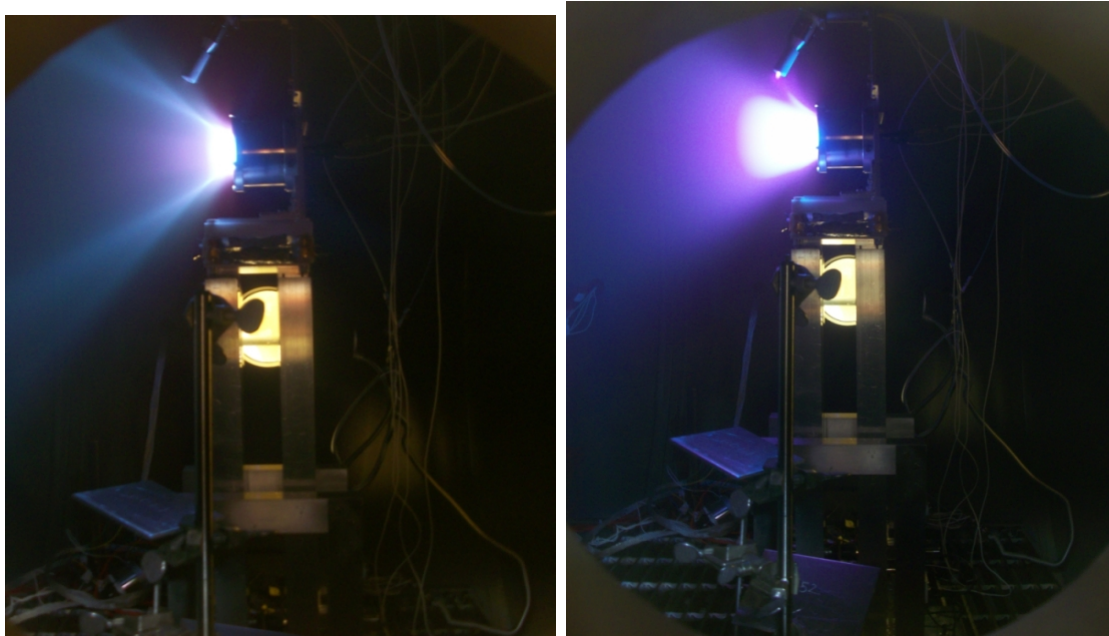
5.1 Established range and accuracy of the SPL Thrust Balance

Through calibration, the thrust balance proved that it can operate over a range of 0mN to 23mN, maintaining accuracies of less than $\pm$1.2mN throughout this regime. Above 3mN, the accuracy improves to about $\pm$0.5mN on average. The thrust balance successfully determined the DCF's thrust range to be between 3mN and 6mN for anode power levels from 45 watts to 125 watts, all at a flow rate of 6 sccms. It also determined the DCF's thrust range to be between 0.5mN and 2.5mN for anode power levels from 5 watts to 44 watts, all at a flow rate of 4 sccms.

5.2 Future Work

While the SPL thrust balance is considered operational, there are several minor issues still left to explore. First, the natural damping present in the balance itself needs to be characterized. Having an idea of how quickly the system can automatically damp its motion may explain why no derivative gain was needed in the PID control. Second, the variation in the coefficient of friction associated with the calibration system is larger than ideal. The uncertainty in the friction coefficient over the four trials in table 3.1 was about $\pm$60%, leaving the value of the force pulling on the balance uncertain by about 5%. This could be the result of an uneven coefficient of friction across the Teflon cylinder itself, and therefore, to get better results, this cylinder should probably be replaced by some sort of rotating pulley.

Also of concern is the effectiveness of the thermal insulation layer. While it does an excellent job protecting the thrust balance from any heat transfer, that heat now remains in the thruster itself. This could lead to overheating if the engine is used at

higher power levels for long periods of time. Some sort of cooling system may need to be implemented to keep the thruster at reasonable temperatures. Small improvements to the design should also be considered, such as better shielding for the LVDT and voice coil wires, or aesthetic changes like reducing the number of decimal places in the voice coil voltage value reported by the Labview software. The voltage value is only accurate to about two decimal places, but as many as six are given. Some sort of vibrational base test should be added to the thrust balance's operational procedure as well. Such a test could allow the user to adjust the counterweight position until the vibration sensitivity goes to zero.

Finally, it would be beneficial to compare the thrust measurements from the thrust balance with those obtained from another thrust measuring device. That way, any future measurements taken with the thrust balance would be assured to have the highest possible degree of validity.

Appendix A

Analysis of Using Sheet Metal to Connect the Pendulum Legs to the Top Plate
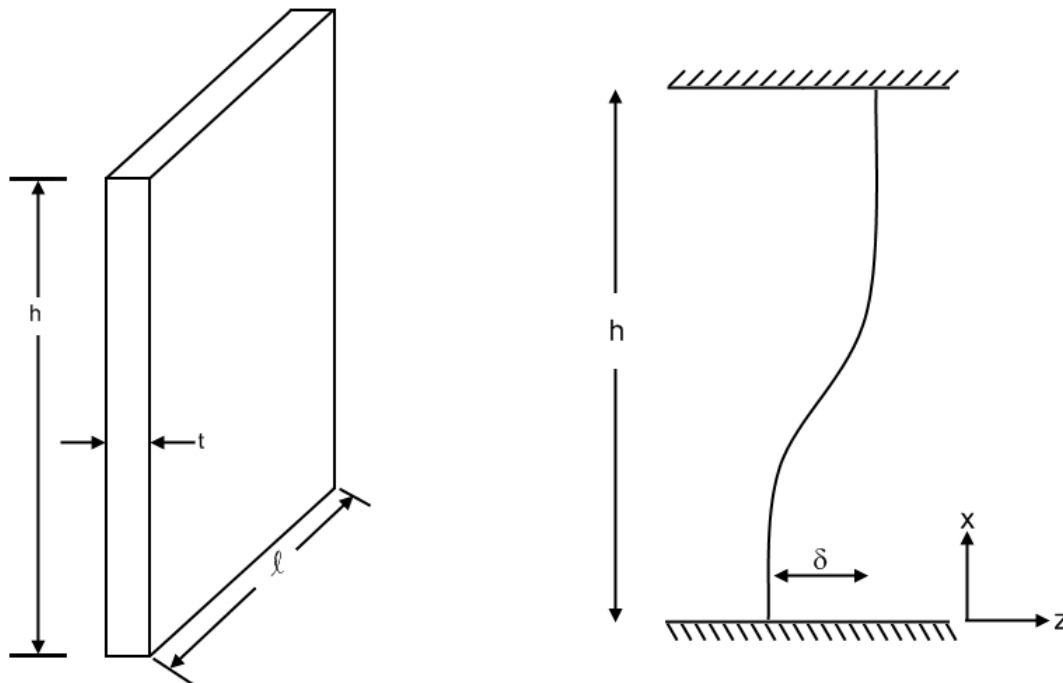
Figure A.1: Sheet metal in compression.

The figure above shows the dimensions of a theoretical metal plate attachment as well as the result of putting a compressive force on the sheet. At a high enough force the sheet metal will exhibit a buckling reaction. The moment of inertia for the metal plate is:

$$I = \frac{1}{12}\ell t^3$$

Where ℓ is the length of the plate and t is the thickness as noted in the figure. The equation for the force along the z axis is as follows[3]:

$$EI\frac{d^2z}{dx^2} = F(x - h)$$

Here, E is the modulus of elasticity, x is the vertical position, h is the height, z is the horizontal position, and F is the compressive force. Integrating this equation produces:

$$EI\frac{dz}{dx} = F\left(\frac{x^2}{2} - hx + C_1\right)$$

$$EIz = F\left(\frac{x^3}{6} - h\frac{x^2}{2} + C_1x + C_2\right)$$

Using the boundary conditions will provide the values for the constants C_1 and C_2:

$$at\ x = h,\ \frac{dz}{dx} = 0 \Rightarrow C_1 = \frac{h^2}{2}$$

$$at\ x = 0,\ z = 0 \Rightarrow C_2 = 0$$

So the equation now becomes:

$$EIz = F\left(\frac{x^3}{3} - h\frac{x^2}{2} + \frac{h^2}{2}x\right)$$

If the compressive force causes a displacement δ in the z direction at the end of the

107

sheet $(x = h)$, then an equation for the displacement under a load F can be found:

$$\delta = \frac{F}{EI} \left(\frac{h^3}{6} - \frac{h^3}{2} + \frac{h^3}{2} \right)$$

$$\delta = \frac{Fh^3}{6EI}$$

From this equation that relates displacement to force, the stiffness k can be found assuming the behavior is linear:

$$F = k\delta$$

$$k = \frac{6EI}{h^3} = \frac{E\ell t^3}{2h^3}$$

Depending on the loading of these sheet metal pieces, the critical load can be found with one of two equations:
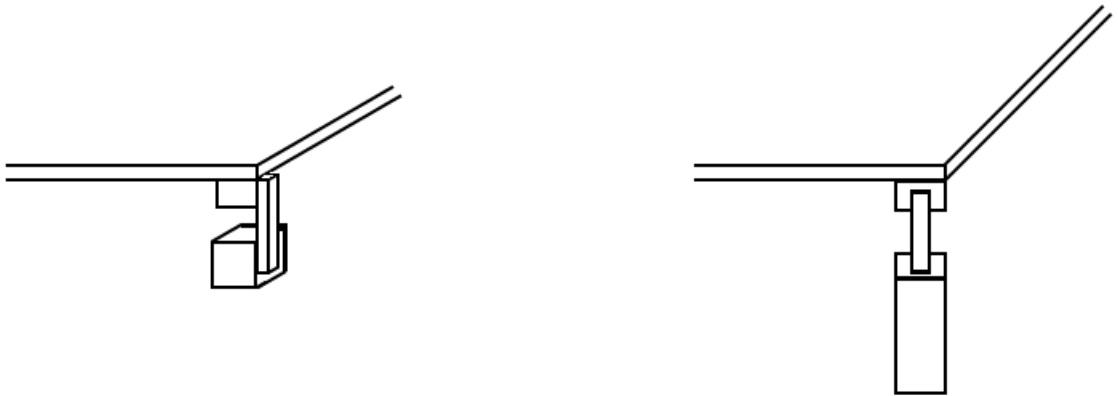
For a connection of the first type, the critical load force is[3]:

$$P_{crit} \approx \frac{\pi^2 EI}{h^2}$$

108

For a connection of the second type, the critical load can be four times higher[3]:

$$P_{crit} \approx \frac{4\pi^2 EI}{h^2}$$

It can be assumed that the DCF is approximately 4 kilograms, and that an appropriate safety factor of at least 2 should be considered for each plate. If the sheet metal is made from aluminum, the modulus of elasticity is also known.

Given:

$m_{DCF} = 4kg$

$S.F. = 2.0$

$m_{tot} = 9kg \Rightarrow P_{crit} = 78.4N$

$E_{Al} = 7 \times 10^{10} Pa$

$h = 1cm = 0.01m$

$\ell = 0.5cm = 0.005m$

Reasonable approximations for the height and length of the sheet metal that keep it in proportion to the thrust balance have also been made. Using these, the thickness becomes:

$$\frac{P_{crit}}{4} = \frac{4\pi^2 EI}{h^2} \Rightarrow I = \frac{P_{crit}h^2}{16\pi^2 E} \Rightarrow t = \left(\frac{3P_{crit}h^2}{4\ell\pi^2 E} \right)^{1/3} = 0.12mm$$

So if the weight were divided evenly between the sheet metal in the sturdier loading position, a minimum thickness of 0.12 mm would be required to hold the DCF. This translates to a stiffness value shown below:

$$k = \frac{E\ell t^3}{2h^3} = 297.9\frac{N}{m}$$

So each plate would have a stiffness of just under 300 N/m. This is far too high for the stand to deflect any measurable amount under the thrust of the DCF. Clearly the flexible pivots will be necessary here.

Analysis of Using Sheet Metal to Connect the Pendulum Legs to the Bottom Plate

A buckling analysis is no longer necessary for the sheet metal connections to the bottom plate because these are acting in tension. In this case, the material will fail when the stress exceeds the ultimate tensile strength rating of the material. Assuming the material is aluminum, the ultimate tensile strength will be at least 324 MPa [3]. To produce such a stress under the counterweight, which weighs 78.4N (and each piece of sheet metal would need to support a fourth of this total weight), the cross sectional area turns out to be very small.

$$A = \frac{F}{\sigma} = \frac{\frac{1}{4}(78.4N)}{324 \times 10^6 Pa} = 6.05 \times 10^{-8} m^2 = 0.0605 mm^2$$

Assuming that the height and width of the sheet metal remain the same as they were in the previous section, the required minimum thickness now becomes 0.0121mm. With this thickness, the smallest stiffness possible will be much less than before.

$$k = \frac{E\ell t^3}{2h^3} = 0.31 \frac{N}{m}$$

Appendix B

Data from Thermal Testing

Figure B.1: Temperature rise for a change in power from 0W to 17.3W

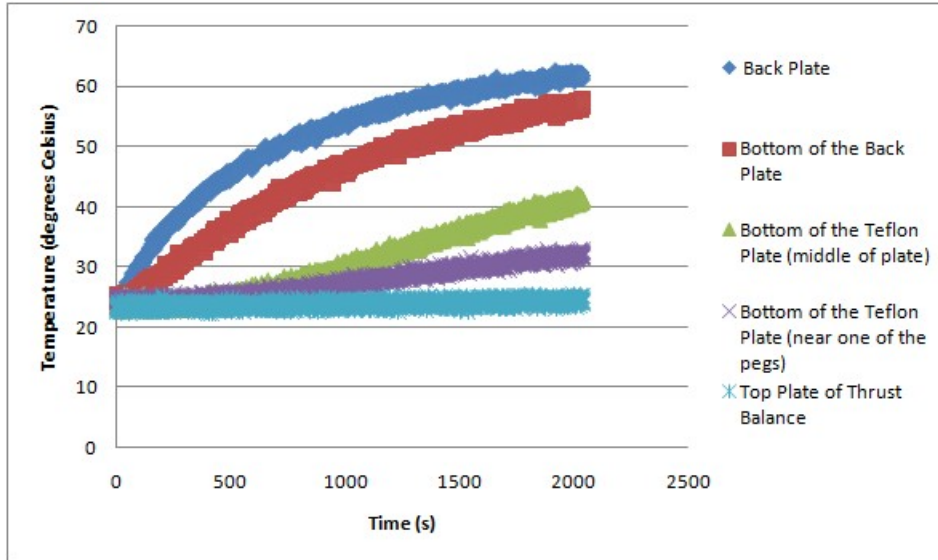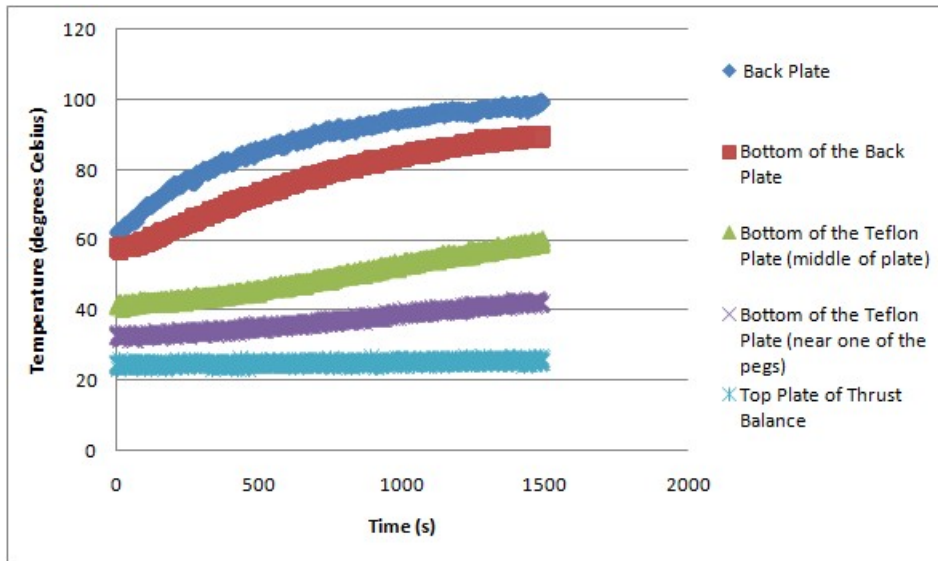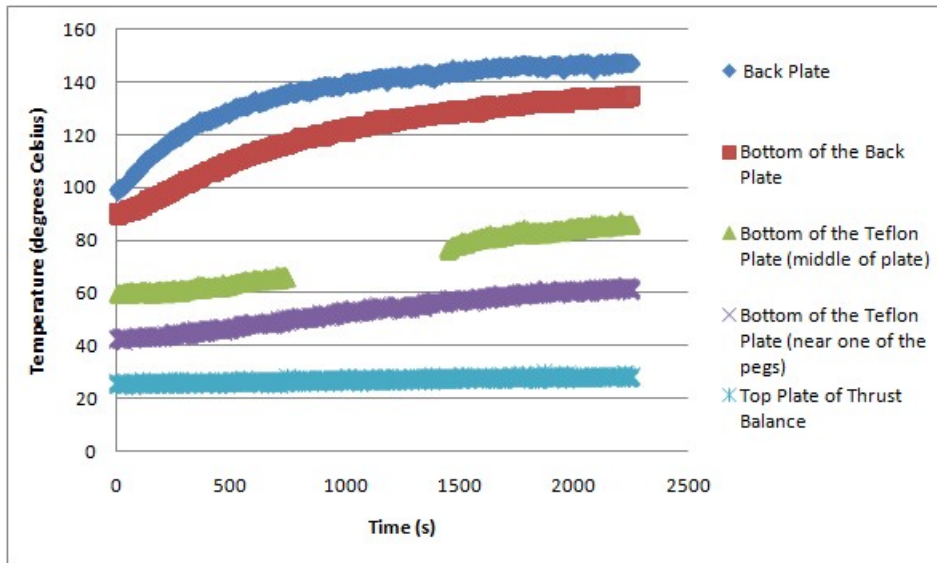Figure B.2: Temperature rise for a change in power from 17.3W to 38.9W.

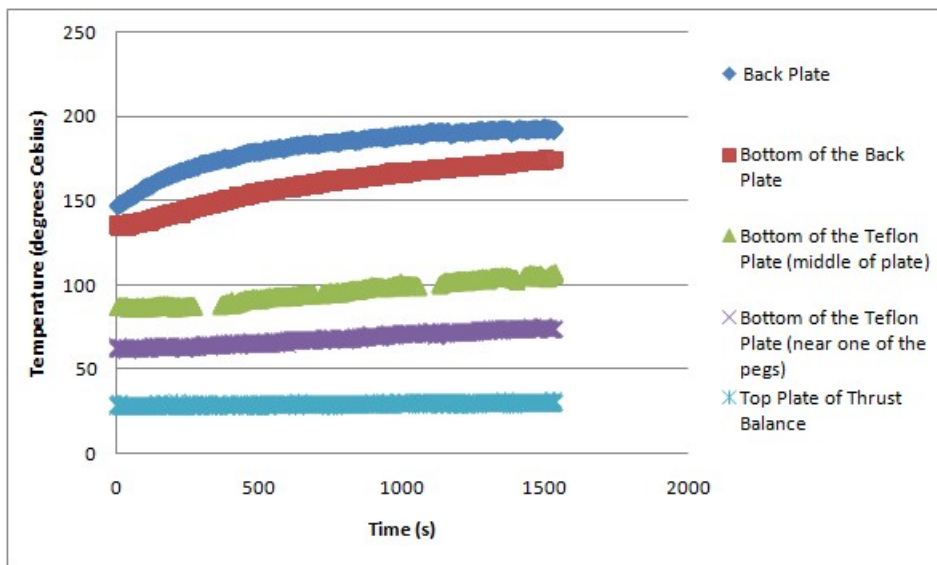Figure B.3: Temperature rise for a change in power from 38.9W to 69.2W.

Figure B.4: Temperature rise for a change in power from 69.2W to 108W.
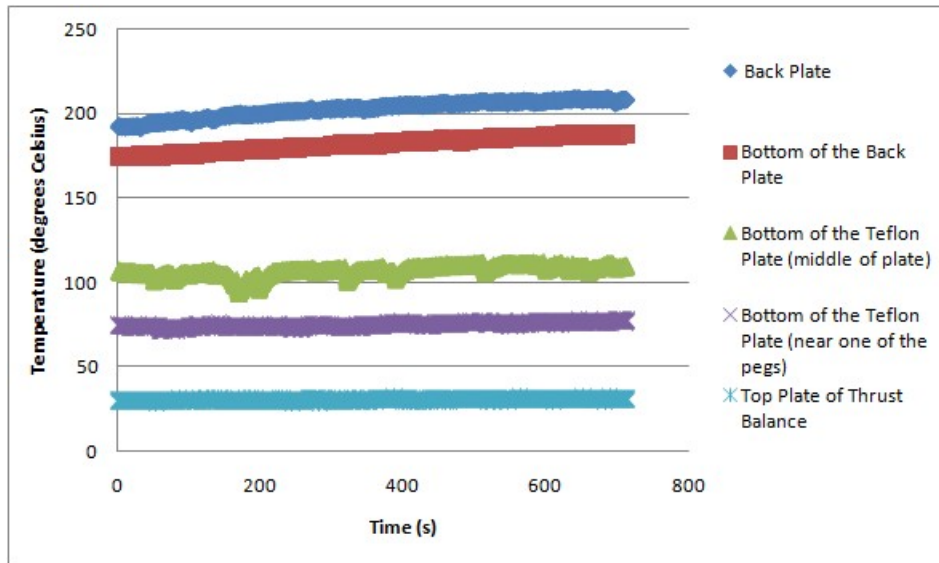
Figure B.5: Temperature rise for a change in power from 108W to 130W.

Appendix C

Data Sheets:

1. Riverhawk Flexural Pivots

2. Linear Variable Differential Transformer

3. Voice Coil

4. NI 6009 DAQ Card

The Free-Flex® Pivot

The Free-Flex® Pivot is a simply packaged, compact and easily installed limited rotation bearing with predictable and repeatable performance. The pivot is made of flat, crossed springs supporting rotating sleeves. Originally patented by the Bendix Company in 1961, to date over eight million pivots have been put into service. The product line was purchased by the Riverhawk Company in 2004.

The Free-Flex® Pivot is a frictionless, stiction-free bearing uniquely suited for limited angular travel. Flex pivots are designed for applications that do not permit lubrication yet demand precise positioning and require infinite life. Along with a wide range of industrial applications, additional applications include guidance systems for missiles, scanning mirror assemblies for both satellites and ground applications, jet engine fuel control, and vibration sensors. Flexural pivots are the product of choice any time reliable, predictable rotation is needed.

A variety of pivot sizes and ratings are available in both cantilevered (Series 5000) and double-ended (Series 6000) designs. We are also fully capable of special designs and have all the testing equipment necessary to examine every mechanical property of our flexural pivots to include: fatigue testing, center shift testing, torsional spring rate testing, concentricity, roundness, radial/axial spring rate and static load testing. We also have a full metallurgy lab to perform a metallographic analysis.

Flexural pivots are made from 410 and 420 stainless steel for standard construction. Special materials have included Custom 455 Stainless, Inconel 718, Titanium and Maraging Steel. Special configurations have included flanges, grooves, flats, special spring rates, special lengths and gold plating.

Evolution of the Free-Flex® Pivot

- **Bendix 1955**
- **Allied 1982**
- **Allied Signal 1988**
- **Lucas 1990**
- **Lucas Varity 1996**
- **TRW 2000**
- **Goodrich 2002**
- **Riverhawk 2004**

Major Performance Characteristics

- High radial stiffness
- High axial stiffness
- Frictionless
- Stiction-free
- Not susceptible to false brinelling
- Low hysteresis
- Low center shift
- Exceptional repeatability
- Predictable performance
- Lubrication not required
- Maintenance not required
- Electrical continuity
- Infinite cycle life (See life curves)
- Ambient temperature range of - 400°F to +1200°F

Cutaway of Double-Ended Design

Additional Characteristics

- Radiation Resistance
- Low Thermal drift
- No Rubbing surfaces
- Contaminant tolerant
- Operates in vacuum of space
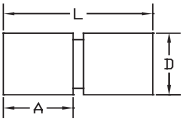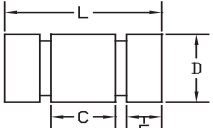- Self – centering
- Resolution to the micro inch range

Cutaway of Cantilevered Design

Visit our website at: www.flexpivots.com

Dimensions & Characteristics

Typical Units

Nominal Outside Diameter (Inch) D +0.00 -0.0005	Catalog Number Series 5000 Cantilevered (size-type)	Load Capacity (Pounds) Load At Center of "A". Vc	Vt	L +/- 0.003	A +/- 0.005	Catalog Number Series 6000 Double Ended (size-type)	Load Capacity (Pounds) Load At Center of "C". Vc	Vt	L +/- 0.003	B +/- 0.005	C +0.005 -0.015	Torsional Spring Rate (in-lb/Degree) See Note (2)
	5004-400	25.5	25.5			6004-400	28.0	28.0				0.0140
0.1250	5004-600	8.9	13.0	0.200	0.095	6004-600	17.7	25.0	0.200	0.045	0.085	0.0017
	5004-800	0.97	3.7			6004-800	2.20	4.7				0.0002
	5005-400	39.5	39.5			6005-400	44.0	44.0				0.0279
0.1562	5005-600	13.8	20.0	0.250	0.120	6005-600	27.6	39.0	0.250	0.057	0.110	0.0035
	5005-800	1.50	6.0			6005-800	3.50	7.4				0.0004
	5006-400	56.0	56.0			6006-400	63.0	63.0				0.0473
	5006-600	19.8	28.0	0.300	0.142	6006-600	39.6	56.0	0.300	0.067	0.130	0.0057
0.1875	5006-660	12.2	20.2									0.0037
	5006-800	2.1	8.0			6006-800	4.9	9.0				0.0007
	5008-400	101.0	101.0			6008-400	113.0	113.0				0.1141
0.2500	5008-600	35.5	51.0	0.400	0.190	6008-600	70.7	100.0	0.400	0.090	0.175	0.0143
	5008-800	3.7	14.5			6008-800	8.5	19.0				0.0018
	5010-400	158.0	158.0			6010-400	176.0	176.0				0.2234
0.3125	5010-600	55.0	79.0	0.500	0.238	6010-600	110.0	156.0	0.500	0.112	0.220	0.0286
	5010-800	5.8	23.0			6010-800	14.0	29.0				0.0036
	5012-400	228.0	228.0			6012-400	253.0	253.0				0.3840
0.3750	5012-600	80.0	114.0	0.600	0.285	6012-600	159.0	225.0	0.600	0.135	0.265	0.0480
	5012-800	8.4	32.8			6012-800	19.8	42.0				0.0058
	5016-400	403.0	403.0			6016-400	450.0	450.0				0.9080
0.5000	5016-600	141.0	202.0	0.800	0.380	6016-600	283.0	400.0	0.800	0.180	0.355	0.1134
	5016-800	14.6	58.0			6016-800	35.4	75.0				0.0142
	5020-400	634.0	634.0			6020-400	703.0	703.0				1.8500
0.6250	5020-600	222.0	317.0	1.000	0.475	6020-600	442.0	625.0	1.000	0.225	0.445	0.2321
	5020-800	23.0	93.0			6020-800	55.0	117.0				0.0295
	5024-400	910.0	910.0			6024-400	1013.0	1013.0				3.1800
0.7500	5024-600	318.0	455.0	1.200	0.570	6024-600	636.0	900.0	1.200	0.270	0.535	0.3980
	5024-800	33.0	130.0			6024-800	78.0	169.0				0.0500
	5032-400	1620.0	1620.0			6032-400	1800.0	1800.0				7.5200
1.0000	5032-600	567.0	815.0	1.600	0.770	6032-600	1131.0	1600.0	1.600	0.370	0.735	0.9390
	5032-800	60.0	236.0			6032-800	141.0	300.0				0.1175

(1) Pounds at zero deflection based on pure radial load. When the load is applied directly through a single spring, multiply capacity shown by 0.707.
(2) At zero load.

• Standard Materials:
Pivot Body: AISI 410 or AISI 420 corrosion-resistant steel. Flex elements: AISI 420 corrosion-resistant steel. Brazed Construction.

• Tighter Diameter Tolerance:
If a tighter diameter tolerance of (+0 / -0.0002) is required, specify T2 after the catalog number.

• Torsional Spring Rate:
Torsional Spring rates are generally within +/- 10% or less of the nominal values, however spring rates that are 0.0018 lb-in/degree or less may have significantly higher tolerances.

• General:
The correct pivot for a specific application can be selected only after determination of required angle of deflection, load, and life expectancy as these are interdependent. When unusual environments or multiplane loading conditions exist consult Riverhawk.

• Welded Construction:
Welded construction pivots are available. Consult Riverhawk for application engineering.

www.flexpivots.com

DC-EC AccuSens™ Series

General Purpose LVDT

The DC–EC AccuSens™ Series incorporates a unique monolithic chip combined with a computer-designed AC LVDT to achieve premium performance.

The ratiometric design of the monolithic circuitry compensates for power supply deviations for continuously stable operation. Unaffected by input variations, the transducer provides highly accurate, repeatable measurement.

Innovative manufacturing techniques further enhance the AccuSens operation and cost efficiency. Micro-miniature components used in the construction of each unit are selected for maximum stability.

Vacuum encapsulation of all elements produces an assembly tolerant to shock, vibration and other forms of physical abuse. Double magnetic shielding protects against stray electrical fields.

Features

❏ *Linearity 0.25% of FS or better*

❏ *CE certified*

❏ *Integrated signal conditioning*

❏ *Rugged stainless steel construction*

❏ *Calibration certificates supplied with all models*

Applications

❏ *General*

Options

❏ *Metric thread core*

❏ *Captive core option for convenient installation*

❏ *Guided core*

❏ *Small diameter, low mass core*

Specifications

Input Voltage	±15 VDC (nominal), ±25 mA
Operating Temperature Range	32°F to 160°F (0°C to 70°C)
Survival Temperature Range	-65°F to 200°F (-55°C to 95°C)
Null Voltage	0 VDC
Ripple	Less than 25 mV rms
Linearity	0.25% full range
Stability	0.125% full scale
Temperature—Coefficient of Scale Factor	0.04%/°F (0.08%/°C)
Shock Survival	250 *g* for 11 milliseconds
Vibration Tolerance	10 *g* up to 2 kHz
Coil Form Material	High density, glass-filled polymer
Housing Material	AISI 400 series stainless steel
Cable	4 conductor, 28 AWG, stranded copper with braided shield and polyurethane jacket, 1 meter
EMC	CE certified (The DC-EC series, when correctly installed, comply with the EMC Directive 89/336/EEC generic standards for residential commercial, light industrial and industrial environments.)
Output Impedance	Less than 1 ohm

Performance and Electrical Specifications[1]

DC–EC Series Model Number	Nominal Linear Range		Scale Factor		Response -3 dB
	inches	mm	V/inch	V/mm	Hz
050 DC–EC	±0.050	±1.25	200.0	8.00	500
125 DC–EC	±0.125	±3.0	80.0	3.20	500
250 DC–EC	±0.250	±6.0	40.0	1.60	500
500 DC–EC	±0.500	±12.5	20.0	0.80	200
1000 DC–EC	±1.000	±25	10.0	0.40	200
2000 DC–EC	±2.000	±50	5.0	0.20	200
3000 DC–EC	±3.000	±75	3.3	0.13	200
5000 DC–EC	±5.000	±125	2.0	0.08	200
10000 DC–EC	±10.00	±250	1.0	0.04	200

[1]All calibration is performed at room ambient temperature.

DC-EC models, when correctly installed, are CE certified to comply with the EMC Directive 89/336/EEC.

CE

How to Order

Specify the DC-EC Model followed by the desired option number(s) <u>added together</u>.

Ordering Example:
Model Number   050 DC-EC-200 is an DC-EC Series LVDT with a ±0.050" range (050 DC-EC), with the captive core option (200).
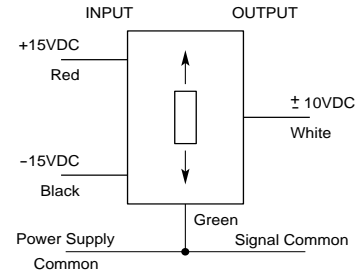
DC-EC Model

| 050 DC-EC |
| 125 DC-EC |
| 250 DC-EC |
| 500 DC-EC |
| 1000 DC-EC |
| 2000 DC-EC |
| 3000 DC-EC |
| 5000 DC-EC |
| 10000 DC-EC |

Options

Number	Description
006	Metric Thread Core
010	Guided Core
020	Small Diameter, Low Mass Core[1]
200	Captive Core[2]

[1] Consult factory for mass, dimensions and thread size.
[2] Available on 050 DC-EC through 3000 DC-EC models only.

Wiring

INPUT   OUTPUT

+15VDC
Red

± 10VDC
White

−15VDC

Black

Green

Power Supply   Signal Common
Common

Block Diagram

+15VDC   Red
         Grn
-15VDC   Blk

Reverse Polarity Protector → Oscillator → LVDT → De-modulator → Output Amplifier

Wht
±10VDC
Output Signal

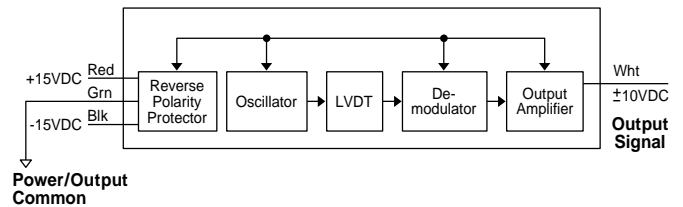**Power/Output Common**

New Captive Core Option!

The DC-EC features a captive core design that greatly simplifies installation. The design utilizes a core rod and bearing assembly that is captured and guided within the LVDT providing low friction travel throughout the stroke length. The assembly incorporates two Delrin bearings on the core rod traveling through the stainless steel boreliner. A bronze bearing on the front end utilizes a self-aligning feature to accommodate lateral LVDT movement during operation. The core rod and bearing assembly are field replaceable. **See page 71 for specifications.**
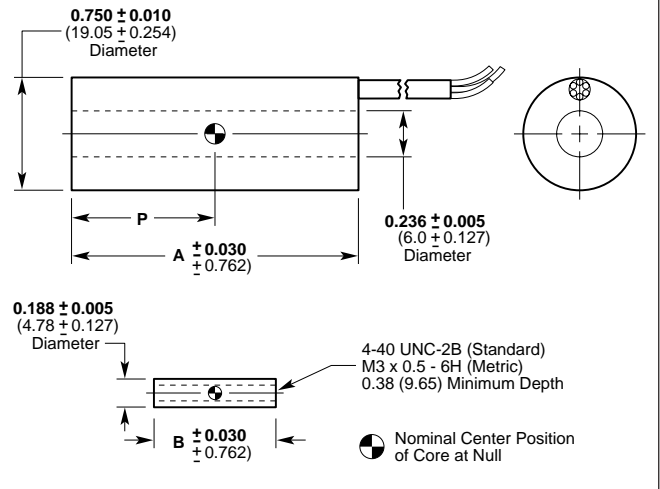
Dimensions   in (mm)

0.750 ± 0.010
(19.05 ± 0.254)
Diameter

0.236 ± 0.005
(6.0 ± 0.127)
Diameter

P

A ± 0.030
± 0.762

0.188 ± 0.005
(4.78 ± 0.127)
Diameter

B ± 0.030
± 0.762

4-40 UNC-2B (Standard)
M3 x 0.5 - 6H (Metric)
0.38 (9.65) Minimum Depth

Nominal Center Position of Core at Null

Mechanical Specifications

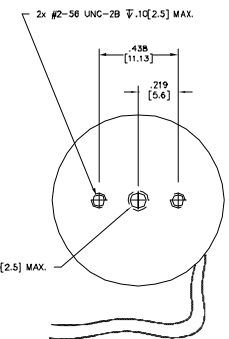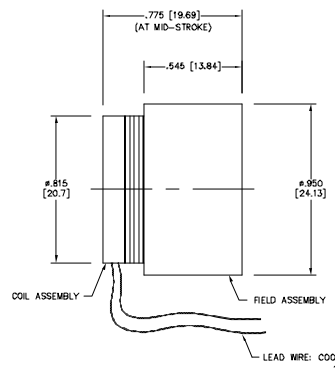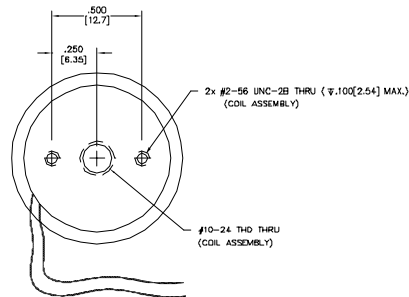| DC-EC Series | Weight | | | | Dimensions | | | | | |
| Model | Body | | Core | | A (Body) | | B (Core) | | P | |
Number	oz	gm	oz	gm	in	mm	in	mm	in	mm
050 DC–EC	2.19	62	0.07	2	2.10	53.5	0.75	19.1	0.50	12.7
125 DC–EC	2.44	69	0.11	3	2.93	74.5	1.25	31.8	0.93	23.6
250 DC–EC	2.58	73	0.18	5	3.80	96.5	2.00	50.8	1.35	34.3
500 DC–EC	2.93	82	0.28	8	5.49	139.5	3.00	76.0	2.20	55.9
1000 DC–EC	4.24	120	0.35	10	7.75	196.9	3.80	96.5	3.18	80.8
2000 DC–EC	5.47	155	0.46	13	11.12	282.5	5.30	135.0	4.88	134.6
3000 DC–EC	9.39	266	0.49	14	16.32	414.5	6.20	157.5	7.55	191.8
5000 DC–EC	11.47	325	0.60	17	20.15	511.8	6.20	157.5	9.53	242.0
10000 DC–EC	15.71	445	0.85	24	35.38	898.5	12.00	305.0	16.58	421.1

SCHAEVITZ SENSORS

WINDING CONSTANTS *	UNITS	TOL	SYMBOL	WDG A
DC RESISTANCE	OHMS	±12.5%	R	9.9
VOLTAGE @ F_P	VOLTS	NOMINAL	V_P	18.3
CURRENT @ F_P	AMPERES	NOMINAL	I_P	1.85
FORCE SENSITIVITY	OZ/AMP	±10%	K_F	13.0
	N/AMP	±10%		3.61
BACK EMF CONSTANT	V/FT/SEC	±10%	K_B	1.10
	V/M/SEC	±10%		3.61
INDUCTANCE ****	MICRO-HENRY	±30%	L	600

ACTUATOR PARAMETERS *	UNITS	SYMBOL	VALUE
PEAK FORCE **	OZ	F_P	24.0
	N		6.7
CONTINUOS STALL FORCE ***	OZ	F_{CS}	9.75
	N		2.7
ACTUATOR CONSTANT	OZ/√WATT	K_A	4.13
	N/√WATT		1.15
ELECTRICAL TIME CONSTANT	MICRO-SEC	τ_E	60.6
MECHANICAL TIME CONSTANT	MILLI-SEC	τ_M	5.3
POWER I²R @ F_P	WATTS	P_P	33.7
STROKE	± INCHES		0.100
	± MM		2.54
CLEARANCE ON EACH SIDE OF COIL	IN		0.035
	MM		0.89
THERMAL RESISTANCE OF COIL	°C/WATT	θTH	15.5
MAX. ALLOWABLE COIL TEMP.	°C	TEMP	155
WEIGHT OF COIL ASSEMBLY	OZ	WT_C	0.247
	G		7.0
WEIGHT OF FIELD ASSEMBLY	OZ	WT_F	1.16
	G		32.89

* AT MID-STROKE & 25°C AMBIENT TEMPERATURE
** 10 SECONDS AT 25°C AMBIENT & 155°C COIL TEMPERATURE
*** 25°C AMBIENT & 155°C COIL TEMPERATURE
**** MEASURED AT 1000 Hz

FORCE VECTOR
− +

.775 [19.69]
(AT MID-STROKE)

.545 [13.84]

ø.815 [20.7]   ø.950 [24.13]

COIL ASSEMBLY   FIELD ASSEMBLY

.500 [12.7]
.250 [6.35]

2x #2-56 UNC-2B THRU (▽.100[2.54] MAX.)
(COIL ASSEMBLY)

#10-24 THD THRU
(COIL ASSEMBLY)

2x #2-56 UNC-2B ▽.10[2.5] MAX.

.438 [11.13]
.219 [5.6]

#4-40 THD ▽ .10[2.5] MAX.

LEAD WIRE: COONER AS-155-28
2x #28 AWG
12.0[305] MIN LONG
(RED, BLACK)

3. A POSITIVE (+) VOLTAGE APPLIED TO THE RED LEAD WILL PRODUCE A FORCE ON THE COIL ASSEMBLY IN THE POSITIVE (+) DIRECTION.

2. DIMENSION IN BRACKETS ARE MILLIMETERS [MM] AND ARE FOR REFERENCE ONLY.

1. INTERPRET DIMENSIONS & TOLERANCES PER ANSI Y14.5M-1994.

NOTES: UNLESS OTHERWISE SPECIFIED

THIRD ANGLE PROJECTION

UNLESS OTHERWISE SPECIFIED
-ALL DIMENSIONS ARE IN INCHES
-BREAK SHARP EDGES .015 MAX.
-SURFACE ROUGHNESS √.63
-DIMENSIONS APPLY AFTER FINISH
-MAX FILLET R .015

TOLERANCED
DECIMALS   ANGULAR
X ± .03   ±0° 30'
XX ± .03
XXX ± .005

DO NOT SCALE DRAWING

DRAWN N. FRENCH DATE 12/17/98
MECH CHECK GUERRERO 06/29/05
APPD A. MORCOS 01/13/09
FILE NO. L:\TOP LEVEL\LA\LA10-08-000A

BEI KIMCO MAGNETICS DIVISION
VISTA, CA 92081

TITLE
LINEAR ACTUATOR

SIZE D   ITEM NO. 55789   DWG NO. LA10-08-000A   REV E
SCALE 4/1   SHEET 1 OF 1

LTR	ECO NO.	DESCRIPTION	DRN	APP'D	DATE
D	D60159	ADD RoHS LOGO	SLM	MG	03/07/06
E	D70211	CHG'D UNITS FOR INDUCTANCE & ELECT. TIME CONST.	JWT	MG	5/02/07

Low-Cost, Bus-Powered Multifunction DAQ for USB – 12- or 14-Bit, up to 48 kS/s, 8 Analog Inputs

NI USB-6008, NI USB-6009

- 8 analog inputs at 12 or 14 bits, up to 48 kS/s
- 2 analog outputs at 12 bits, software-timed
- 12 TTL/CMOS digital I/O lines
- 32-bit, 5 MHz counter
- Digital triggering
- Bus-powered
- 1-year warranty

Operating Systems
- Windows Vista (32- and 64-bit)/XP/2000
- Mac OS X[1]
- Linux®[1]
- Windows Mobile[1]
- Windows CE[1]

Recommended Software
- LabVIEW
- LabVIEW SignalExpress
- LabWindows™/CVI
- Measurement Studio

Other Compatible Software
- C#, Visual Basic .NET
- ANSI C/C++

Measurement Services Software (included)
- NI-DAQmx driver software
- Measurement & Automation Explorer configuration utility
- LabVIEW SignalExpress LE

[1]You need to download NI-DAQmx Base for these operating systems.

Product	Bus	Analog Inputs[1]	Input Resolution (bits)	Max Sampling Rate (kS/s)	Input Range (V)	Analog Outputs	Output Resolution (bits)	Output Rate (Hz)	Output Range (V)	Digital I/O Lines	32-Bit Counter	Trigger
USB-6009	USB	8 SE/4 DI	14	48	±1 to ±20	2	12	150	0 to 5	12	1	Digital
USB-6008	USB	8 SE/4 DI	12	10	±1 to ±20	2	12	150	0 to 5	12	1	Digital

[1]SE = single ended, DI = differential   [2]Software-timed

Overview and Applications

With recent bandwidth improvements and new innovations from National Instruments, USB has evolved into a core bus of choice for measurement applications. The NI USB-6008 and USB-6009 are low-cost entry points to NI flagship data acquisition (DAQ) devices. With plug-and-play USB connectivity, these modules are simple enough for quick measurements but versatile enough for more complex measurement applications.

The USB-6008 and USB-6009 are ideal for a number of applications where low cost, small form factor, and simplicity are essential. Examples include:

- Data logging – quick and easy environmental or voltage data logging
- Academic lab use – student ownership of DAQ hardware for completely interactive lab-based courses (Academic pricing available. Visit **ni.com/academic** for details.)
- OEM applications as I/O for embedded systems

Recommended Software

National Instruments measurement services software, built around NI-DAQmx driver software, includes intuitive application programming interfaces, configuration tools, I/O assistants, and other tools designed to reduce system setup, configuration, and development time. National Instruments recommends using the latest version of NI-DAQmx driver software for application development in NI LabVIEW, LabVIEW SignalExpress, LabWindows/CVI, and Measurement Studio software. To obtain the latest version of NI-DAQmx, visit **ni.com/support/daq/versions**.

NI measurement services software speeds up your development with features including:

- A guide to create fast and accurate measurements with no programming using the DAQ Assistant.
- Automatic code generation to create your application in LabVIEW.
- LabWindows/CVI; LabVIEW SignalExpress; and C#, Visual Studio .NET, ANSI C/C++, or Visual Basic using Measurement Studio.
- Multithreaded streaming technology for 1,000 times performance improvements.
- Automatic timing, triggering, and synchronization routing to make advanced applications easy.
- More than 3,000 free software downloads available at **ni.com/zone** to jump-start your project.
- Software configuration of all digital I/O features without hardware switches/jumpers.
- Single programming interface for analog input, analog output, digital I/O, and counters on hundreds of multifunction DAQ hardware devices. M Series devices are compatible with the following versions (or later) of NI application software – LabVIEW, LabWindows/CVI, or Measurement Studio versions 7.x; and LabVIEW SignalExpress 2.x.

NATIONAL INSTRUMENTS™

Every M Series data acquisition device also includes a copy of LabVIEW SignalExpress LE data-logging software, so you can quickly acquire, analyze, and present data without programming. The NI-DAQmx Base driver software is provided for use with Linux, Mac OS X, Windows Mobile, and Windows CE operating systems.

Recommended Accessories

The USB-6008 and USB-6009 have removable screw terminals for easy signal connectivity. For extra flexibility when handling multiple wiring configurations, NI offers the USB-600x Connectivity Kit, which includes two extra sets of screw terminals, extra labels, and a screwdriver.

In addition, the USB-600x Prototyping Kit provides space for adding more circuitry to the inputs of the USB-6008 or USB-6009.

NI USB DAQ for OEMs

Shorten your time to market by integrating world-class National Instruments OEM measurement products into your embedded system design. Board-only versions of NI USB DAQ devices are available for OEM applications, with competitive quantity pricing and available software customization. The NI OEM Elite Program offers free 30-day trial kits for qualified customers. Visit **ni.com/oem** for more information.

Information for Student Ownership

To supplement simulation, measurement, and automation theory courses with practical experiments, NI has developed the USB-6008 and USB-6009 student kits, which include the LabVIEW Student Edition and a ready-to-run data logger application. These kits are exclusively for students, giving them a powerful, low-cost, hands-on learning tool. Visit **ni.com/academic** for more details.

Information for OEM Customers

For information on special configurations and pricing, call (800) 813 3693 (U.S. only) or visit **ni.com/oem**. Go to the Ordering Information section for part numbers.

Ordering Information

NI USB-6008[1] 779051-01
NI USB-6009[1] 779026-01
NI USB-6008 OEM 193132-02
NI USB-6009 OEM 193132-01
NI USB-6008 Student Kit[1,2] 779320-22
NI USB-6009 Student Kit[1,2] 779321-22
NI USB-600x Connectivity Kit 779371-01
NI USB-600x Prototyping Kit 779511-01

[1] Includes NI-DAQmx software, LabVIEW SignalExpress LE, and a USB cable.
[2] Includes LabVIEW Student Edition.

BUY NOW!

For complete product specifications, pricing, and accessory information, call 800 813 3693 (U.S. only) or go to **ni.com/usb**.

Low-Cost, Bus-Powered Multifunction DAQ for USB – 12- or 14-Bit, up to 48 kS/s, 8 Analog Inputs

Specifications

Typical at 25 °C unless otherwise noted.

Analog Input

Absolute accuracy, single-ended

Range	Typical at 25 ˚C (mV)	Maximum (0 to 55 ˚C) (mV)
±10	14.7	138

Absolute accuracy at full scale, differential[1]

Range	Typical at 25 ˚C (mV)	Maximum (0 to 55 ˚C) (mV)
±20	14.7	138
±10	7.73	84.8
±5	4.28	58.4
±4	3.59	53.1
±2.5	2.56	45.1
±2	2.21	42.5
±1.25	1.70	38.9
±1	1.53	37.5

Number of channels............................ 8 single-ended/4 differential
Type of ADC .... Successive approximation

ADC resolution (bits)

Module	Differential	Single-Ended
USB-6008	12	11
USB-6009	14	13

Maximum sampling rate (system dependent)

Module	Maximum Sampling Rate (kS/s)
USB-6008	10
USB-6009	48

Input range, single-ended.................. ±10 V
Input range, differential..................... ±20, ±10, ±5, ±4, ±2.5, ±2, ±1.25, ±1 V
Maximum working voltage .... ±10 V
Overvoltage protection .... ±35 V
FIFO buffer size .... 512 B
Timing resolution .... 41.67 ns (24 MHz timebase)
Timing accuracy .... 100 ppm of actual sample rate
Input impedance .... 144 kΩ
Trigger source................................... Software or external digital trigger
System noise..................................... 5 m V_{rms} (±10 V range)

Analog Output

Absolute accuracy (no load) .... 7 mV typical, 36.4 mV maximum at full scale
Number of channels........................... 2
Type of DAC .... Successive approximation
DAC resolution.................................. 12 bits
Maximum update rate .... 150 Hz, software-timed

Output range .... 0 to +5 V
Output impedance.............................. 50 Ω
Output current drive........................... 5 mA
Power-on state................................... 0 V
Slew rate.. 1 V/µs
Short-circuit current........................... 50 mA

Digital I/O

Number of channels........................... 12 total
8 (P0.<0..7>)
4 (P1.<0..3>)
Direction control .... Each channel individually programmable as input or output
Output driver type
USB-6008...................................... Open-drain
USB-6009...................................... Each channel individually programmable as push-pull or open-drain
Compatibility .... CMOS, TTL, LVTTL
Internal pull-up resistor .... 4.7 kΩ to +5 V
Power-on state................................... Input (high impedance)
Absolute maximum voltage range...... -0.5 to +5.8 V

Digital logic levels

Level	Min	Max	Units
Input low voltage	-0.3	0.8	V
Input high voltage	2.0	5.8	V
Input leakage current	–	50	µA
Output low voltage (I = 8.5 mA)	–	0.8	V
Output high voltage (push-pull, I = -8.5 mA)	2.0	3.5	V
Output high voltage (open-drain, I = -0.6 mA, nominal)	2.0	5.0	V
Output high voltage (open-drain, I = -8.5 mA, with external pull-up resistor)	2.0	–	V

Counter

Number of counters 1
Resolution .... 32 bits
Counter measurements...................... Edge counting (falling edge)
Pull-up resistor.................................. 4.7 kΩ to 5 V
Maximum input frequency.................. 5 MHz
Minimum high pulse width................. 100 ns
Minimum low pulse width.................. 100 ns
Input high voltage .... 2.0 V
Input low voltage .... 0.8 V

Power available at I/O connector

+5 V output (200 mA maximum)......... +5 V typical
+4.85 V minimum
+2.5 V output (1 mA maximum).......... +2.5 V typical
+2.5 V output accuracy .... 0.25% max
Voltage reference temperature drift... 50 ppm/°C max

[1]Input voltages may not exceed the working voltage range.

Physical Characteristics

If you need to clean the module, wipe it with a dry towel.

Dimensions (without connectors).......	6.35 by 8.51 by 2.31 cm (2.50 by 3.35 by 0.91 in.)
Dimensions (with connectors)	8.18 by 8.51 by 2.31 cm (3.22 by 3.35 by 0.91 in.)
Weight (without connectors)	59 g (2.1 oz)
Weight (with connectors)	84 g (3 oz)
I/O connectors...................................	USB series B receptacle (2) 16-position (screw-terminal) plug headers
Screw-terminal wiring	16 to 28 AWG
Screw-terminal torque.......................	0.22 to 0.25 N•m (2.0 to 2.2 lb•in.)

Power Requirement

USB (4.10 to 5.25 VDC)......................	80 mA typical 500 mA maximum
USB suspend.....................................	300 µA typical 500 µA maximum

Environmental

The USB-6008 and USB-6009 are intended for indoor use only.
Operating environment

Ambient temperature range...........	0 to 55 °C (tested in accordance with IEC-60068-2-1 and IEC-60068-2-2)
Relative humidity range	10 to 90%, noncondensing (tested in accordance with IEC-60068-2-56)

Storage environment

Ambient temperature range...........	-40 to 85 °C (tested in accordance with IEC-60068-2-1 and IEC-60068-2-2)
Relative humidity range	5 to 90%, noncondensing (tested in accordance with IEC-60068-2-56)
Maximum altitude..............................	2,000 m (at 25 °C ambient temperature)
Pollution degree	2

Safety and Compliance

Safety

This product is designed to meet the requirements of the following standards of safety for electrical equipment for measurement, control, and laboratory use:

- IEC 61010-1, EN 61010-1
- UL 61010-1, CSA 61010-1

Note: For UL and other safety certifications, refer to the product label or visit **ni.com/certification**, search by model number or product line, and click the appropriate link in the Certification column.

Electromagnetic Compatibility

This product is designed to meet the requirements of the following standards of EMC for electrical equipment for measurement, control, and laboratory use:

- EN 61326 EMC requirements; Minimum Immunity
- EN 55011 Emissions; Group 1, Class A
- CE, C-Tick, ICES, and FCC Part 15 Emissions; Class A

Note: For EMC compliance, operate this device according to product documentation.

CE Compliance

This product meets the essential requirements of applicable European Directives, as amended for CE marking, as follows:

- 2006/95/EC; Low-Voltage Directive (safety)
- 2004/108/EC; Electromagnetic Compatibility Directive (EMC)

Note: Refer to the Declaration of Conformity (DoC) for this product for any additional regulatory compliance information. To obtain the DoC for this product, visit **ni.com/certification**, search by model number or product line, and click the appropriate link in the Certification column.

Waste Electrical and Electronic Equipment (WEEE)

EU Customers: At the end of their life cycle, all products must be sent to a WEEE recycling center. For more information about WEEE recycling centers and National Instruments WEEE initiatives, visit **ni.com/environment/weee.htm**.

电子信息产品污染控制管理办法（中国 RoHS）

中国客户 National Instruments 符合中国电子信息产品中限制使用某些有害物质指令 (RoHS)。关于 National Instruments 中国 RoHS 合规性信息，请登录 ni.com/environment/rohs_china。(For information about China RoHS compliance, go to ni.com/environment/rohs_china.)

Appendix D

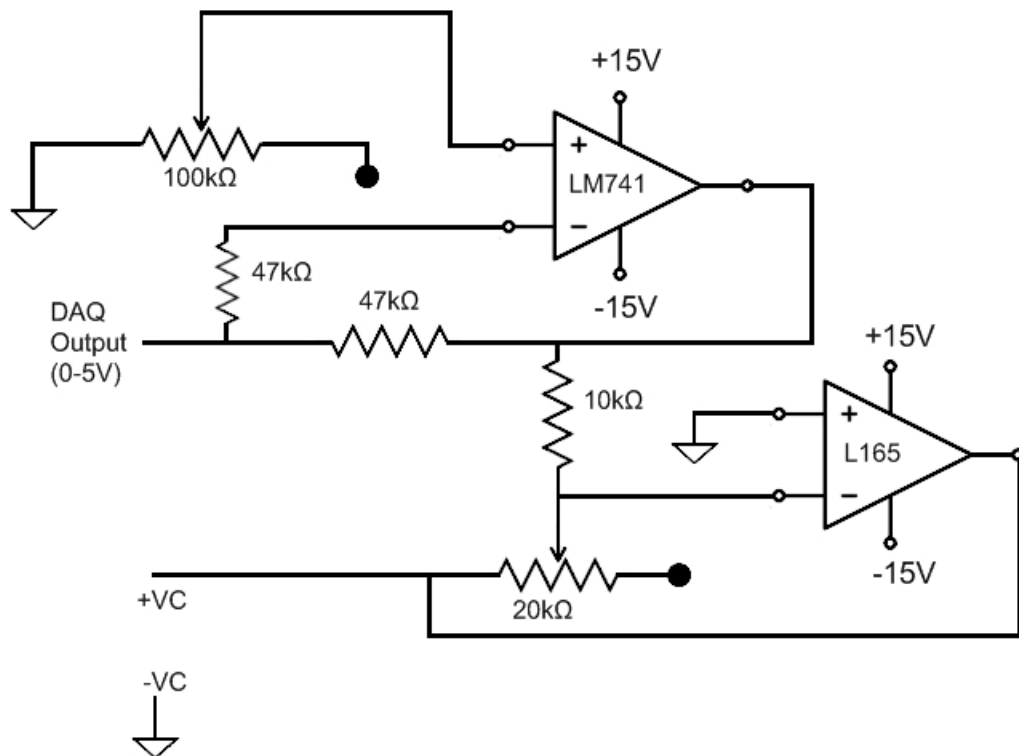## Schematic for the Amplifying Circuits found in the Control Box:

Figure D.1: The schematic of the amplifying circuit.

L165

3A POWER OPERATIONAL AMPLIFIER

- OUTPUT CURRENT UP TO 3A
- LARGE COMMON-MODE AND DIFFERENTIAL MODE RANGES
- SOA PROTECTION
- THERMAL PROTECTION
- ± 18V SUPPLY

DESCRIPTION

The L165 is a monolithic integrated circuit in Pentawatt® package, intended for use as power operational amplifier in a wide range of applications, including servo amplifiers and power supplies. The high gain and high output power capability provide superiore performance wherever an operational amplifier/power booster combination is required.

Pentawatt V

ORDERING NUMBER: L165V

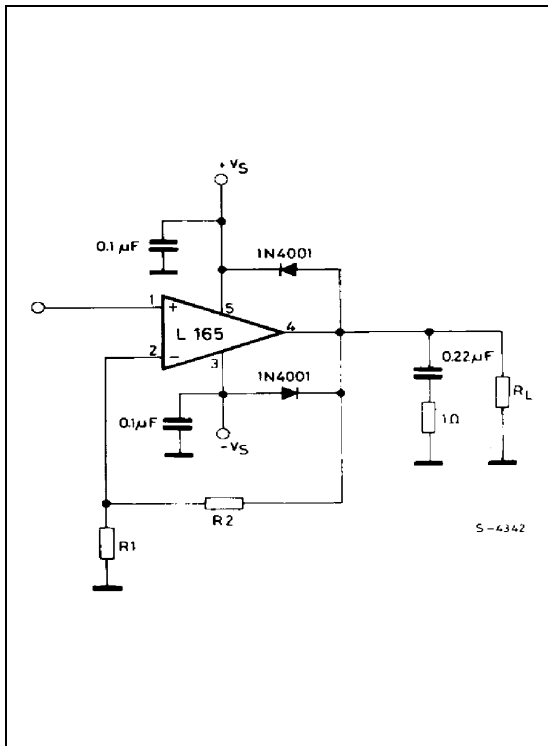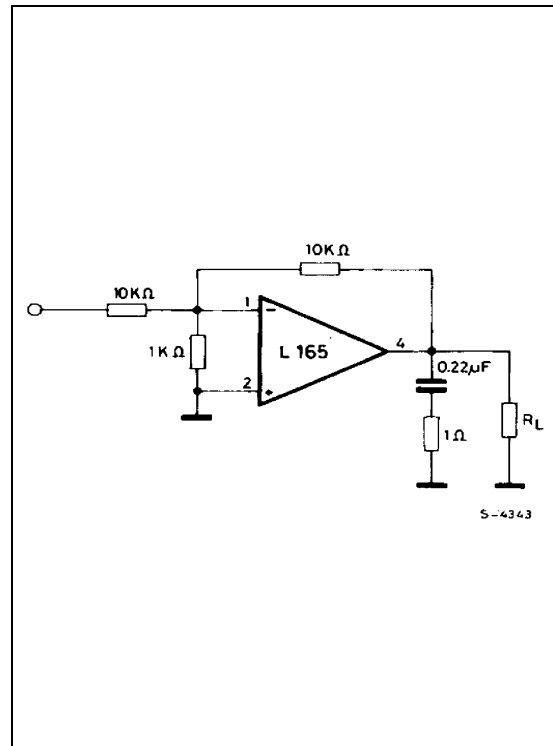### APPLICATION CIRCUITS

**Figure 1. Gain > 10.**

Figure 2. Unity gain configuration.

ABSOLUTE MAXIMUM RATINGS

Symbol	Parameter	Value	Unit
V_S	Supply voltage	± 18	V
V_5 V_4	Upper power transistor V_{CE}	36	V
V_4 V_3	Lower power transistor V_{CE}	36	V
V_i	Input voltage	V_S	
V_j	Differential input voltage	± 15	V
I_o	Peak output current (internally limited)	3.5	A
P_{tot}	Power dissipation at $T_{case} = 90°C$	20	W
T_{stg}, T_j	Storage and junction temperature	-40 to 150	°C

PIN CONNECTION (Top view)
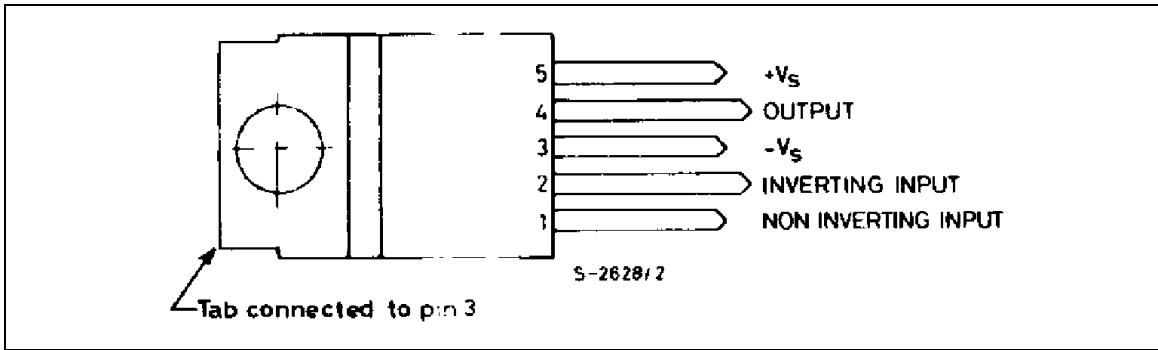
SCHEMATIC DIAGRAM
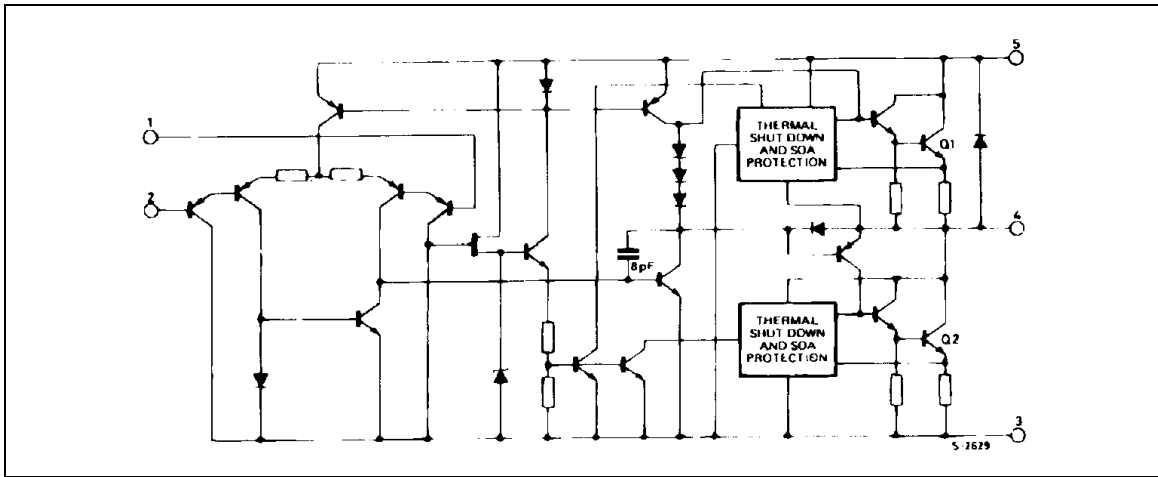
THERMAL DATA

Symbol	Parameter		Value	Unit
$R_{th-j-case}$	Thermal resistance junction-case	max	3	°C/W

ELECTRICAL CHARACTERISTCS (V_S = ± 15 V, T_j = 25 °C unless otherwise specified)

Symbol	Parameter	Test Condition	Min.	Typ.	Max.	Unit
V_S	Supply Voltage		± 6		± 18	V
I_d	Quiescent Drain Current	V_S = ±18 V		40	60	mA
I_b	Input Bias Current			0.2	1	µA
V_{os}	Input Offset Voltage			± 2	± 10	mV
I_{os}	Input Offset Current			± 20	± 200	nA
SR	Slew-rate	G_v = 10	8			V/µs
		G_v = 1 (°)	6			
V_o	Output Voltage Swing	f = 1kHz I_P = 0.3A I_P = 3A		27 24		V_{pp}
		f = 10kHz I_P = 0.3A I_P = 3A		27 24		V_{pp}
R	Input Resistance (pin 1)	f = 1 KHz	100	500		KΩ
G_v	Voltage Gain (open loop)			80		dB
e_N	Input Noise Voltage	B = 10 to 10 000 Hz		2		µV
i_N	Input Noise Current	f = 1 KHz		100		pA
CMR	Common-mode Rejection	R_g ≤ 10 KΩ; G_V = 30 dB		70		dB
SVR	Supply Voltage Rejection	R_g = 22 KΩ; V_{ripple} = 0.5 Vrms f_{ripple} = 100 Hz G_v = 10 G_v = 100		60 40		dB dB
	Efficiency	f = 1 kHz; R_L = 4Ω I_P = 1.6 A; P_o = 5W I_P = 1.6 A; P_o = 18W		70 60		% %
T_{sd}	Thermal Shut-down Case Temperature	P_{tot} = 12 W		110		°C
		P_{tot} = 6 W		130		°C

August 2000

National Semiconductor

LM741
Operational Amplifier

General Description

The LM741 series are general purpose operational amplifiers which feature improved performance over industry standards like the LM709. They are direct, plug-in replacements for the 709C, LM201, MC1439 and 748 in most applications.

The amplifiers offer many features which make their application nearly foolproof: overload protection on the input and output, no latch-up when the common mode range is exceeded, as well as freedom from oscillations.

The LM741C is identical to the LM741/LM741A except that the LM741C has their performance guaranteed over a 0˚C to +70˚C temperature range, instead of −55˚C to +125˚C.

Features

Connection Diagrams
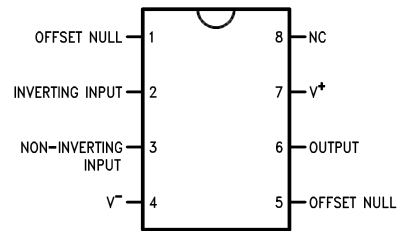
Metal Can Package
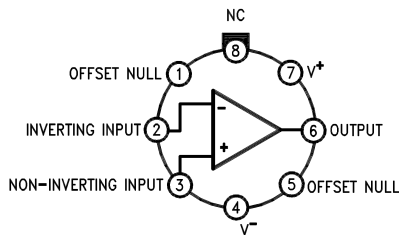
00934102

Note 1: LM741H is available per JM38510/10101

Order Number LM741H, LM741H/883 (Note 1)**,
LM741AH/883 or LM741CH
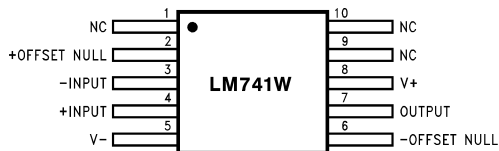See NS Package Number H08C**

Dual-In-Line or S.O. Package

00934103

**Order Number LM741J, LM741J/883, LM741CN
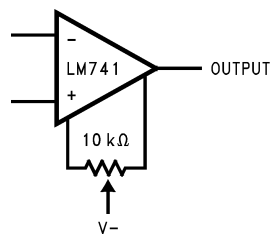See NS Package Number J08A, M08A or N08E**

Ceramic Flatpak

00934106

**Order Number LM741W/883
See NS Package Number W10A**

Typical Application

Offset Nulling Circuit

00934107

Absolute Maximum Ratings (Note 2)

If Military/Aerospace specified devices are required, please contact the National Semiconductor Sales Office/ Distributors for availability and specifications.

(Note 7)

	LM741A	LM741	LM741C
Supply Voltage	±22V	±22V	±18V
Power Dissipation (Note 3)	500 mW	500 mW	500 mW
Differential Input Voltage	±30V	±30V	±30V
Input Voltage (Note 4)	±15V	±15V	±15V
Output Short Circuit Duration	Continuous	Continuous	Continuous
Operating Temperature Range	−55˚C to +125˚C	−55˚C to +125˚C	0˚C to +70˚C
Storage Temperature Range	−65˚C to +150˚C	−65˚C to +150˚C	−65˚C to +150˚C
Junction Temperature	150˚C	150˚C	100˚C
Soldering Information			
N-Package (10 seconds)	260˚C	260˚C	260˚C
J- or H-Package (10 seconds)	300˚C	300˚C	300˚C
M-Package			
Vapor Phase (60 seconds)	215˚C	215˚C	215˚C
Infrared (15 seconds)	215˚C	215˚C	215˚C

See AN-450 "Surface Mounting Methods and Their Effect on Product Reliability" for other methods of soldering

surface mount devices.

| ESD Tolerance (Note 8) | 400V | 400V | 400V |

Electrical Characteristics (Note 5)

| Parameter	Conditions	LM741A Min	Typ	Max	LM741 Min	Typ	Max	LM741C Min	Typ	Max	Units
Input Offset Voltage	T_A = 25˚C $R_S \le$ 10 kΩ				1.0	5.0		2.0	6.0	mV
	$R_S \le$ 50Ω		0.8	3.0							mV
	$T_{AMIN} \le T_A \le T_{AMAX}$ $R_S \le$ 50Ω			4.0							mV
	$R_S \le$ 10 kΩ						6.0			7.5	mV
Average Input Offset Voltage Drift				15							µV/˚C
Input Offset Voltage Adjustment Range	T_A = 25˚C, V_S = ±20V	±10				±15			±15		mV
Input Offset Current	T_A = 25˚C		3.0	30		20	200		20	200	nA
	$T_{AMIN} \le T_A \le T_{AMAX}$			70		85	500			300	nA
Average Input Offset Current Drift				0.5							nA/˚C
Input Bias Current	T_A = 25˚C		30	80		80	500		80	500	nA
	$T_{AMIN} \le T_A \le T_{AMAX}$			0.210			1.5			0.8	µA
Input Resistance	T_A = 25˚C, V_S = ±20V	1.0	6.0		0.3	2.0		0.3	2.0		MΩ
	$T_{AMIN} \le T_A \le T_{AMAX}$, V_S = ±20V	0.5									MΩ
Input Voltage Range	T_A = 25˚C							±12	±13		V
	$T_{AMIN} \le T_A \le T_{AMAX}$				±12	±13					V

Electrical Characteristics (Note 5)   (Continued)

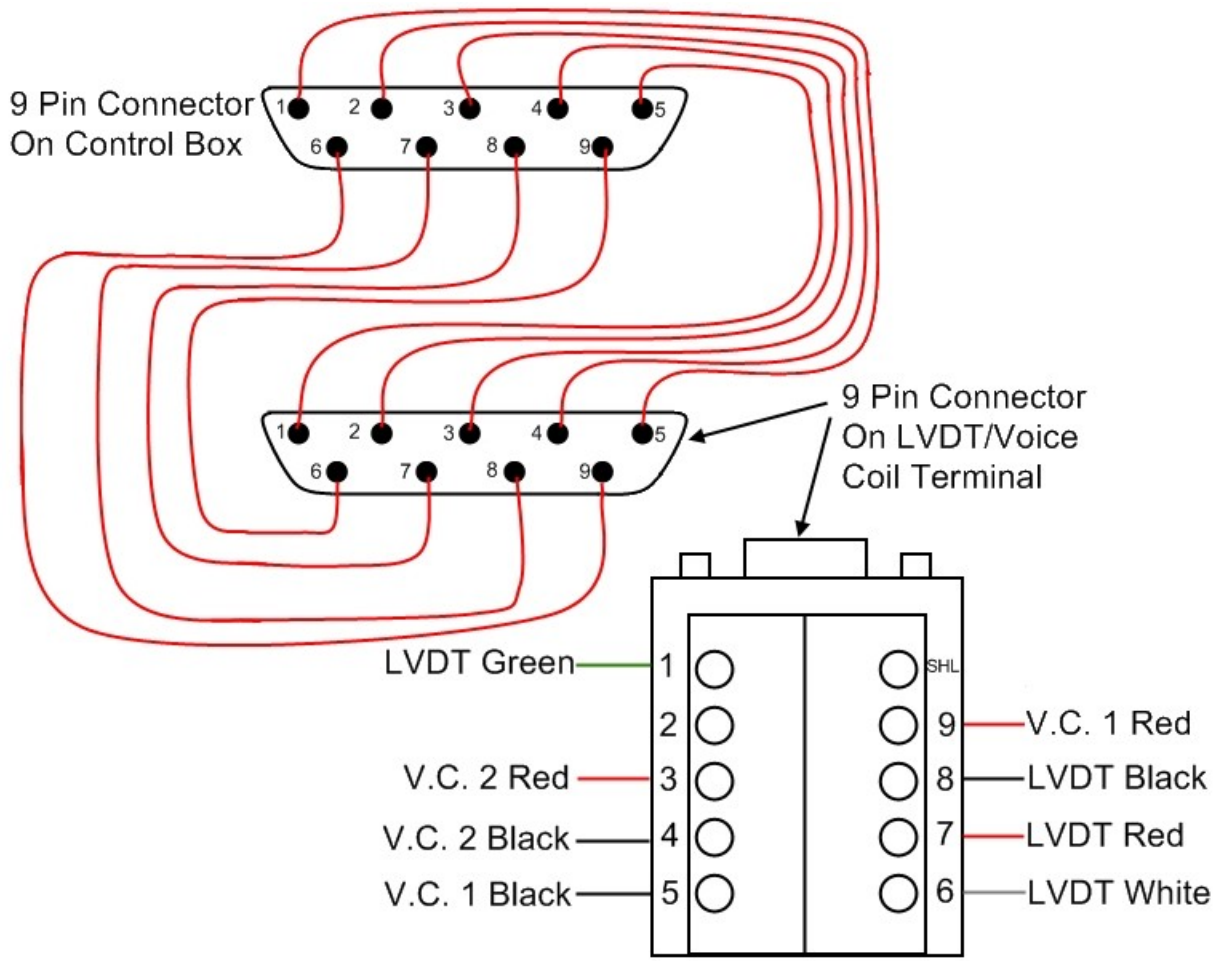| Parameter	Conditions	LM741A			LM741			LM741C			Units
		Min	Typ	Max	Min	Typ	Max	Min	Typ	Max	
Large Signal Voltage Gain	$T_A = 25°C$, $R_L \geq 2$ kΩ										
	$V_S = \pm20V$, $V_O = \pm15V$	50									V/mV
	$V_S = \pm15V$, $V_O = \pm10V$				50	200		20	200		V/mV
	$T_{AMIN} \leq T_A \leq T_{AMAX}$,										
	$R_L \geq 2$ kΩ,										
	$V_S = \pm20V$, $V_O = \pm15V$	32									V/mV
	$V_S = \pm15V$, $V_O = \pm10V$				25			15			V/mV
	$V_S = \pm5V$, $V_O = \pm2V$	10									V/mV
Output Voltage Swing	$V_S = \pm20V$										
	$R_L \geq 10$ kΩ	±16									V
	$R_L \geq 2$ kΩ	±15									V
	$V_S = \pm15V$										
	$R_L \geq 10$ kΩ				±12	±14		±12	±14		V
	$R_L \geq 2$ kΩ				±10	±13		±10	±13		V
Output Short Circuit Current	$T_A = 25°C$	10	25	35		25			25		mA
	$T_{AMIN} \leq T_A \leq T_{AMAX}$	10		40							mA
Common-Mode Rejection Ratio	$T_{AMIN} \leq T_A \leq T_{AMAX}$										
	$R_S \leq 10$ kΩ, $V_{CM} = \pm12V$				70	90		70	90		dB
	$R_S \leq 50\Omega$, $V_{CM} = \pm12V$	80	95								dB
Supply Voltage Rejection Ratio	$T_{AMIN} \leq T_A \leq T_{AMAX}$,										
	$V_S = \pm20V$ to $V_S = \pm5V$										
	$R_S \leq 50\Omega$	86	96								dB
	$R_S \leq 10$ kΩ				77	96		77	96		dB
Transient Response	$T_A = 25°C$, Unity Gain										
Rise Time			0.25	0.8		0.3			0.3		µs
Overshoot			6.0	20		5			5		%
Bandwidth (Note 6)	$T_A = 25°C$	0.437	1.5								MHz
Slew Rate	$T_A = 25°C$, Unity Gain	0.3	0.7			0.5			0.5		V/µs
Supply Current	$T_A = 25°C$					1.7	2.8		1.7	2.8	mA
Power Consumption	$T_A = 25°C$										
	$V_S = \pm20V$		80	150							mW
	$V_S = \pm15V$					50	85		50	85	mW
LM741A	$V_S = \pm20V$										
	$T_A = T_{AMIN}$			165							mW
	$T_A = T_{AMAX}$			135							mW
LM741	$V_S = \pm15V$										
	$T_A = T_{AMIN}$					60	100				mW
	$T_A = T_{AMAX}$					45	75				mW

Note 2: "Absolute Maximum Ratings" indicate limits beyond which damage to the device may occur. Operating Ratings indicate conditions for which the device is functional, but do not guarantee specific performance limits.

Appendix E

Wiring Inside of the Control Box:
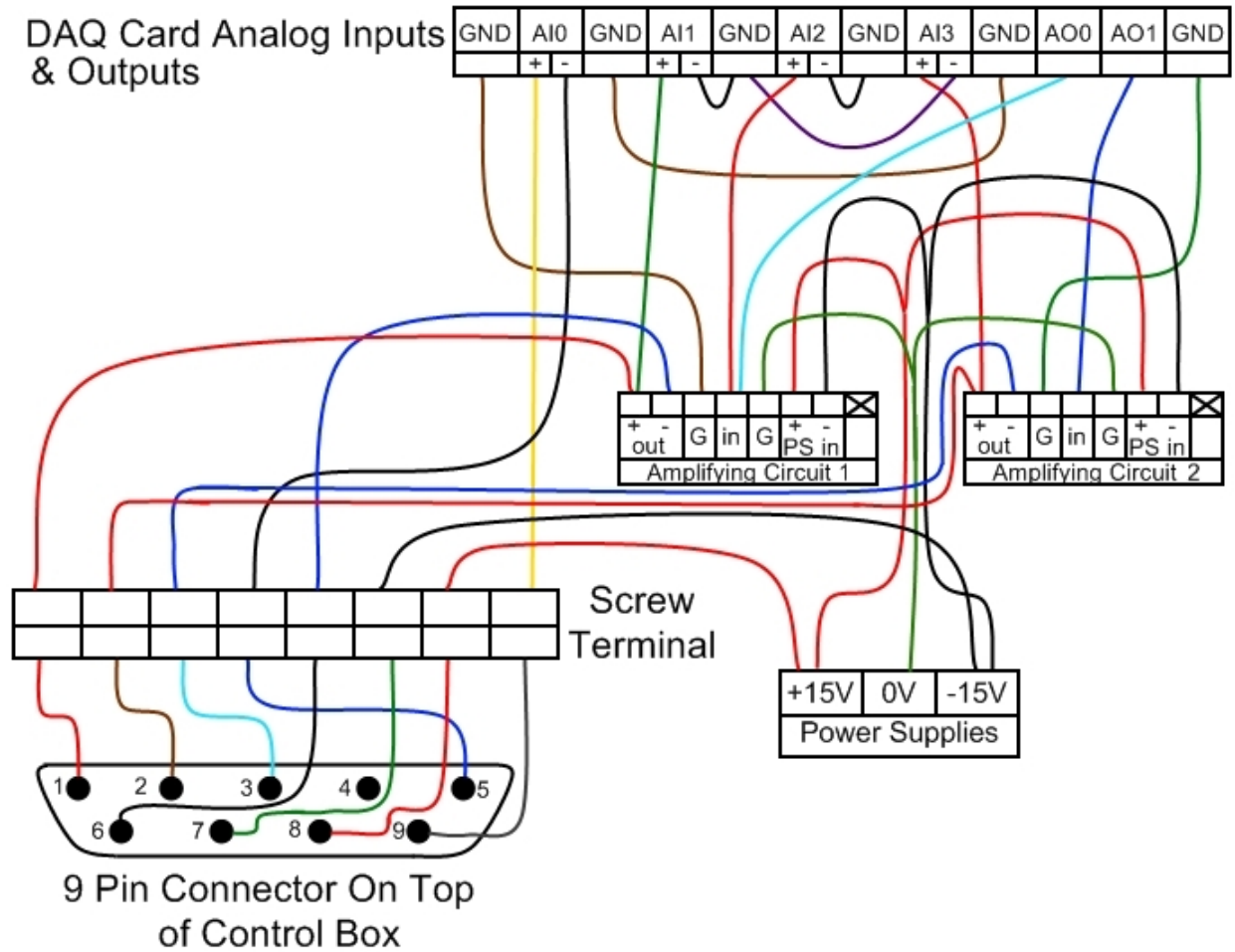
NOTE: The pins literally "flip" going from the box to the terminal where the LVDT and two voice coils are wired. See figure below:

9 Pin Connector On Control Box

9 Pin Connector On LVDT/Voice Coil Terminal

LVDT Green — 1

2

V.C. 2 Red — 3

V.C. 2 Black — 4

V.C. 1 Black — 5

SHL

9 — V.C. 1 Red

8 — LVDT Black

7 — LVDT Red

6 — LVDT White

Bibliography

[1] Riverhawk company flexural pivots. http://www.flexpivots.com/index.asp.

[2] S. W. Attaway. The mechanics of friction in rope rescue. *International Technical Rescue Symposium*, 1999.

[3] R. G. Budynas and J. K. Nisbett. *Shigley's Mechanical Engineering Design.* McGraw-Hill, Hoboken, New Jersey, eighth edition, 2008.

[4] E. Y. Choueiri. Critical history of electric propulsion: The first 50 years, (1906 to 1956).

[5] Daniel G. Courtney. Development and characterization of a diverging cusped field thruster and a lanthanum hexaboride hollow cathode. Master's thesis, Massachusetts Institute of Technology, Department of Aeronautics and Astronautics, 2008.

[6] David Darling. Elecric space propulsion, the internet encyclopedia of science. http://www.daviddarling.info/encyclopedia/E/electricprop.html.

[7] de Aquino M. G. S. de Lucena, S. E. and A. Caporalli-Filho. A load cell for grain-propelled ballistic rocket thrust measurement. *Instrumentation and Measurement Technology Conference*, pages 1767–1772, May 2005.

[8] R. S. Figliola and D.E. Beasley. *Theory and Design for Mechanical Measurements.* John Wiley and Sons, Inc., Hoboken, New Jersey, fourth edition, 2006.

[9] E. M. Goodger. *Principles of Spaceflight Propulsion*, volume 6 of *International Series of Monographs in Aeronautics and Astronautics*. Pergamon Press, London, England, first edition, 1970.

[10] Dewitt D. P. Bergman T. L. Lavine A. S. Incropera, F. P. *Fundamentals of Heat and Mass Transfer*. John Wiley and Sons, Inc., Hoboken, New Jersey, sixth edition, 2007.

[11] Robert G. Jahn. *Physics of Electric Propulsion*. Dover, Mineola, New York, first edition, 2006.

[12] Manuel Martinez-Sanchez. 16.522, space propulsion, lecture 13-14: Electrostatic thrusters.

[13] Manuel Martinez-Sanchez. 16.522, space propulsion, lecture 17: Notes on hall thrusters.

[14] Jareb Mirczak. Milli-newton thrust stand for electric propulsion. Master's thesis, Massachusetts Institute of Technology, Department of Aeronautics and Astronautics, May 2003.

[15] Norman S. Nise. *Control Systems Engineering*. John Wiley and Sons, Inc.

[16] Markusic T. E. Stanojev B. J. Dehoyos A. Polzin, K. A. and B. Spaun. Thrust stand for electric propulsion performance evaluation. Technical report, NASA-Marshall Space Flight Center, Huntsville, AL 35812.

[17] C. Rossi S. Orieux and D. Esteve. Thrust stand for ground tests of solid propellant microthrusters. *Review of Scientific Instruments*, 73(7):2694–2698, July 2002.

[18] Paul Scherz. *Practical Electronics for Inventors*. McGraw Hill, second edition, 2007.

[19] Ching-Fang Tu and Fort Fort, Tomlinson. A study of fiber-capstan friction. 1. stribeck curves. *Tribology International*, pages 701–710, 2004.